Cold Atoms in a Ring Cavity

by

Lawrence Mudarikwa

A thesis submitted to
The University of Birmingham
for the degree of
DOCTOR OF PHILOSOPHY

Ultracold Atoms Group
School of Physics and Astronomy
College of Engineering and Physical Sciences
The University of Birmingham

March 2015

Abstract

An ensemble of atoms coupled to a high finesse optical cavity is an ideal test bed for the study of the cooperative behavior of atom-photon systems. Dicke showed that an ensemble of excited atoms coupled to a light field interacts with the light in a collective and coherent fashion leading to the emission of highly directional spontaneous emission whose intensity scales with the square of the number of atoms, a phenomenon known as superradiance.

This thesis describes the build of an experiment to study cooperative atom-photon interactions in a ring cavity. Particular focus is given to the cavities used in the experiment. Firstly a transfer cavity used for transferring stability to off-resonant lasers in the experiment, this was developed with the capability of exploiting Gouy phase degeneracies to produce tightly spaced frequency discriminants to be used as lock points. Secondly the ring cavity for the experiment which is atypical in its design allowing for bidirectional probing of the cavity mode and dynamic manipulation of the intra-cavity optical lattice. An intra-cavity MOT was produced and collective strong coupling was observed in the cavity with ≈ 6400 atoms coupled to the cavity mode.

CONTENTS

1 Introduction **1**

1.1 Brief History of Cavity QED 1

1.2 Motivation 2

1.3 State of Art 3

1.4 Outline of Thesis 3

2 Cavity QED **5**

2.1 The Jaynes-Cummings Hamiltonian 5

2.2 Master Equation 7

2.3 Strong Coupling: One to Many Atoms 9

3 Experiment Overview **12**

3.1 Plan 12

3.2 Setup 13

4 Optical Cavities **15**

4.1 Resonant Character of Cavities 15

4.2 Gaussian Waves 18

4.3 Higher-Order Gaussian Waves 21

4.4 ABCD Matrix 23

4.5 Higher-Order Gaussian waves in a Cavity 23

4.6 Cavity Types and Stability 24

5 The Transfer Cavity **26**

5.1 Design of the Cavity 26

5.2 The Gouy Degenerate Cavity . . . 29
5.3 The Hänsch-Couillaud Laser Lock Technique . . . 32
5.3.1 Background . . . 32
5.3.2 Setup . . . 33
5.3.3 Results . . . 35
5.4 Pound Drever Hall locking scheme . . . 38
5.4.1 Setup . . . 39
5.4.2 Transmission PDH vs Reflection PDH . . . 42
5.5 Discussion . . . 43

6 The Ring Cavity **44**
6.1 Design and Fabrication . . . 44
6.2 Mode Volume and Astigmatism . . . 46
6.3 Finesse and Linewidth . . . 50
6.4 Impedance matching and mode matching . . . 52
6.5 Cavity Stability . . . 54
6.6 Cavity Alignment . . . 55

7 The Vacuum System **58**
7.1 The Vacuum Chamber . . . 58
7.2 Viewports . . . 59
7.3 Vacuum Parts . . . 59
7.4 Conductance calculations . . . 61
7.5 Custom Bottom Flange . . . 63
7.6 Dispenser Arm . . . 64
7.7 Vacuum Assembly . . . 66

8 Building the Experiment **72**
8.1 Laser Systems . . . 72
8.1.1 Custom ECDLs . . . 72
8.1.2 Atomic Laser Locking Techniques . . . 75
8.1.3 Overview of the Laser Locking Scheme for the Experiment . . . 82
8.2 Magneto-Optical Trapping of Potassium . . . 84

8.2.1 Laser Cooling and Trapping 84
8.2.2 Elongated MOT Setup 87
8.2.3 Observation of Intra-cavity MOT 88

9 Light in the Cavity **93**
9.1 Reduced Dipole Matrix Element 93
9.2 Observation of Cavity Peaks 95
9.3 Atoms in the Cavity Mode 96
9.4 New Cavity Mirrors 97
9.5 Preliminary Observation of Rabi Splitting 99

10 Outlook **101**
10.1 Looking Forward 102

Appendix A Octave Code for Fitting Multiple Cavity Peaks **I**
A.1 Fitting Lorentzians onto Multiple Cavity Peaks I

Acknowledgements **IV**

List of References **VI**

LIST OF FIGURES

2.1 Jaynes-Cummings ladder for the dressed state of a coupled atom-cavity system. 7

2.2 Normal mode splitting of a coupled atom-cavity system. 10

3.1 Schematic of the full experimental setup. 14

4.1 A schematic of an optical cavity. The cavity is formed by two mirrors separated by a distance d. Each mirror has an associated reflection and transmission field amplitude coefficients r_1, r_2 and t_1, t_2, respectively. A field of amplitude E_{in} impinges on mirror one, leading to a circulating field, E_{circ} inside the cavity, a transmitted field, E_{tran} and a reflected field, E_{refl}. 16

4.2 Transmission profile of a field incident on a cavity, away from resonance no light enters the cavity, upon resonance there is a sudden spike in the transmitted intensity. 18

4.3 Reflection profile of a field incident on a cavity, away from resonance no light enters the cavity, upon resonance there is a sudden dip in the reflected intensity. 19

4.4 Gaussian beam near a focus showing the radial intensity profile and spherical wavefronts. . . 21

4.5 Gouy phase shift of π about the focus of a Gaussian beam. 21

4.6 Spatial energy distribution for Hermite-Gaussian modes. 22

4.7 Two-mirror standing wave cavity and a three-mirror traveling wave cavity. 25

5.1 CAD drawing of the transfer cavity. 27

5.2 Example of 3rd order and 6th order Golomb ruler [1]. 27

5.3 The cavity cylinder cut into sections determined by 5th order Golomb ruler. 28

5.4 Location of the solutions of equation 5.4. This plot can be used for choosing appropriate mirror separation for a desired value of N [14]. 30

5.5 Transmission peaks showing degenerate mode spacing positions of the cavity as determined by equation 5.4, with a mode spacing of 275 MHz, 637 MHz, 100 MHz and 77 MHz. (left top - right top - left bottom - right bottom). 31
5.6 Linewidth of the cavity as a function of cavity length, a 1/x line fit is used to find an estimate of the Finesse, which was found to be 188 ± 15. 32
5.7 Transmission of two planes of polarization through the cavity. The Brewster's angle plate reduces the transmission for the vertically polarized component (red) while letting the horizontally polarized component (green) propagate freely [41]. 33
5.8 Photodiode signals relative to the incident intensity over laser wavelength (top), magnified for a single resonance (middle). Dispersion shaped difference signal for the same frequency range (bottom). 34
5.9 The experimental setup for Hänsch-Couillard, light from a laser is linearly polarised then sent a cavity a Brewster window in the middle. The output of the cavity is sent an analyser consisting a 1/4 wave plate and PBS. 35
5.10 (Top) Transmission peaks of two planes of polarization through the cavity at a mode-spacing of 152 MHz. (Bottom) The error signal produced. 36
5.11 (Top) Transmission peaks of two planes of polarization through the cavity at a mode-spacing of 116 MHz. (Bottom) The error signal produced. 36
5.12 (Top) Transmission peaks of two planes of polarization through the cavity at a mode-spacing of 501 MHz (confocal). (Bottom) The error signal produced. 37
5.13 Linewidth of the cavity (with Brewster window) as a function of cavity length, a 1/x line fit is used to find an estimate of the Finesse, which was found to be 66 ± 5. 37
5.14 Error signal produced by the PDH technique. 39
5.15 Setup of the PDH technique, the laser is current modulated at the modulation frequency ω_m producing phase modulated light which is sent through the cavity. The signal from the cavity is sent to a mixer where it is mixed with the LO and the output of the mixer is low-pass filtered and viewed on the oscilloscope. 40
5.16 (Top) Transmission peaks of the PDH signal through the cavity with mode spacing of 42 MHz at a modulation frequency of 35 MHz. (Bottom) The error signal produced. 41
5.17 (Top) Transmission peaks of the PDH signal through the cavity with mode spacing of 42 MHz at a modulation frequency of 25 MHz. (Bottom) The error signal produced. 41

5.18 (Top) Transmission peaks of the PDH signal through the cavity with mode spacing of 42 MHz at a modulation frequency of 21 MHz. (Bottom) The error signal produced. 42

6.1 Mirror positions of the cavity in relation to the MOT beams. 45
6.2 3D CAD model of the ring cavity showing MOT beam access. 46
6.3 Input/Output channels for the cavity. 47
6.4 Cavity frame after machining. 48
6.5 Cavity mirror gluing and heat curing procedure in portable oven. 49
6.6 Astigmatism abberation in which sagittal and tangential rays become non-degenerate [40]. . . 50
6.7 Data from the manufacturer showing the reflectivities of s-pol light on the dielectric ring cavity mirrors at 45° and 22.5° incident angle over desired wavelength range. 51
6.8 Aberration balancing mode matching system. 53
6.9 Aberration coefficients for typical lens shapes [13]. 54
6.10 Left: (A), beam plane and mirror positions for ideal case with no misalignment. (B) Tilt of the curved mirrors causes the beam path to become unstable and the beam walks. (C) Translation of the curved mirror to find new stable center of curvature for the cavity axis. (D), Cavity axis is translated to match the new center of curvature of the tilted mirror where the mode is stable. Right: New cavity axis for the ring cavity to compensate for deviations from planarity in our system. 56
6.11 From Left to Right: Multiple passes through the cavity eventually converge to form one stable cavity mode. 56
6.12 Using the fluorescence of the atoms the beam paths of the cavity mode are clearly visible, unstable cavity with beam walking out of alignment after a few passes is visible in the right picture. 57

7.1 The spherical octagon used as the main experimental chamber of the experiment. 59
7.2 Top and side view of the full vacuum design. 60
7.3 The effective path of pumping from the vacuum chamber to the ion pump. 62
7.4 The custom bottom flange for the vacuum chamber with the positions of the cavity bolt holes (1,2,3), electrical feedthrough (4) and MOT beam hole (5) indicated. 63
7.5 The custom bottom flange for the vacuum chamber showing the extending pipe welded between the bottom flange and a 2.75" CF flange and a viewport subsequently attached to the flange. 64

7.6 Cross section of an atom dispenser showing typical dimensions in mm and notable features (left) and the electrical feedthrough driving the dispensers and the configuration of the inline connectors securing the dispensers (right). 65
7.7 Flexible resistive heaters wrapped around the dispenser arm. 66
7.8 2D slice across a vacuum part showing (A) The appearance of a virtual leak when a volume of air is trapped by a bolt in a blind hole. (B) Vent hole that allows the trapped volume to escape. (C) Graph showing the difference between a real leak and virtual leak. 67
7.9 Fully assembled vacuum system. 68
7.10 The cavity inside the vacuum chamber. 69
7.11 Pressure change in the vacuum as the system is baked with temperature (red) and pressure (blue). 71

8.1 The EDCL in the Littrow configuration. 73
8.2 The EDCL mechanical construction. 74
8.3 Measurement of the beam size of the laser output. TOP: Measurement of the horizontal width. BOTTOM: Measurement of the vertical width. 75
8.4 Setup for saturated absorption spectroscopy and the corresponding spectral features of the probe beam. 76
8.5 Energy level spectrum for the D2 line of ^{39}K and ^{41}K. The grey lines crossing over the ground and excited levels show the Doppler linewidth and natural linewidth respectively. Units are in MHz detuning from the fine structure transition. 77
8.6 (Left) The setup for direct modulation spectroscopy. The blue line represents the pump beam and red is the probe. (Right) Upper trace shows a substracted saturation absorption signal and the lower trace the direct modulation signal. 78
8.7 (Left) The setup for modulation transfter spectroscopy. The blue line represents the pump beam and red is the probe. (Right) Upper trace shows a substracted saturation absorption signal and the lower trace the modulation transfer signal. 79
8.8 Setup for generation polarisation spectroscopy signal. 80
8.9 Error signals produced by polarisation spectroscopy. (Red) Signal produced using a NPBS in the setup and (Green) signal produced using a gold mirror. 80

8.10 (a) Setup used to produce split beam magnetically induced dichroism signals. The dashed quarter-wave plate QWP* is absent in Type I spectroscopy and present in Type II. (b) Comparison of pump and probe polarizations for Type I and II configurations. (c) Type I spectroscopy error signal (d) Type II spectroscopy error signal. 82
8.11 Offset lock technique used to stabilise the slave lasers with respect to the master laser. 83
8.12 Locking scheme for the experiment, the direction of arrows denotes the direction of the lock. 84
8.13 Model of the trapping mechanism for a MOT using circularly polarised light and a magnetic field gradient. 86
8.14 3D MOT coil setup for creating an elongated MOT. Red beams are for the MOT and blue beams are for the cavity. 87
8.15 Fully assembled coil system to generate the magnetic field for the MOT with the water cooling system installed. 88
8.16 The energy level diagram for ^{39}K D2 transitions where the cooling and repump transitions are highlighted, Δ_1 is the detuning of the cooling beam and Δ_2 is the detuning of the repump beam. Units are in MHz detuning from the fine structure transition. 89
8.17 The intra-cavity MOT. 90
8.18 The 2D Gaussian fit of the MOT. 91

9.1 The relative strength of the m_F transitions for the D2 $F = 2 \rightarrow F' = 3$ transition of Potassium in units of μ. Greens are π transitions, blue are σ_- and red are σ_+. 95
9.2 Transmission peak through the ring cavity. 96
9.3 Figure showing the input/output direction of the probe laser. 98
9.4 The cavity with replaced input/output coupler mirrors. 99
9.5 First observation of Rabi splitting 100

10.1 CAD design of the new ring cavity. 103

A.1 Output of the Octave code after fitting Lorentzians on 3 peaks. II
A.2 Output of the Octave code after fitting Lorentzians on 5 peaks. III
A.3 Output of the Octave code after fitting Lorentzians on 2 peaks. III

CHAPTER 1

INTRODUCTION

1.1 Brief History of Cavity QED

The field of Cavity Quantum Electro-dynamics (Cavity QED) traces its roots from the seminal work by Purcell, he predicted that the radiative properties of an atom can be modified by the presence of a resonant cavity [47]. Cavity QED experiments initially explored the enhancing and inhibition of the spontaneous emission rate of an atom coupled to a cavity. Fermi's golden rule states that the decay rate of an atom, Γ_{free}, is dependent on the density of electromagnetic states in free space. A resonant cavity serves to enhance the density of states leading to increased spontaneous emission. This effect is known as Purcell enhancement [33]. The modified decay rate of an atom in the presence of a cavity is given by

$$\Gamma_{cavity} = F_{Purcell}\Gamma_{free}, \tag{1.1}$$

where $F_{Purcell}$ is given by

$$F_{Purcell} = \frac{3}{4\pi^2}\left(\frac{\lambda^3}{V}\right)Q, \tag{1.2}$$

where λ is the wavelength of the resonant transition coupling the atom and the cavity, Q is the quality factor of the cavity and V is the mode volume of the cavity. As technology improved, cavities with higher Q were realised, resulting in experiments were the coherent interaction of an atom with a photon in a cavity overwhelmed the spontaneous decay of the atom. This regime is known as 'strong coupling' and most modern cavity QED experiments aim to operate in this regime.

Cavity QED in the strong coupling regime comes in two flavours, superconducting microwave cavities interacting with Rydberg atoms and low lying atoms interacting with optical cavities. The former was

initially the method of choice as the lifetime of Rydberg states were relatively long, lowering the threshold Q required to reach strong coupling. The pace of the atom-field entanglement is very slow allowing for complex multi-qubit entangled states [49]. The major drawback for this method was the need for cryogenic cooling of the superconducting material. Improvements in optical mirror manufacturing techniques enabled strong coupling to be reached with optical cavities [29]. Cavity QED with low lying atoms in optical cavities has much faster interactions and dissipations but has the advantage of being able to couple photons in and out the cavity very efficiently.

Cavity QED experiments can be characterised by three distinct parameters, the atom spontaneous decay rate, γ, the decay rate of the cavity, κ and the strength of interaction between the atom and cavity mode, g. The strong coupling regime is reached when $g \gg \gamma, \kappa$.

1.2 Motivation

This thesis aims to study an ensemble of atoms coupled to a high finesse optical cavity. This ensemble of atoms can be made to behave cooperatively through their common interaction with the cavity mode. Long range interactions and correlations are at the heart of variety of physical phenomena, from protein folding to superconductivity. Dicke showed that an ensemble of excited atoms coupled to a light field interact with the light in a collective and coherent fashion. This leads to the emission of highly directional spontaneous emission whose intensity scales with the square of the number of atoms, a phenomenon known as superradiance [17]. The object of this thesis is to build an experiment to study ultracold atoms in a high finesse ring cavity.

Ring cavities differ from traditional Fabry-Perot design by having pairs of counterpropating modes comprised of running waves. This adds an extra degree of freedom to the system where the resultant standing wave mode is not limited by the boundary conditions of the mirror surfaces but is free to rotate by changing the phase of one the input modes. It is also possible for momentum to be coherently exchanged between the field modes, meaning that an atom can have a noticeable back action on the optical field. This back action of the field is sensed by all the atoms trapped in the cavity mode and hence the motions of all the atoms are now coupled through the field mode, leading to rich cooperative behavior such as Recoil Induced Resonances (RIR) [12], [34].

1.3 State of Art

Experiments studying the collective behavior of cold atoms in ring cavities have been studied in the groups of Hemmerich in Hamburg [20] and Zimmermann and Courteille in Tübigen [39]. The experiments in Tübigen were able to observe superradiant behavior of cold atoms evoked by their collective interaction with a light field. This was in the form of Superradiant Rayleigh Scattering (SRyS) [56] and Collective Atomic Recoil Lasing (CARL) [35]. SRyS was first observed in free space by shining a short laser pulse into a Bose-Einstein condensate [30]. The scattering atoms collectively formed motional sidebands that are coupled out of the condensate. Light scattered into the long axis of the condensate induces matter-wave interference between the recoiling atoms and atoms at rest. This leads to the formation of a density grating which exponentially enhances the scattering.

The experiment in Tubigen to observe SRyS studies a BEC of ^{87}Rb loaded into the mode volume of a high-finesse optical ring cavity. A strong pump beam is shone onto the atomic cloud from one of the modes of the ring cavity. This leads to an exponential growth of an unpumped probe field in the counterpropagating mode and an atomic density grating. SRyS is observed not as a single burst of light but a train of light pulses demonstrating that the cavity helps preserves the coherence of the effect against diffusion. To study CARL the same experimental setup was used but with just ultracold atoms not BEC. CARL shares the same gain mechanism as SRyS where light is scattered from the pumped mode into the reverse, leading the atoms to self-organise into a density grating. The main difference between the two phenomena is that for SRyS the coherence is stored in the momentum states of the atoms where as for CARL the coherence is stored in the light field of cavity.

1.4 Outline of Thesis

This thesis reports the designing and building of a ring cavity experiment with cold Potassium atoms carried out in the Cold Atom group at the University of Birmingham, under the supervision of Dr. J. Goldwin. We chose Potassium as it has both fermionic and bosonic isotopes available, all rich with tunable Feshbach scattering resonance.

Chapter 2 presents the theoretical framework describing the interaction of an atom and a cavity mode. It uses the Jaynes-Cummings Hamiltonian as a starting point and extends to the Tavis-Cummings model for an ensemble of atoms interacting with a cavity mode.

Chapter 3 presents an overview of the experiment, with the aims and plan detailed.

Chapter 4 presents an elementary description of optical cavities and their characteristics and the interaction of Gaussian waves with cavities.

Chapter 5 presents the design and building of the transfer cavity for the experiment used to transfer the stability of the master laser to the off-resonant laser used to lock the ring cavity. Methods of locking the transfer cavity were studied, namely the Hänsch-Couillaud and Pound-Drever-Hall technique.

Chapter 6 presents the design and fabrication of the ring cavity used in the experiment. Key parameters are characterised including the Finesse, linewidth, mode matching, impedance matching, stability and alignment of the cavity.

Chapter 7 presents the design and building of the vacuum system for the experiment. The conductance of the system is characterised and a custom bottom flange and dispenser arm are described.

Chapter 8 presents the building of the laser systems and Magneto-Optical Trap (MOT) required to cool and trap the atoms. A number of atomic spectroscopic techniques for stabilising the lasers were studied. These were separated into two categories, modulation techniques which included direction modulation and modulation transfer spectroscopy and modulation free techniques which included polarisation and magnetic dichroism spectroscopy.

Chapter 9 presents the preliminary observations of atom-photon interactions in the strong coupling regime for our experiment.

Chapter 10 presents a summary of the key results from this thesis and proposes future directions for the experiment.

CHAPTER 2

CAVITY QED

2.1 The Jaynes-Cummings Hamiltonian

A theoretical model to describe the interaction of a single atom and light in a cavity comes in the form of the Jaynes-Cummings model [31]. This model, developed in 1963 describes the interaction of a single two level atom at rest with the electro-magnetic field of a single mode cavity. The Hamiltonian for the model is given by

$$H_{JC} = H_{atom} + H_{mode} + H_{int}, \tag{2.1}$$

where H_{atom} is the Hamiltonian for a two level atom with ground and excited state $|g\rangle$ and $|e\rangle$ respectively, given by

$$H_{atom} = \hbar\omega_a \sigma_+ \sigma_-, \tag{2.2}$$

where ω_a is the resonant angular frequency of the atomic transition, σ_+ is the atomic raising operator given by $|g\rangle\langle e|$ and σ_- is the atomic lowering operator given by $|e\rangle\langle g|$. H_{mode} is the Hamiltonian for a single cavity mode given by

$$H_{mode} = \hbar\omega_a \alpha^\dagger \alpha, \tag{2.3}$$

where $\alpha^\dagger$ and α are the photon creation and annihilation operators respectively, which obey the canonical commutation relation $[\alpha, \alpha^\dagger] = 1$. H_{int} is the interaction Hamiltonian describing the reversible exchange of excitation between the cavity mode and the atom and is given by

$$H_{int} = \hbar g(\alpha^\dagger \sigma_- + \alpha\sigma_+), \tag{2.4}$$

where g describes the coupling strength between the cavity mode and the atom and is given by

$$g = \sqrt{\frac{\mu^2 \omega_c}{2\hbar\epsilon_0 V}}, \tag{2.5}$$

where μ is the reduced dipole matrix element for the atomic transition and V is the mode volume for the cavity mode.

The full Jaynes-Cummings Hamiltonian in the dipole[1] and rotating wave[2] approximations is given by

$$H_{JC} = \hbar\omega_a \sigma_+ \sigma - + \hbar\omega_c \alpha^\dagger \alpha + \hbar g(\alpha^\dagger \sigma_- + \alpha\sigma_+). \tag{2.6}$$

In this closed atom-cavity system the basis vectors can be written as tensor products of the atomic states $|g\rangle$, $|e\rangle$ and the cavity Fock states $|n\rangle$ to obtain the product states $\{|g,0\rangle, |e,0\rangle, |g,1\rangle, |e,1\rangle .....\}$. These product states can be represented in the "dressed state" basis as $|+,n\rangle, |-,n\rangle$ and are given by

$$\begin{aligned} |+,n\rangle &= \cos\theta\,|n-1,e\rangle + \sin\theta\,|n,g\rangle\,, \\ |-,n\rangle &= -\sin\theta\,|n-1,e\rangle + \cos\theta\,|n,g\rangle\,, \end{aligned} \tag{2.7}$$

where the mixing angle

$$\tan(\theta) = \frac{2g\sqrt{n}}{(\omega_a - \omega_c) + \sqrt{4g^2 n + (\omega_a - \omega_c)^2}}. \tag{2.8}$$

The corresponding energy eigenvalues are given by

$$E_{n,\pm} = \hbar n\omega_c + \frac{1}{2}\hbar(\omega_a - \omega_c) \pm \frac{1}{2}\hbar\sqrt{4g^2 n + (\omega_a - \omega_c)^2}. \tag{2.9}$$

The splitting between energy levels for a given n is given by

$$E_{n,+} - E_{n,-} = \sqrt{4g^2 n + (\omega_a - \omega_c)^2}. \tag{2.10}$$

For the case when the cavity and the atom are simultaneously resonant at the same frequency, i.e $\omega_a - \omega_c = 0$ and there is no coupling, i.e $g = 0$ the splitting between the energy levels is zero and eigenlevels of the atom-cavity system are degenerate. For values of $g < 0$ this degeneracy is lifted and the eigenstates are symmetrically split by $2\sqrt{n}g$. This splitting is known as the Jaynes-Cummings ladder as shown in figure 2.1.

[1]The dipole approximations assumed the size of the atom is such that the field of the cavity mode is constant across the whole atom

[2]Where $\omega_a - \omega_c \ll (\omega_a, \omega_c)$

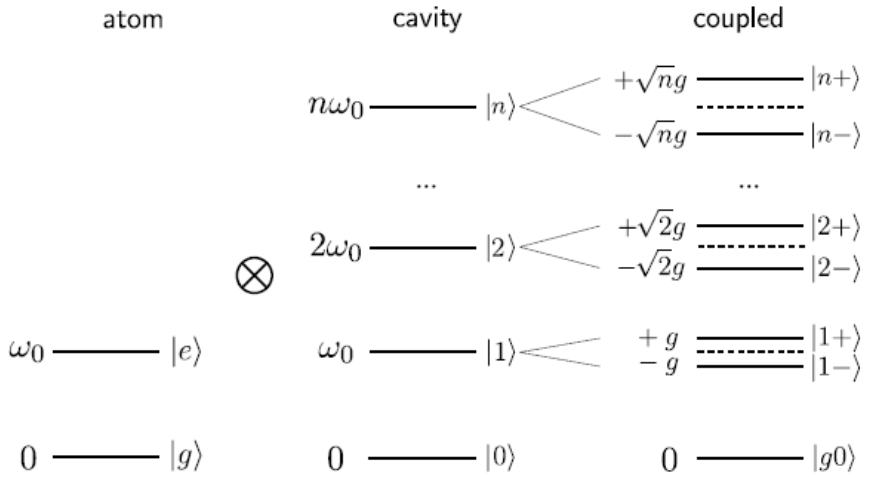

Figure 2.1: Jaynes-Cummings ladder for the dressed state of a coupled atom-cavity system.

Limiting our argument to just the first exited state (n=1), the frequency splitting of this state is $2g$ and commonly referred to as the Vacuum Rabi splitting. This splitting can be observed spectroscopically by scanning a probe laser through the cavity and observing the transmission.

2.2 Master Equation

The above description of the Jaynes-Cummings model is for a closed system without losses. While it is useful for showing the basic phenomena of a coupled atom-cavity system, for a more realistic description of the system in an experimental setting, the interaction of the system with the environment must be accounted for. Generally speaking this system interacts with the environment through two main mechanisms, namely, spontaneous emission of photons by the atom at a rate γ and through loss of photons from the cavity mirrors at a rate κ. These mechanisms are a source of dissipation to the system and their time evolution can be modeled using the master equation [7]

$$\dot{\rho} = -\frac{i}{h}[H_{JC}, \rho] + L\rho, \tag{2.11}$$

where ρ is the atom-cavity density matrix and L is the Liouville superoperator which describes the two loss mechanisms and is given by

$$L = \kappa(2\alpha\rho\alpha^\dagger - \alpha^\dagger\alpha\rho - \rho\alpha^\dagger\alpha) + \gamma(2\sigma_-\rho\sigma_+ - \sigma_+\sigma_-\rho - \rho\sigma_+\sigma_-). \tag{2.12}$$

This equation assumes the Born approximation [8], which neglects second and higher-order terms of the system-environment interaction and assumes the system evolves linearly and the Markov approximation [8], which assumes the environment has no memory[1] and its influence on the system only depends on the current state of the system and not its history.

As photons are being lost at the cavity mirrors, a near resonant laser can be used to pump photons into the cavity from one of these mirrors. This pumping can be described by a Hamiltonian, which is added to the Jaynes-Cummings Hamiltonian as follows

$$\begin{aligned} H_{JC} &= H_{JC} + H_p, \\ H_p &= -i\hbar\eta(\alpha - \alpha^\dagger), \end{aligned} \tag{2.13}$$

where η is the pump strength given by $\eta = \sqrt{J_{in}\kappa}$ and J_{in} is the photon flux in photons/sec.

Generally speaking the master equation cannot be solved analytically. However an approximate solution can be reached when the cavity field is treated semi-classically. Assuming α is a coherent state with $\alpha = \langle\alpha\rangle$ and we are in the limit of weak atomic excitation, it is given by the following Heisenberg equations of motion for $\langle\alpha\rangle$, $\langle\sigma_+\rangle$ and $\langle\sigma_-\rangle$

$$\begin{aligned} \frac{d}{dt}\langle\alpha\rangle &= -(\kappa + i\Delta_c)\langle\alpha\rangle + \eta + ig\langle\sigma_-\rangle, \\ \frac{d}{dt}\langle\sigma_-\rangle &= -(\gamma + i\Delta_a\langle\sigma_-\rangle + ig\langle\alpha\rangle[1 - 2\langle\sigma_+\sigma_-\rangle], \\ \frac{d}{dt}\langle\sigma_+\sigma_-\rangle &= -2\gamma\langle\sigma_+\sigma_-\rangle + ig[\langle\alpha\sigma_+\rangle - \langle\alpha^*\sigma_-\rangle], \end{aligned} \tag{2.14}$$

where Δ_a and Δ_c are the detunings of the atomic transition and cavity mode with respect to the pump laser ω_l defined by $\Delta_a = \omega_l - \omega_a$ and $\Delta_c = \omega_l - \omega_c$. These equations have steady state solutions of the form

$$\begin{aligned} \langle\alpha\rangle &= \frac{1}{\widetilde{\kappa}}[\eta + ig\langle\sigma_-\rangle], \\ \langle\sigma_-\rangle &= \frac{ig\alpha}{\widetilde{\gamma}}[1 - 2\langle\sigma_+\sigma_-\rangle], \\ \langle\sigma_+\sigma_-\rangle &= \frac{g^2|\alpha|^2/|\widetilde{\gamma}|^2}{1 + 2g^2|\alpha|^2/|\widetilde{\gamma}|^2}, \end{aligned} \tag{2.15}$$

where $\widetilde{\kappa}$ and $\widetilde{\gamma}$ are new variables for the two decay rates, given by $\widetilde{\kappa} = \kappa + i\Delta_c$ and $\widetilde{\gamma} = \gamma + i\Delta_a$. From these equations an expression can be obtained for the cavity field amplitude, given by

$$\langle\alpha\rangle = \frac{\eta}{\widetilde{\kappa}}\frac{1}{1 + 2\widetilde{C}}, \tag{2.16}$$

[1]Correlations within the environment and between the system and the environment decay much faster than the timescale of the evolution of the density matrix.

where the new variable $\widetilde{C}$ is the single atom cooperativity. From this expression of the field amplitude the mean number of photons in the cavity mode can be calculated using the relation $\langle n \rangle = |\langle \alpha \rangle|^2$ which gives

$$\langle n \rangle = \frac{\eta^2}{|\widetilde{\kappa}^2|} |\frac{1}{1 + 2\widetilde{C}}|^2. \tag{2.17}$$

For an empty cavity the mean photon number is given $\left(\eta/\widetilde{\kappa}\right)^2$.

2.3 Strong Coupling: One to Many Atoms

As stated earlier, κ and γ account for dissipation in the system. In order to observe cavity-atom dynamics it is necessary to overcome these processes. This is achieved when the coupling strength constant $g \gg (\gamma, \kappa)$, known as the strong coupling regime. For $g \ll (\gamma, \kappa)$ scanning the pump laser frequency through the cavity and observing the transmission on a photo-diode results in the familiar Lorentzian lineshape centered around $\Delta_c = 0$. When $g \gg (\gamma, \kappa)$ the excited state energy level spitting of the coupled atom-cavity system described earlier can be observed in the transmission signal as a double peaked feature separated by $2g$ and is shown graphically in figure 2.2, commonly referred to as the normal mode splitting. This observation is the benchmark signature that a system has entered the strong coupling regime.

The quality of the atom-cavity coupling is often measured by the single atom cooperativity factor $\widetilde{C}$ mentioned earlier, which on resonance is given by[1]

$$C = \frac{g^2}{2\kappa\gamma}. \tag{2.18}$$

Other hallmarks of an atom cavity system that are of note are, firstly the critical photon number. This variable given by

$$n_0 = \frac{\gamma^2}{2g^2}, \tag{2.19}$$

denotes the number of photons needed to saturate an atom in a system on resonance and be able to observe non-linear effects. The other is the critical atom number, which is given by

$$N_0 = \frac{2\gamma\kappa}{g^2}, \tag{2.20}$$

and is the inverse of the single atom Cooperativity. It denotes the number of atoms needed in the cavity

[1]Note that on resonance $\widetilde{C}$ reduces to C.

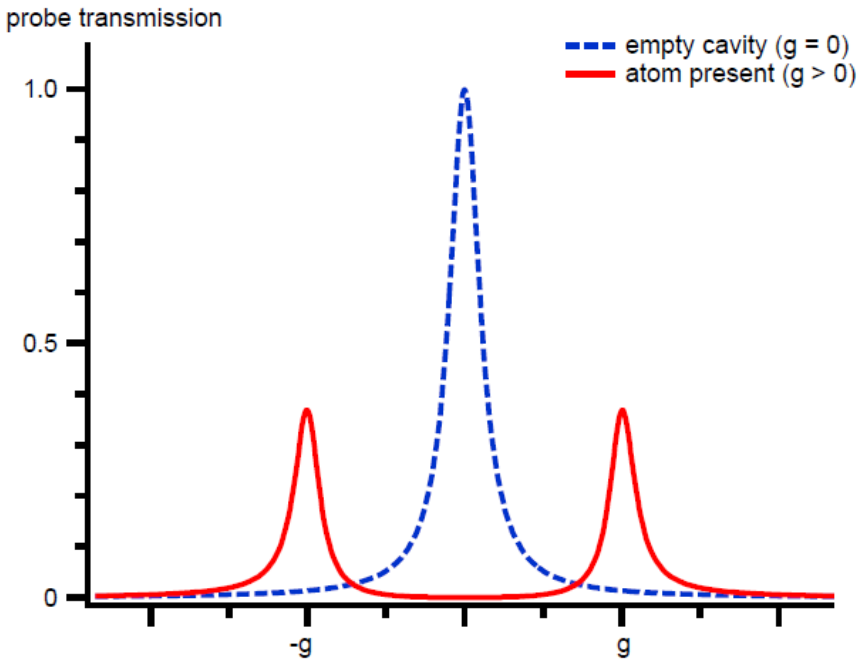

Figure 2.2: Normal mode splitting of a coupled atom-cavity system.

mode to observe a non-linear switching of the optical response. For a system with $n_0 < 1$ the interaction between an atom and a single cavity photon will have observable quantum effects and similarly when $N_0 < 1$ a single atom will have a similar effect on a cavity mode.

So far our discussion has been limited to the case of one atom coupled to a cavity mode, it is also possible to model the interaction of several atoms coupled to a cavity mode. This treatment begins with an extension of the Jaynes-Cummings model to include many atoms. This extension is known as the Tavis-Cummings model [60], [61] and is given by the Hamiltonian

$$H_{TC} = \hbar\omega_a S_z + \hbar\omega_c \alpha^\dagger \alpha + \hbar g(\alpha^\dagger S_- + \alpha S_+, \tag{2.21}$$

where $S_{\pm,z}$ are the collective atomic operators, given by

$$S_\pm = \sum_{i=1}^{N} S_\pm^{(i)} \ \ and \ \ S_z = \sum_{i=1}^{N} S_z^{(i)}, \tag{2.22}$$

where N is the number of atoms and $S^{(i)}_{\pm,z}$ represents a set of two level atoms whose spin operators are given by

$$S^{(i)}_{-} = |g_i\rangle \langle e_i|\,,\ \ S^{(i)}_{+} = |e_i\rangle \langle g_i|\ \ and\ \ S^{(i)}_{z} = \frac{1}{2}(|e_i\rangle \langle e_i| - |g_i\rangle \langle g_i|), \tag{2.23}$$

where $|g_i\rangle$ and $|e_i\rangle$ are the ground and excited state respectively for the ith atom. In the limit of low collective excitation ($n << N$), an approximate solution for the eigenenergies can be found and has the form

$$E_{n,\pm} \approx (n - \frac{N}{2})\omega_c - \frac{1}{2}n(\omega_a - \omega_c) \pm \sqrt{4g^2N + (\omega_a - \omega_c)^2}. \tag{2.24}$$

From this expression it can be seen that the coupling constant g now carries a $\sqrt{N}$ dependence and this new variable is commonly referred to as the collective coupling constant and is given by $g_{coll} = \sqrt{N}g$. This also leads on to a new expression for the cooperativity, know as the Collective Cooperativity factor which is given by

$$C_{coll} = \frac{g^2N}{2\kappa\gamma}. \tag{2.25}$$

Collective coupling of atoms to a cavity mode has the special feature that where the single atom coupling constant for the system may have been much less than γ and κ and thus not in the strong coupling regime, by having collective coupling of many atoms in the cavity it is possible for the system to reach the strong coupling regime by utilizing this $\sqrt{N}$ enhancement. The collective normal mode splitting can be observed spectroscopically by scanning a probe laser through the cavity and observing the transmission as the atom number of the system is increased.

CHAPTER 3

EXPERIMENT OVERVIEW

This chapter details the overall aim and plan for the experiment performed. Creating a cold atom experiment requires the cooling and trapping of atoms to milli-Kelvin temperatures. This is done through the use of a magneto-optical trap (MOT). A MOT consists of three paired counter-propagating lasers incident on an atom cloud trapped in a magnetic field. When atoms in the cloud move, they are Doppler shifted into resonance with the counter-propagating laser in that direction. When the atom absorbs photons from the laser beam, atomic momentum and hence velocity decreases. This effect occurs in all six Cartesian directions.

3.1 Plan

This experiment aims to interface cold ^{39}K atoms with an optical ring cavity. Cooperative behavior of the atoms can be observed through their common interaction with the cavity mode. In order to observe this cooperative behavior, the system has to enter the "strong coupling regime" as detailed in the previous chapter. The experiment is conducted inside a vacuum chamber in the ultra-high vacuum (UHV) regime of 10^{-9} to 10^{-11} mbar. At this pressure the lifetime of MOT is increased as there are less collisions with background atoms. For simplicity, this experiment operates out of a single science chamber, where the atoms are loaded directly into the MOT from background. The MOT itself is also located at the center of the cavity mode. This way, no moving transitions of the atoms or the cavity are needed during the experimental procedure. Once the MOT is created and interfaced with the cavity, the main aim is to observe the strong coupling of the atoms to the cavity. This is done by probing the cavity with a resonant laser to observe the normal mode splitting.

3.2 Setup

To create the experiment, the first step is the development of the laser systems. For cooling and trapping of atomic species, lasers are required whose frequencies are near the cooling transitions of the atoms. These lasers have to be stable to within the natural linewidth of the atoms, typically a few MHz. For this, custom built extended cavity diode lasers (ECDLs) are used. Three laser are used, a master laser and two slave lasers. The master laser is actively stabilised using an atomic locking scheme, specifically the magnetically induced dichroism technique. The two slave lasers are locked relative to the master laser using frequency offset lock technique. The locking schemes are explained in greater detail in chapter 8.

One slave laser acts as the cooling laser and the other as the repump laser for the MOT. To generate the MOT light, the cooling and repump laser are amplified using a master oscillator power amplifier (MOPA). After the MOPA the light is split into three components and coupled into polarisation maintaining fibres. The output of the fibres are sent through beam expanders and form the three paired counter-propagating beams that generate the MOT. The next step is the development of the vacuum system. The system is built around a spherical octagon chamber. Eight viewports provide optical access, one port contains the atom source and on the other side one port is connected to the vacuum pumping system.

The ring cavity is located in the middle of the main chamber. Access holes on the cavity allow the MOT beams to intersect with the cavity mode. A transfer cavity used to lock far off-resonant lasers in the experiment is developed as part of this thesis. It is however not used as part of the main experiment performed for the thesis, but instead be used for subsequent experiments which require the ring cavity to be stabilised.

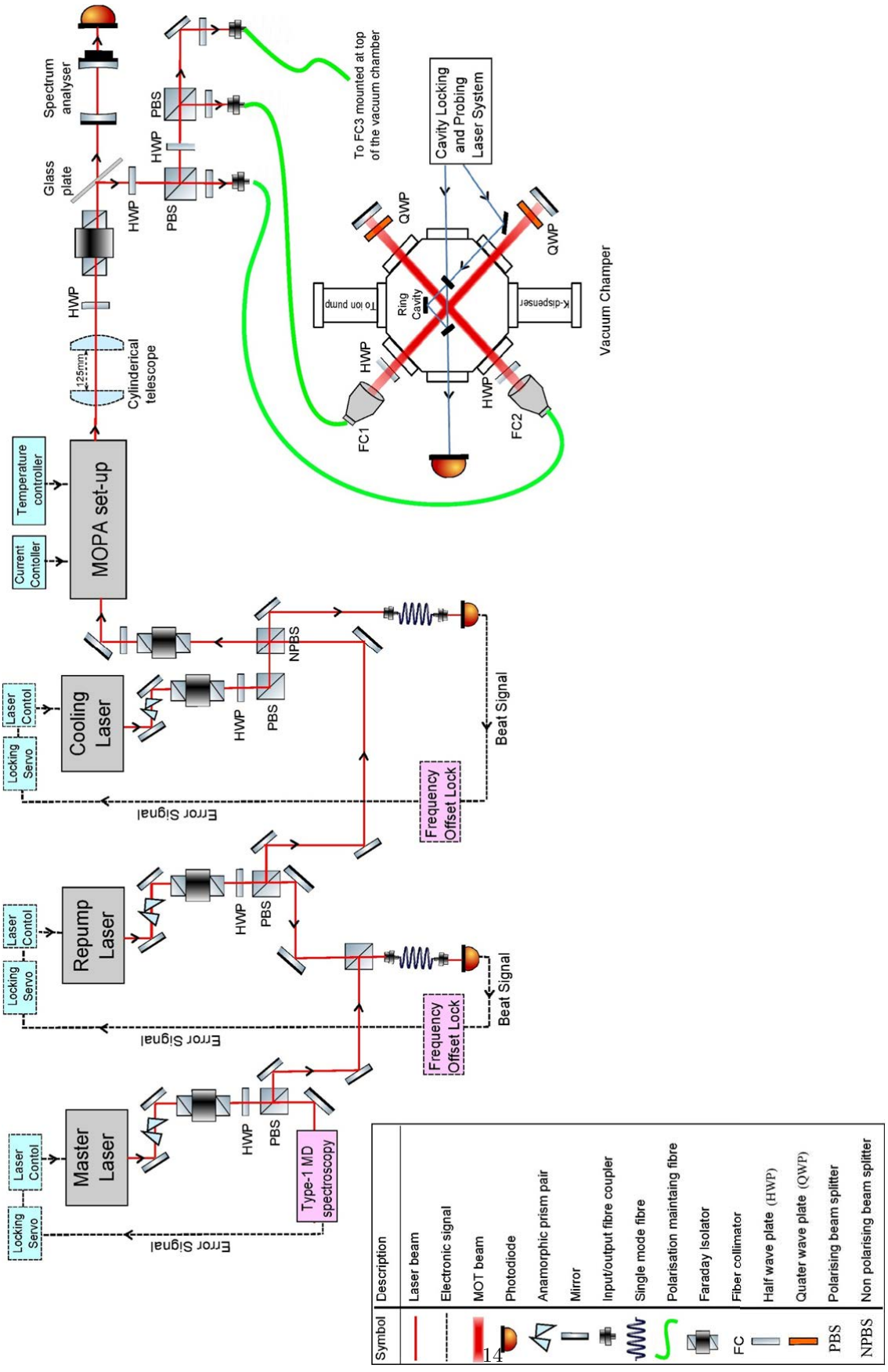

Figure 3.1: Schematic of the full experimental setup.

CHAPTER 4

OPTICAL CAVITIES

4.1 Resonant Character of Cavities

This section will detail an elementary analysis of the resonant character of optical cavities mainly derived from [55]. For simplicity we will assume than the light entering the cavity are plane waves and the cavity mirrors are flat. Effects such as diffraction will be ignored. For convenience this treatment will be generalized to be able to describe standing wave cavities or ring cavities on equal footing. Optical cavities are formed when light propagates in a closed path between two or more reflecting surfaces i.e mirrors separated by a distance or path length p. Each mirror has an associated field amplitude reflection and transmission coefficient, quantified by $r_{1,2,3...}$ and $t_{1,2,3...}$. Firstly let us consider the case when a plane wave encounters just the input mirror and is divided into two partial waves. One part is transmitted through the mirror, the other reflected. The transmitted and reflected electrical field amplitudes can be written as

$$E_{tran} = -itE_{inc}, \tag{4.1}$$

$$E_{refl} = rE_{inc}. \tag{4.2}$$

where E_{inc} is the incident electrical field amplitude. Provided the closed path condition is satisfied, a circulating field will build up inside the cavity, which we denote E_{circ}. With each round trip the wave accumulates a phase shift $e^{(i\omega p/c)}$ associated with the round trip, where ω is the angular frequency and c is the speed of light. This circulating field after one round trip will return with a complex round trip gain g_{rt} given by

$$g_{rt}(\omega) = r_1 r_2 (r_3 ...) e^{\phi}, \tag{4.3}$$

where $\phi = [i\omega p/c]$.

This circulating field therefore consists of the vector sum of the portion of the initial wave that transmitted through the input mirror denoted $-it_1 E_{inc}$ plus a contribution of the circulating field E_{circ} which left the same point one round trip earlier and is given in the form

$$E_{circ} = -it_1 E_{inc} + g_{rt}(\omega) E_{circ}. \tag{4.4}$$

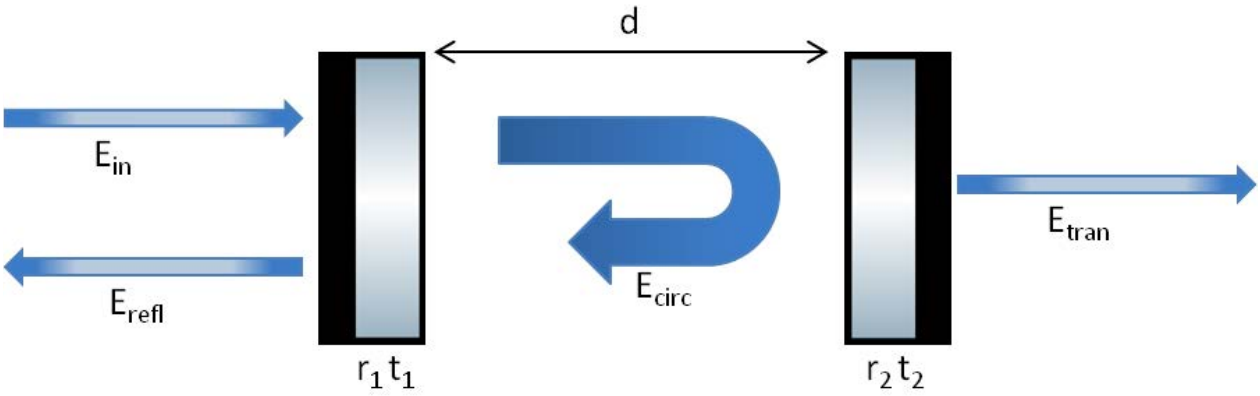

Figure 4.1: A schematic of an optical cavity. The cavity is formed by two mirrors separated by a distance d. Each mirror has an associated reflection and transmission field amplitude coefficients r_1, r_2 and t_1, t_2, respectively. A field of amplitude E_{in} impinges on mirror one, leading to a circulating field, E_{circ} inside the cavity, a transmitted field, E_{tran} and a reflected field, E_{refl}.

Relating this circulating field to the incident field we get the expression

$$\frac{E_{circ}}{E_{inc}} = \frac{-it_1}{1 - g_{rt}(\omega)}. \tag{4.5}$$

A similar treatment can be done for the reflected and transmitted fields. For the reflected field, this is the combination of the instantly reflected field, $r_1 E_{inc}$ and a component of the circulating field E_{circ} that has retransmitted out of the mirror M_1 and is given by

$$E_{refl} = r_1 E_{inc} - it_1 (g_{rt}(\omega)/r_1) E_{circ}. \tag{4.6}$$

Relating this reflected field to the incident field we get the expression

$$\frac{E_{refl}}{E_{inc}} = r_1 - \frac{{t_1}^2}{r_1}\frac{g_{rt}(\omega)}{1 - g_{rt}(\omega)}. \tag{4.7}$$

For the transmitted field, this is the portion of the circulating field E_{circ} that gets transmitted through the mirror, M_2 and is given by

$$E_{trans} = -it_2 e^{\frac{\phi}{2}} E_{circ}. \tag{4.8}$$

Relating this reflected field to the incident field we get the expression

$$\frac{E_{tran}}{E_{inc}} = \frac{t_1 t_2 e^{i\frac{\phi}{2}}}{1 - g_{rt}(\omega)}. \tag{4.9}$$

To calculate the intensity of the fields we use the quadratic dependence of the intensity upon the field, given by

$$\frac{I_{refl,trans}}{I_0} = \left|\frac{E_{refl,trans}}{E_0}\right|^2. \tag{4.10}$$

For the transmitted intensity this has the solution

$$I_{trans} = \frac{I_0}{1 + m\sin^2(\phi/2)}, \tag{4.11}$$

where m is given by

$$\frac{4r_1 r_2(r_{3...})}{(1 - r_1 r_2(r_{3...}))^2}. \tag{4.12}$$

The optical cavity exhibits a strong resonance behavior each time the round-trip phase shift $\omega p/c$ equals an integer multiple of 2π, i.e $\omega = \omega_q \equiv q2\pi(c/p)$, where q is an integer. This gives rises to the well known perfectly discrete peaks associated with cavities, figure 4.2, 4.3.

These resonant frequencies are known as cavity axial modes and the frequency separation between them is given by

$$\Delta\omega = \omega_{q+1} - \omega_q = 2\pi c/p = 2\pi\frac{c}{p}, \tag{4.13}$$

or more generally

$$\Delta\nu = \frac{c}{p}. \tag{4.14}$$

This is known as the Free Spectral Range (FSR) of a cavity.

Another important quantity of an optical cavity is the Half Width at Half Maximum (HWHM) which is

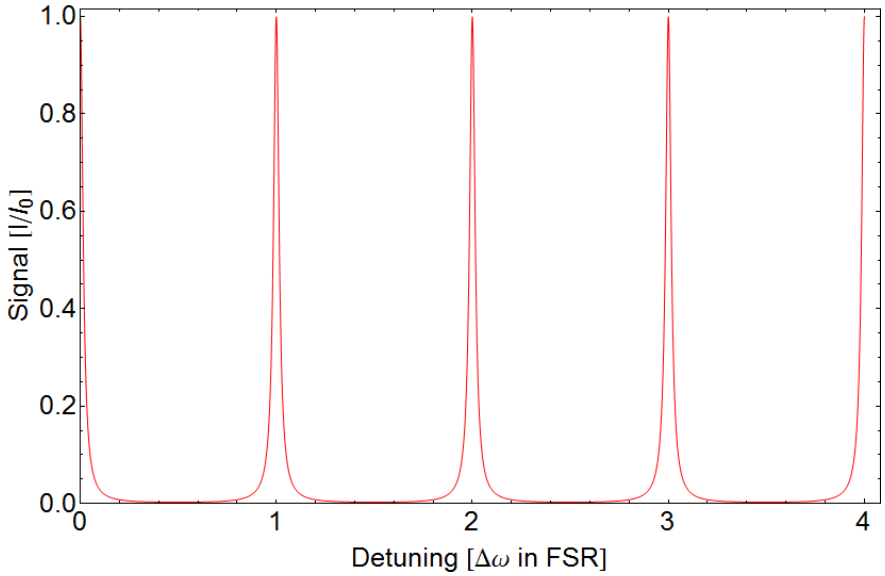

Figure 4.2: Transmission profile of a field incident on a cavity, away from resonance no light enters the cavity, upon resonance there is a sudden spike in the transmitted intensity.

the width of the resonance peak when the intensity falls to half of its maximum value and can be found to be [4]

$$\Delta\omega_{HWHM} = \frac{1}{2}\frac{2c}{\sqrt{m}2L\pi}. \tag{4.15}$$

The ratio of the FSR to the FWHM is known as the Finesse (F) and is given by

$$F = \frac{\pi}{2}\sqrt{m}. \tag{4.16}$$

The Finesse directly relates the cavity losses to the HWHM of the resonance peaks, as the losses increase they serve to effectively spread the HWHM.

4.2 Gaussian Waves

So far our discussion of optical waves in a cavity has only considered plane waves, of course this is not the same for real cavities as it ignores diffraction and wavefront curvature of the waves. A more realistic description of optical waves comes in the form of the Gaussian beam model. A brief description of this model will be given in this section.

One fundamental way of describing wave propagation is through the paraxial wave equation [40]. Elec-

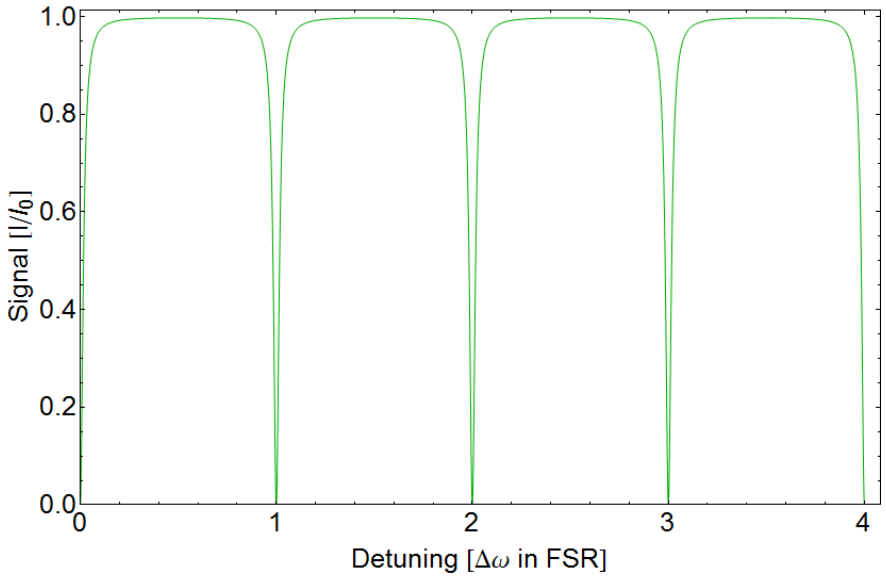

Figure 4.3: Reflection profile of a field incident on a cavity, away from resonance no light enters the cavity, upon resonance there is a sudden dip in the reflected intensity.

tromagnetic waves in free space are governed by the scalar wave equation

$$\nabla^2 u - \frac{1}{c^2}\frac{\partial^2 u}{\partial t^2} = 0, \tag{4.17}$$

where u is the field component (E_x, E_y, E_z). Assuming the wave is monochromatic the equation becomes

$$\nabla^2 u + k^2 u = 0, \tag{4.18}$$

where k is the magnitude of the wave vector of the wave. The paraxial approximation requires that the normals to the wavefront make a small angle with some fixed axis, which in our consideration will be the z-axis of Cartesian coordinate system and be modeled as

$$u(x, y, z) = \psi(x, y, z)e^{-ikz}, \tag{4.19}$$

where $\psi(x, y, z)$ is a slow varying function that is spatially modulating the wave. Substituting this equation back into the scalar wave equation gives rise to the Paraxial wave equation

$$\nabla_t{}^2\psi - 2ik\frac{\partial \psi}{\partial z} = 0, \tag{4.20}$$

where ${\nabla_t}^2$ is the transverse Laplacian ($\frac{\partial^2}{\partial x^2} + \frac{\partial^2}{\partial y^2}$).

One simple solution to the paraxial wave equation can be found by using a trial solution of the form

$$\psi(x, y, z) = P(z)e^{[-ik\frac{x^2+y^2}{2q(z)}]}, \tag{4.21}$$

where P(z) and q(z) are the phase term and complex beam parameter respectively. The complex beam parameter q can be written in terms of two real parameters R and ω in the form

$$\frac{1}{q(z)} = \frac{1}{R(z)} - i\frac{\lambda}{\pi\omega(z)^2}, \tag{4.22}$$

where R is the wavefront radius and ω is the waist radius.

Using the complex beam parameter it is possible to specify the properties of a Gaussian beam at any point as it propagates along the z-axis. From figure 4.4 showing the focusing properties of a Gaussian beam it can be seen that it never comes to a point but rather achieves a minimum spot size, whose $1/e^2$ waist radius is denoted ω_0. Using this minimum waist as a reference it is convenient to describe the evolution of *R(z)* and $\omega(z)$ along the z-axis with respect to ω_0 in the form

$$\omega(z) = \omega_0[1 + (\frac{z}{z_r})^2]^{1/2}, \tag{4.23}$$

and

$$R(z) = z + \frac{{z_r}^2}{z}, \tag{4.24}$$

where z_r is the distance from the waist where it equals $\sqrt{2}\omega_0$, known as the Rayleigh range and is given by $\pi\omega_0^2/\lambda$.

From the P(z) phase term stated in equation 4.21 it can be shown after a bit of algebra that the phase shift of a Gaussian wave ($i\phi$) is given by

$$i\phi = ikz - itan^{-1}\frac{z}{z_r}. \tag{4.25}$$

The first term is the normal phase shift associated with a plane wave as described in section 4.1, the second term is known as the Gouy phase shift which is the phase shift associated with the discrepancy from true planarity [22]. The origin of this Gouy phase continues to be a matter of debate, for example, it has been associated with Heisenberg's uncertainty principle, Berry's geometric phase, Kirchhoff diffraction integral

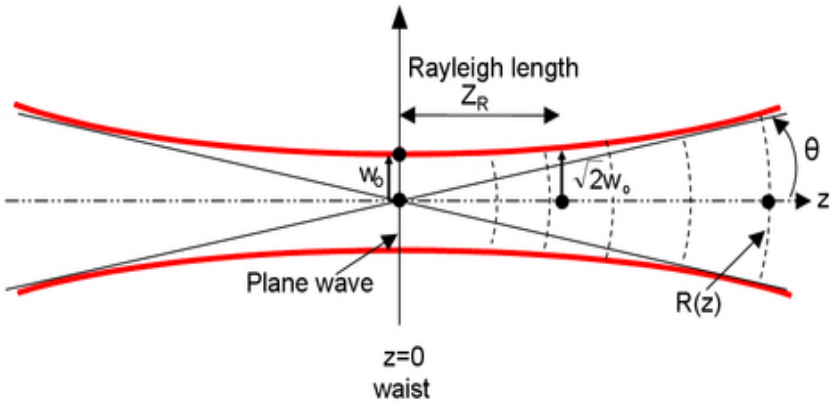

Figure 4.4: Gaussian beam near a focus showing the radial intensity profile and spherical wavefronts.

[25] [59] [5], to name but a few. What is well understood is that it manifests itself in the form of a net 180 degree phase shift through the focus of a Gaussian beam relative to a plane wave with equal wave vector as shown in figure 4.5. It plays a very important role in determining the resonant frequencies of an optical cavity as higher-order modes have stronger Gouy phase shifts.

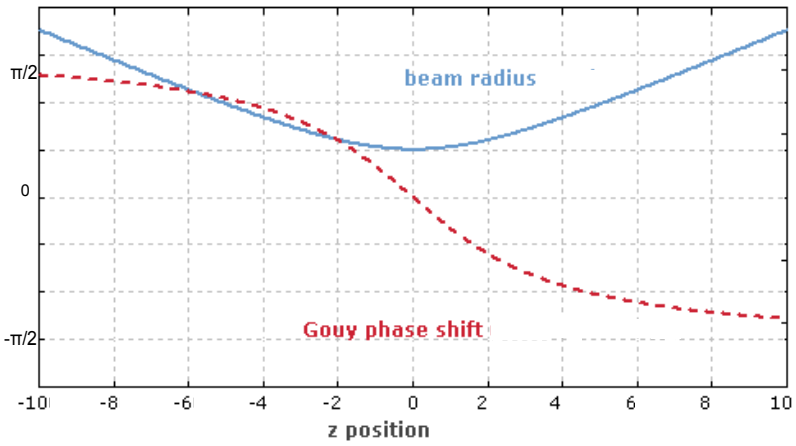

Figure 4.5: Gouy phase shift of π about the focus of a Gaussian beam.

4.3 Higher-Order Gaussian Waves

So far the Gaussian beam we have considered is only one (the simplest) form of an infinite number of possible modes. In order to be able to describe an arbitrary wave we need a complete set of functions, each a solution

of the paraxial wave equation. The wave would then be a linear combination of all these functions. After some algebra [51] it can shown that this Gaussian wave can be described by

$$u(x,y,z)_{nm} = \frac{\omega_0}{\omega(z)} H_n(\sqrt{2}\frac{x}{\omega}) H_m(\sqrt{2}\frac{y}{\omega}) exp^{-i(kz-\Phi(m,n;z))-i\frac{k}{2q}(x^2+y^2)}, \tag{4.26}$$

where

$$\Phi(m,n;z) = (m+n+z)tan^{-1}(z/z_r), \tag{4.27}$$

where n and m are integers, $\Phi(m,n;z)$ is the Gouy phase and the functions H_n and H_m are Hermite polynomials of order n and m. When $n = m = 0$, this expression reduces to the lowest order Gaussian beam described in section 4.2. Depending on the value of n and m the resulting waves will have very different cross-sectional shapes as shown in figure 4.6. These wave distributions are collectively known as Hermite-Gaussian modes, or more commonly TEM_{nm} (Transverse Electromagnetic) modes.

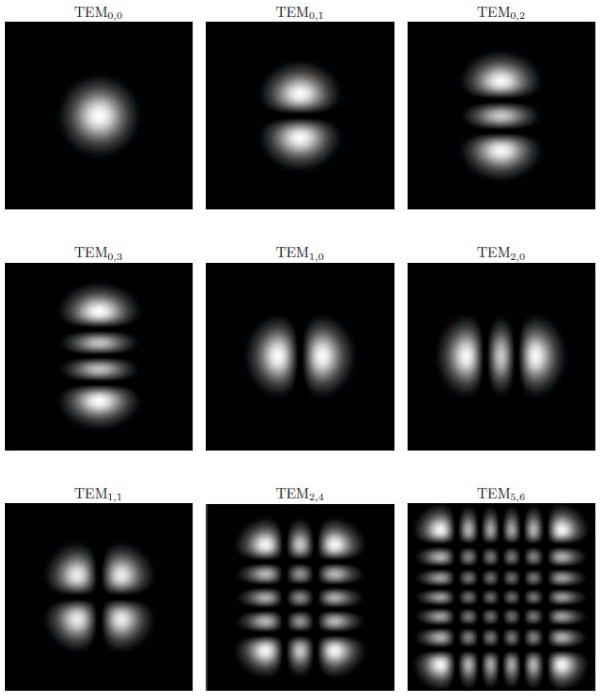

Figure 4.6: Spatial energy distribution for Hermite-Gaussian modes.

4.4 ABCD Matrix

Despite the added complexity, higher-order Gaussian waves can be still be describes by the same complex beam parameter q derived for the lowest order Gaussian wave in section 4.2. A useful way of calculating q is the so called ABCD matrix [2]. Originally used to describe the propagation of light rays as they pass through various optical elements. It can also be employed to find solutions of q as the Gaussian wave propagates through or between various optical elements. Firstly let us consider a single paraxial ray which is completely described by a two element column vector containing the height y of the ray above the axis and the slope y', of the ray. As it passes through various optical elements there is a change in displacement and slope. The ray at the output of the element is given by

$$\begin{pmatrix} y_2 \\ y_2' \end{pmatrix} = \begin{pmatrix} A & B \\ C & D \end{pmatrix} \begin{pmatrix} y_1 \\ y_1' \end{pmatrix}.$$

Every optical element has an associated ABCD matrix, given below

$$\begin{pmatrix} 1 & d \\ 0 & 1 \end{pmatrix}, \begin{pmatrix} 1 & 0 \\ -1/f & 1 \end{pmatrix}, \begin{pmatrix} 1 & 0 \\ -2/R & 1 \end{pmatrix}, \begin{pmatrix} 1 & d/n \\ 0 & 1 \end{pmatrix},$$

for free-space distance d, thin lens with focal length f, mirror with radius of curvature R and slab with thickness d and index of refraction n respectively. To satisfy the closed path condition stated in section 4.1 q must replicate itself after a round trip. q can then be represented as

$$q = \frac{Aq + B}{Cq + D}, \tag{4.28}$$

which has the solutions:

$$\frac{1}{q} = \frac{D - A}{2B} \pm \frac{1}{2B}\sqrt{(A - D)^2 + 4BC}. \tag{4.29}$$

4.5 Higher-Order Gaussian waves in a Cavity

With a full description of Gaussian waves given, it is now possible to describe how these waves behave when placed inside a cavity. The flat mirrors detailed in section 4.1 will be replaced with curved mirrors since to satisfy the closed path condition stated in section 4.1 the radius of curvature of the mirrors, R_1, R_2 has to match the radius of curvature of the wave. Although in practice we will actually have mirrors with a given

radius of curvature and fit a Gaussian wave to those mirrors. In what follows it is convenient to describe the cavity geometry in terms of two dimensionless parameters g_1 and g_2 [55], which for a standing wave cavity are given by

$$g_1 \equiv 1 - \frac{L}{R_1}, \tag{4.30}$$

$$g_2 \equiv 1 - \frac{L}{R_2}, \tag{4.31}$$

where L is the distance between the mirrors i.e *(p/2)* and are called the 'cavity g parameters'. After some algebra it can be shown that the Higher-order Gaussian beam Gouy phase $\Phi(m, n; z)$ along the cavity length can be given by

$$\Phi(m, n; z) = cos^{-1} \pm \sqrt{g_1 g_2}. \tag{4.32}$$

The resonant frequencies of the axial plus transverse modes of the cavity are then given by

$$\nu_{(nmq)} = \left(q + (n + m + 1) \frac{cos^{-1} \pm \sqrt{g_1 g_2}}{\pi} \right) \frac{c}{p}. \tag{4.33}$$

From this expression it can be seen that the transverse mode frequencies associated with a given axial mode will have difference Gouy phase shifts and therefore difference resonance lines. This means that every axial mode resonant frequency line will have additional spectral lines associated with the Higher-order modes. A useful generalisation of this effect occurs when one has a cavity with g_1,$g_2 \rightarrow 0$, for this case the Gouy phase term in equation 4.33 $\approx 1/2$. The equation for the resonant frequencies of the axial plus transverse modes reduces to

$$\nu_{(nmq)} = \frac{1}{2} \frac{c}{p}. \tag{4.34}$$

We notice that c/p is the Free Spectral Range defined earlier. This means that the axial and transverse modes become degenerate and we get a mode spacing of 1/2FSR, this is known as the confocal cavity.

4.6 Cavity Types and Stability

Cavities are generally categorized into two sections, standing wave and traveling wave (ring) cavities as shown in figure 4.7. Standing wave cavities have a two-mirror configuration where the light bounces back and forth between the two mirrors and forms a standing wave, hence the name. Ring cavities on the other hand have three or more mirrors and the light entering the cavity circulates around the cavity in the input direction and never bounces back on itself to create a standing wave. A ring cavity can however support a standing

wave by inputing two beams in opposite directions to each other into the cavity.

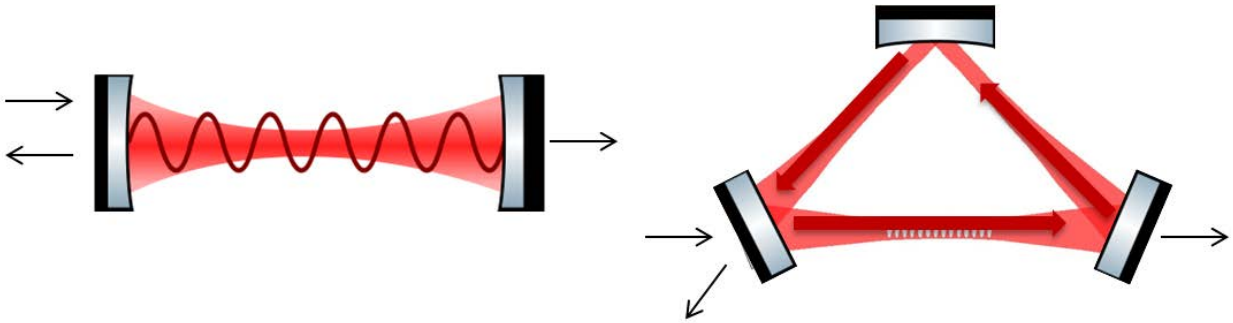

Figure 4.7: Two-mirror standing wave cavity and a three-mirror traveling wave cavity.

The simplest type of standing wave cavity is the plane-parallel cavity, described in section 4.1, consisting of two opposing flat mirrors. This cavity forms the basis of the Fabry-Perot interferometer [28]. The confocal cavity is where the mirror curvatures equal the cavity length i.e ($R_1 = R_2 = L$). Only certain values of R_1, R_2 and L will satisfy the closed path condition and it can be shown that a cavity is stable if the following condition is satisfied

$$0 \leq g_1 g_2 \leq 1. \tag{4.35}$$

A more general form of the stability criterion using the ABCD matrix of the closed path condition is given by

$$|A + D| \leq 2. \tag{4.36}$$

CHAPTER 5

THE TRANSFER CAVITY

A transfer cavity as the name suggests serves to transfer the stability of one laser on to another. Typically for cold atom experiments there is one master laser which is locked with some spectroscopic method and other lasers in the system have locks derived from this master laser. This is usually done by the means of an offset lock or injection lock. The major drawback with these methods is that the frequency of the subsequent or slave lasers has to be relatively close to the master laser as they are limited by the bandwidths of the detectors used to measure the beatnote between the lasers. If one needs a laser with a very large frequency detuning to the master laser then typically this laser would need its own spectroscopic lock method. However locking to a separate spectroscopy means that the total stability of the laser systems suffers since the lasers are decoupled from each other.

A solution to this problem is the use of a transfer cavity. If one locks the transfer cavity to the master laser and then the far detuned laser to the cavity, a stability chain is created between the two lasers with a relative stability narrower than the case of two independently locked lasers. For our experiment were require a transfer cavity for locking a far off-resonant laser at 852 nm. This laser will be used to lock the ring cavity in future experiments and also serve as a dipole potential for atoms trapped in the cavity mode. This chapter will detail the design and construction of the transfer cavity, properties of the cavity that allow for very small mode spacings and methods of locking the cavity are explored.

5.1 Design of the Cavity

The cavity is machined from a brass cylinder, on one end is attached a Newport LFM-1A mirror mount housing one of the mirrors. The mount allows for course adjustment of the cavity length over a range of 5 mm. On the other end is a small custom spacer piece attached to the end of the cylinder, this piece contains

the piezo and the other mirror. The piezo is a ring actuator from Piezomechanik (HPCh 150/12-6/2) with 2 mm thickness and 12 mm diameter with a 6 mm through hole and is capable of 4 μm travel. The piezo is glued into a groove on one end of the custom spacer piece using 5-minute epoxy. On the other side of the spacer a 1 inch mirror is placed in a groove and held rigidly by three nylon m3 screws in a triangular pattern. The piezo, spacer and mirror assembly is glued to the end of the cylinder from the piezo side using 5-minute epoxy.

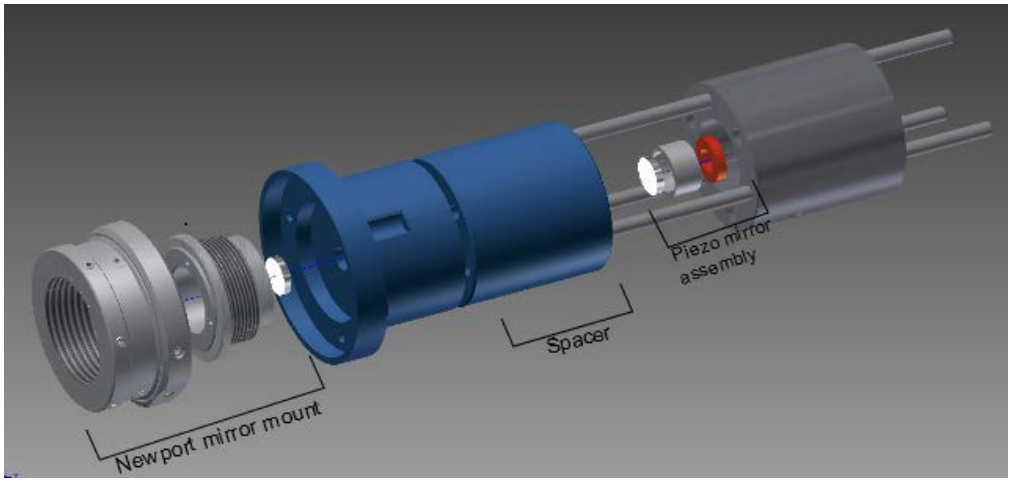

Figure 5.1: CAD drawing of the transfer cavity.

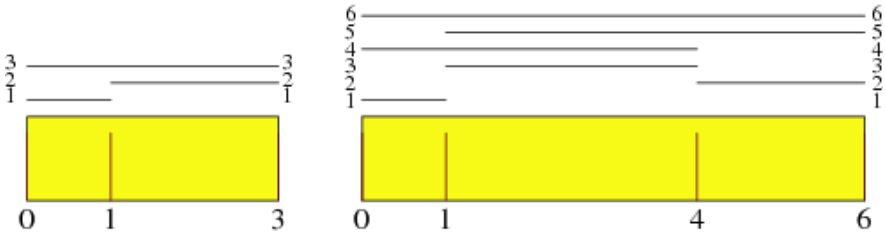

Figure 5.2: Example of 3rd order and 6th order Golomb ruler [1].

The cylinder has a 15 mm through hole to allow optical access. It is further cut into various length sections ranging from 2 cm thickness to 10 cm. This is to allow for the cavity length to be altered by choosing the appropriate amount of the sections that add up to the desired length. To maximize the number of possible length configurations the sections were divided up according to the Golomb ruler [1]. A Golomb ruler consists of a set of integer marks along an imaginary ruler with a configuration such that the difference between any two marks is distinct. This has the feature that for a ruler of a given length, it is possible to measure all

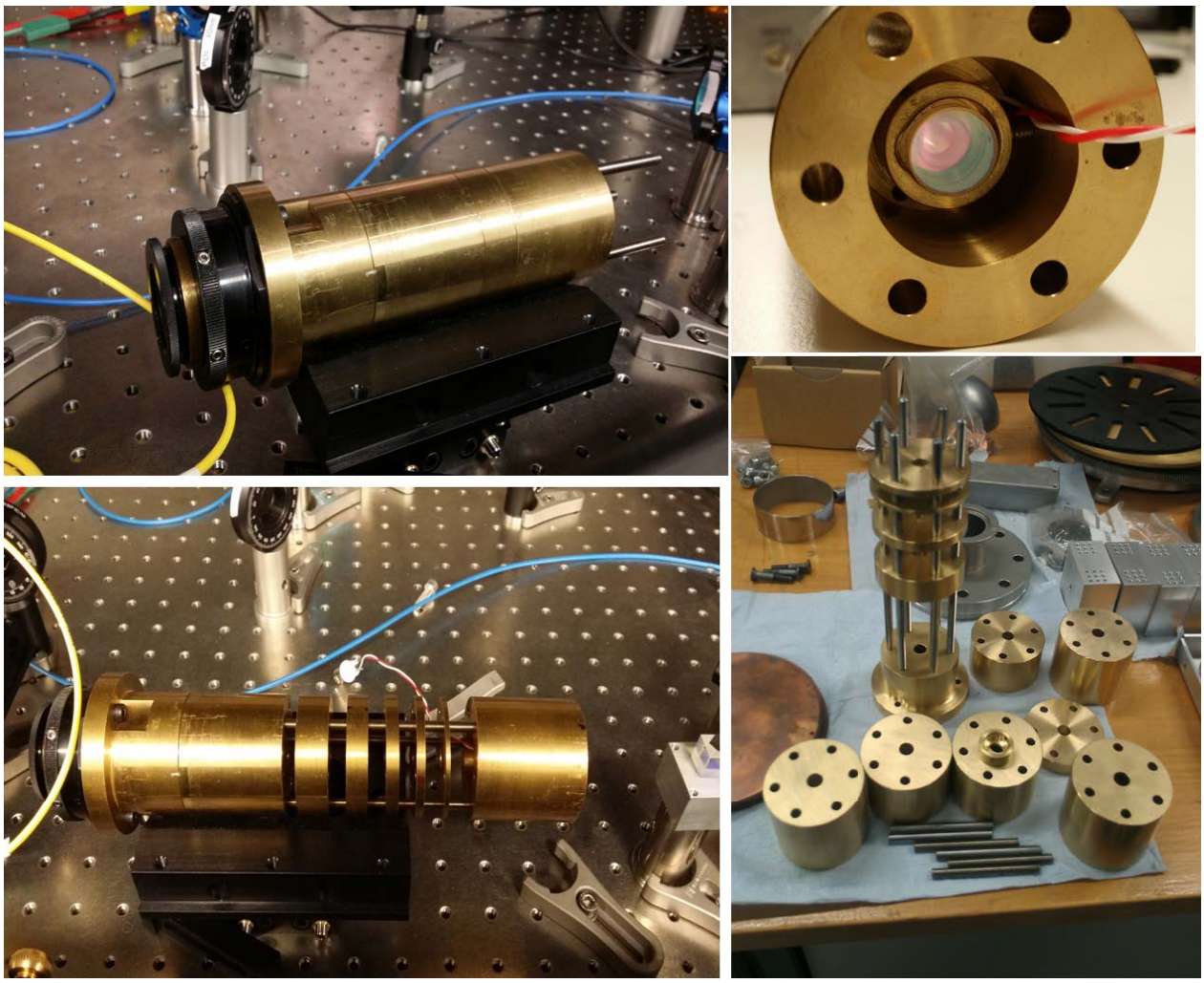

Figure 5.3: The cavity cylinder cut into sections determined by 5th order Golomb ruler.

distances up to its length. For example a ruler of 6 cm with marks at 0, 1, 4 and 6 can be cut to give sections of 1 cm, 2 cm and 3 cm.

This is an example of a 4th order Golomb ruler and it is clear that different combinations of these sections one can make a ruler of integer values from 1 to 6 cm as shown in figure 5.2. A 5th order Golomb ruler was used to cut the cavity into appropriate spacer sections as shown in figure 5.3. With this, a cavity of any length between 5 cm and 20 cm with a precision of 1cm can be made. Six m4 through holes are drilled in all the spacers, with taped holes in the end piece (housing the Newport mount). Six 10 cm metal rods are screwed into the end piece to give the cavity a skeleton for adding the desired spacers and end piece. Once a suitable length is found the cavity is bolted into placed at the ends of the rods. The cavity is placed in a

v-groove mount from Newport with 4 axis micro adjustment for alignment of the cavity. The mirrors used are from Mells Griot/CVI, 1 inch in size with a reflectivity of 99% and both have a radius or curvature of 15 cm.

5.2 The Gouy Degenerate Cavity

As shown in a previous chapter, at confocal there is a degenerate mode spacing for a cavity at half the FSR. This reduces the equation for the resonant frequencies of the axial and transverse mode to[1]

$$\nu_{(nmq)} = \frac{1}{2}\frac{c}{2L}, \tag{5.1}$$

where L is the length of the cavity. For our cavity we have a FSR of 1.5 GHz at confocal leading to a degenerate mode spacing of 750 MHz. For a fixed cavity, a laser incident on the cavity would need to be detuned into resonance with the cavity. At confocal this detuning requirement is essentially halved as lock points are now available every 750 MHz, instead of 1.5GHz. Although it is possible to get shorter mode spacings by tuning the cavity to non-degenerate modes, this is undesirable as you lose the frequency reference capability of degenerate modes. For example, with degenerate modes, a laser's frequency can be detuned a certain amount by simply counting lock points until you reach the desired frequency. Degenerate modes are also more robust against long term drifts, as the cavity can only drift an integer amount of lock points away from the desired position. Whereas for non-degenerate modes, drifts can easily mask where the original lock point was located.

To this end, investigations were done to assess how further we could exploit this feature of subdividing the FSR into shorter spaced degerenate modes. A solution came in the form of the Gouy Degenerate Cavity. This method, first described by D.Budker [14] exploits the fact that in addition to this primary degeneracy which occurs at confocal, there are additional degeneracies where the mode spacings are given by

$$\nu_{(nmq)} = \frac{1}{N}\frac{c}{2L}, \tag{5.2}$$

where $N \geq 2$. The resonant frequencies for these cases correspond to the degeneracy

$$\nu(q, k+N) = \nu(q+l, k), \tag{5.3}$$

[1]For convenience, the path length, p, has been redefined to $2L$ as we are only considering a linear cavity.

where $k = m + n$ and l is an integer. The resonance condition for the system can be expressed as

$$\frac{L}{R} = 1 - cos\left[\frac{l\pi}{N}\right], \tag{5.4}$$

where R is the radius of curvature of the mirrors. The solutions to this equation are plotted in figure 5.4. This graph can be used to locate the degenerate mode spacing positions of a cavity as a function of L/R. For a fixed value of R any desired value of N can be found by scanning the cavity length, L. To be able to utilise this method is the reason why the cavity spacers were cut into sections determined by the Golomb ruler.

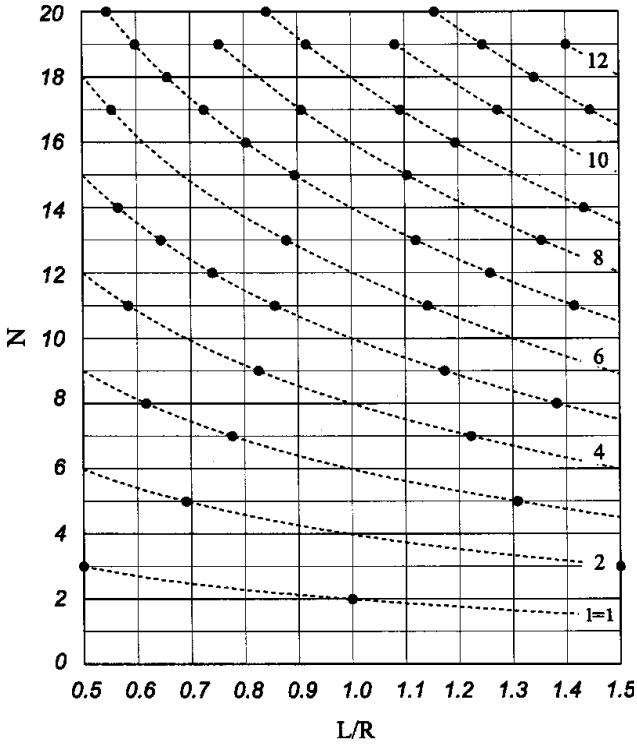

Figure 5.4: Location of the solutions of equation 5.4. This plot can be used for choosing appropriate mirror separation for a desired value of N [14].

The cavity is probed with a home-built AR coated Extended Cavity Diode Laser (ECDL) with center wavelength of 770 nm (Eagleyard, EYP-RWE-0790-04000-0750-SOT01-0000). The transmission through the cavity is incident on a Thorlabs DET100A/M photodiode and the trace observed on an oscilloscope. With the cavity setup, initial experiments involved scanning the length of the cavity while using the graph from figure 5.4 to find degenerate mode spacing positions. Numerous positions were found with a select few presented below, figure 5.5. A limitation to this method is that as you subdivide the FSR you proportionally lose

signal strength in each peak, as the total power has to be conserved. The linewidth of the cavity at confocal was found to be 5.1 ± 0.4 MHz. Since linewidth is a function of cavity length, linewidth measurements for different cavity lengths were taken and plotted, figure 5.6. In addition to showing us the variance of linewidth to cavity length this graph can be used to find an estimate of the Finesse of the cavity. Using a 1/x line fit, the Finesse of this cavity was found to be 188 ± 15 and the linewidth drifts in the range of 4-10 MHz.

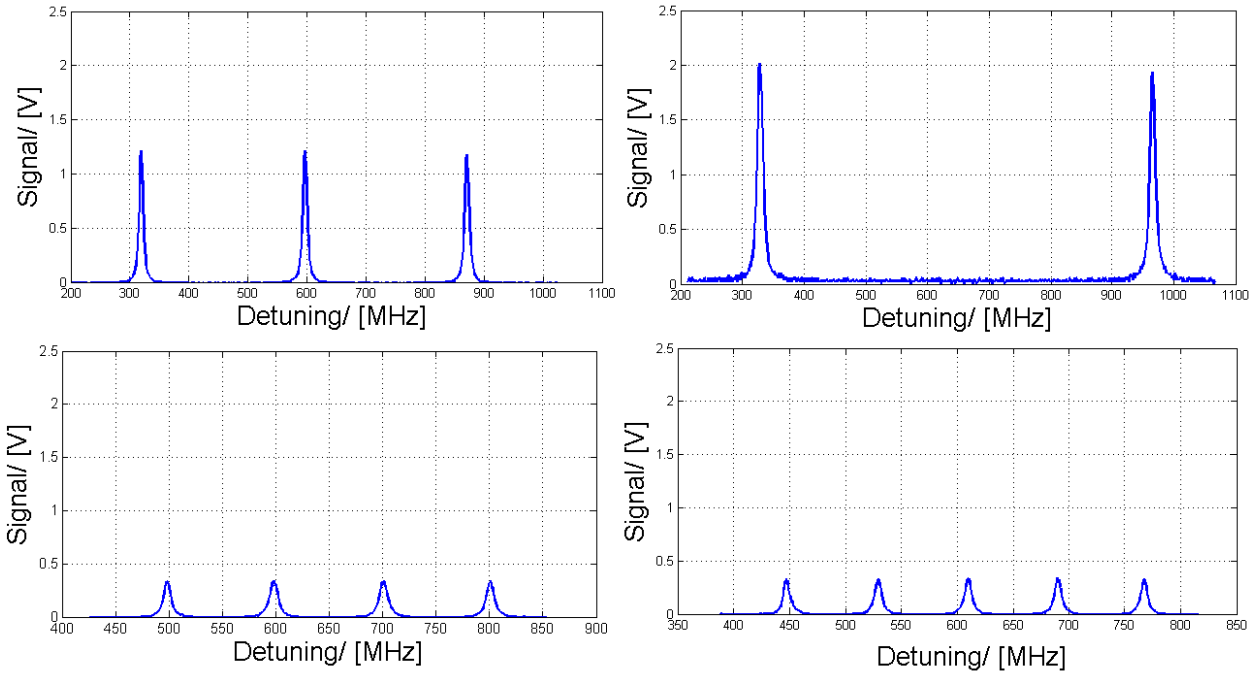

Figure 5.5: Transmission peaks showing degenerate mode spacing positions of the cavity as determined by equation 5.4, with a mode spacing of 275 MHz, 637 MHz, 100 MHz and 77 MHz. (left top - right top - left bottom - right bottom).

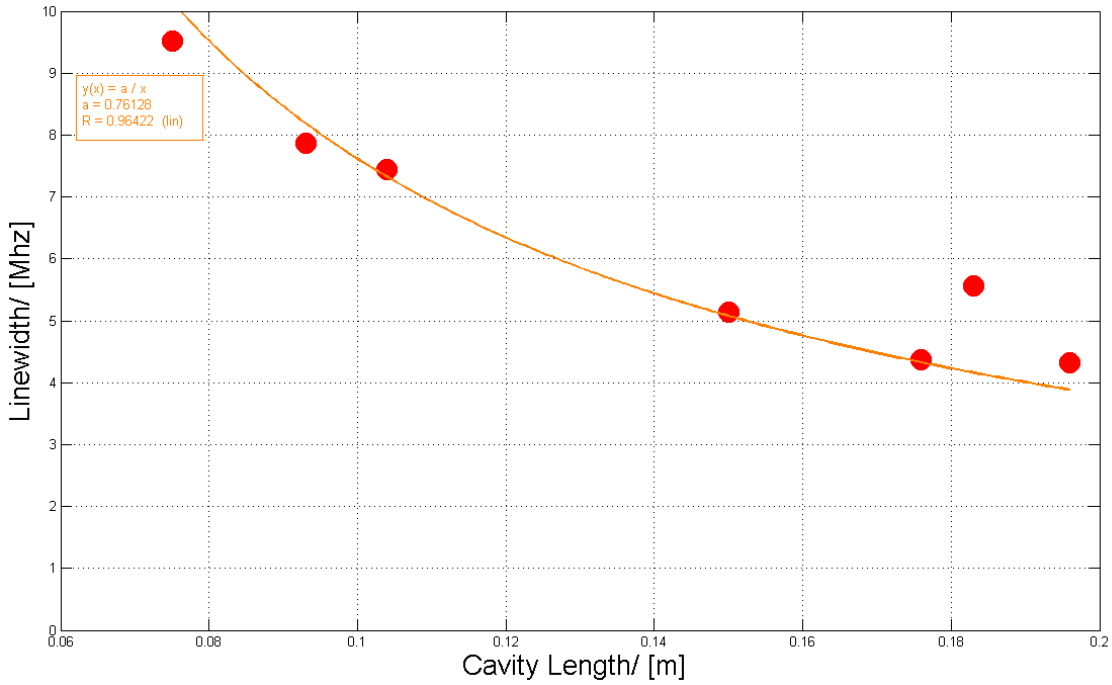

Figure 5.6: Linewidth of the cavity as a function of cavity length, a 1/x line fit is used to find an estimate of the Finesse, which was found to be 188 ± 15.

5.3 The Hänsch-Couillaud Laser Lock Technique

5.3.1 Background

The first method for locking the cavity to be discussed is the Hänsch-Couillaud lock, first proposed by T.D.Hänsch and B.Couillard in 1980 [23]. A Brewster window is placed inside the cavity such that when linearly polarised light orientated at an angle that will produce both vertical and horizontal components will preferentially attenuate one polarization while leaving the other to freely propagate as shown in figure 5.7

The Brewster window acts to spoil the cavity Finesse for the attenuated component. On resonance these two components have the same phase but away from resonance the differing Finesse causes a phase difference between the two components. These two components are given by [41]

$$E_v = \left(\frac{1+i}{2}\right) \cdot \left(\frac{E_{inc-h}}{-1+g_{rt(h)}} + \frac{iE_{in-v}}{1-g_{rt}g_{rt(v)}}\right) t_1 t_2, \tag{5.5}$$

$$E_h = \left(\frac{1+i}{2}\right) \cdot \left(\frac{iE_{inc-h}}{1-g_{rt(h)}} + \frac{E_{in-v}}{-1+g_{rt}g_{rt(brew)}}\right) t_1 t_2, \tag{5.6}$$

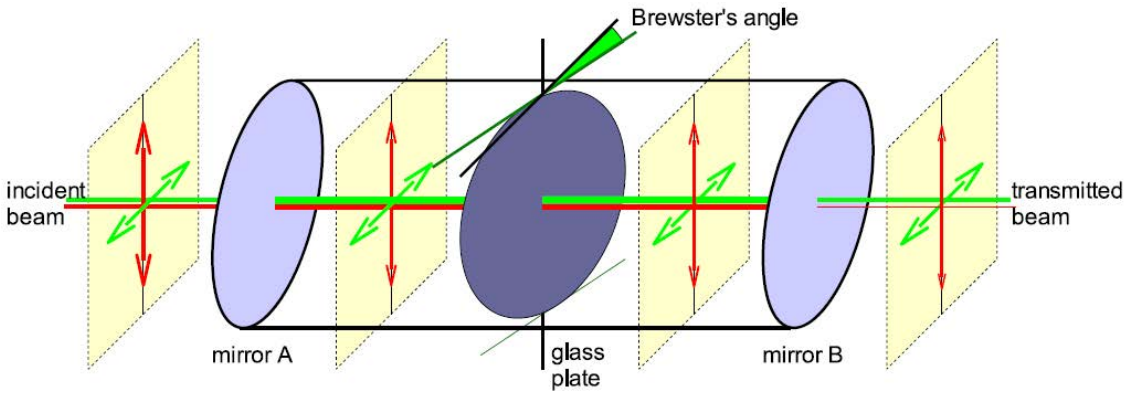

Figure 5.7: Transmission of two planes of polarization through the cavity. The Brewster's angle plate reduces the transmission for the vertically polarized component (red) while letting the horizontally polarized component (green) propagate freely [41].

where $g_{rt(v)}$ is the round trip gain factor for the vertical polarisation and $g_{rt(h)}$ is the round trip gain factor for the horizontal polarisation and $g_{rt(brew)}$ is the reduction of electric field amplitude caused by the Brewster window. Of course what we actually measure is the power of the beams incident on the photodiodes, which is proportional to $|E_{v/h}|^2$ and is given by

$$P_v = \left| \frac{E_{inc-h}}{-1 + g_{rt(h)}} + \frac{iE_{in-v}}{1 - g_{rt(v)}} \right|^2, \tag{5.7}$$

$$P_h = \left| \frac{iE_{inc-h}}{1 - g_{rt(h)}} + \frac{E_{in-v}}{-1 + g_{rt(v)}} \right|^2. \tag{5.8}$$

Taking the difference of these signals produces a dispersion shaped error signal which can be used to lock the cavity, figure 5.8.

5.3.2 Setup

The basic setup for this technique is shown in figure 5.9. Light from the laser firstly passes through a linear polariser, then enters the cavity with a Brewster window in the middle. The linearly polarised light is orientated 45° to the axis of the Brewster window to produce equal amounts of vertical and horizontal linearly polarised light from the Brewster window's perspective. The light transmitted through the cavity is sent to an analyser consisting of a quarter-wave plate and a polarising beam splitter(PBS). The PBS splits the two components which are sent to two different photodiodes. On resonance there is no phase shift between the

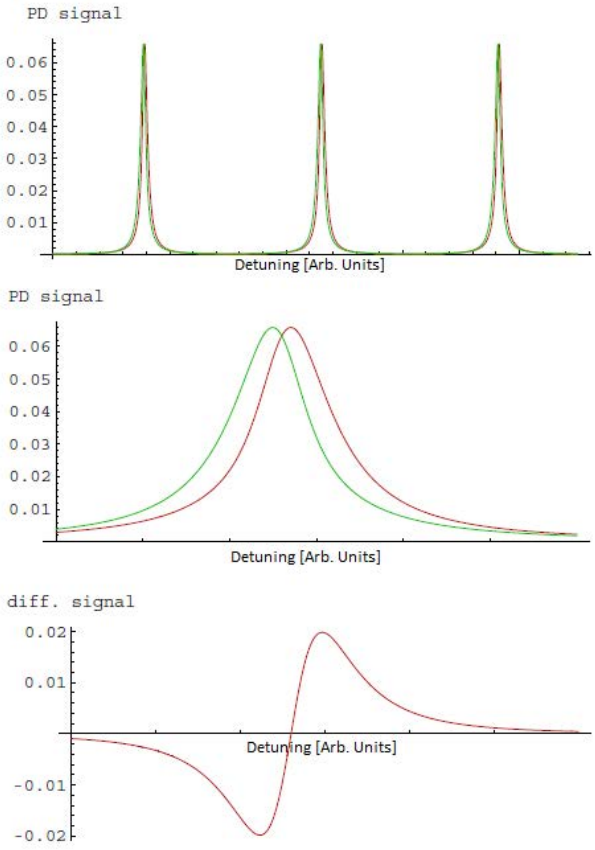

Figure 5.8: Photodiode signals relative to the incident intensity over laser wavelength (top), magnified for a single resonance (middle). Dispersion shaped difference signal for the same frequency range (bottom).

two linear components, therefore the polarisation of the light transmitted from the cavity will stay linear. We can consider this linear polarised light as the superposition of two counter-propagating circularly polarised components. As this light enters the analyser, the quarter wave plate transforms these circular components into orthogonal linearly polarised light which are separated by the beam splitter to be measured individually. As we move away from resonance there is a relative phase shift between the two linear components, therefore the polarisation of the transmitted beam becomes elliptical.

On resonance, the difference between the two signals is 0 since the split counter-propagating circularly polarized components have the same amplitude. Away from resonance, one component has greater amplitude than the other and this feature is reversed depending on which side of resonance is being observed. This leads to the dispersion shaped signal described above, figure 5.8. The zero crossing on resonance is used as the lock point. Though we are using this technique in transmission traditionally it is done in reflection.

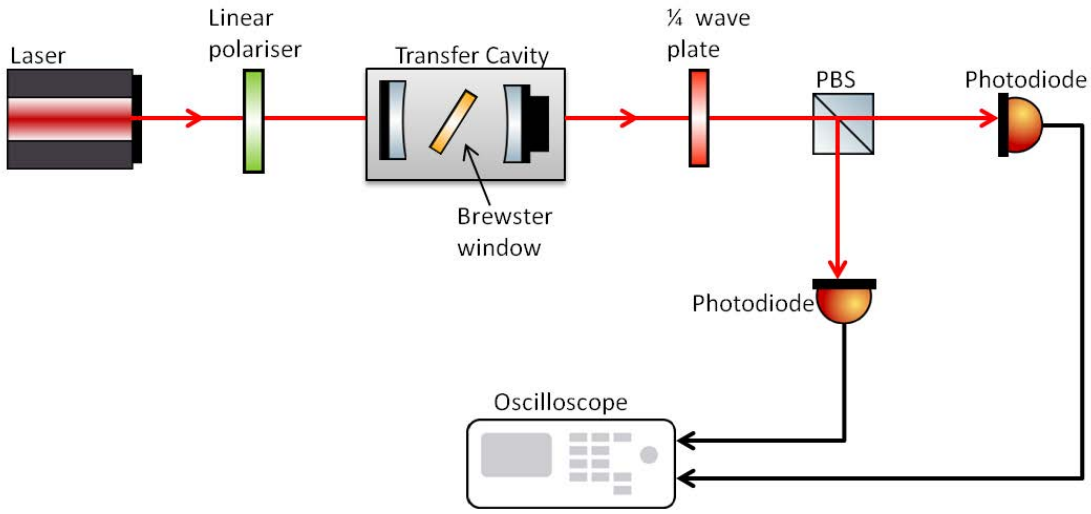

Figure 5.9: The experimental setup for Hänsch-Couillard, light from a laser is linearly polarised then sent a cavity a Brewster window in the middle. The output of the cavity is sent an analyser consisting a 1/4 wave plate and PBS.

However, we found that the amplitude of the light returning from the cavity is low compared to that of the directly reflected beam. This degrades the signal-to-noise ratio considerably, hence why we use transmission.

5.3.3 Results

With the Hänsch-Couillaud setup, the two orthogonal signals are observed on an oscilloscope. The difference between them is taken and produces an error signal. This was done for many Gouy degenerate positions and a select few are shown in figures 5.10, 5.11 and 5.12. A linewidth measurement was taken for the varying cavity lengths to observe how the Brewster window affected the overall linewidth of the cavity. As can be seen from figure 5.13 the overall trend of decreasing linewidth with cavity length is observed but at a much larger range, 9-38 MHz, compared to 4-10 MHz without a Brewster window. The Finesse of the cavity is also determined and found to be 66 ± 5. As can be seen from figures 5.10, 5.11 and 5.12, as we subdivide the FRS of the cavity the overall signal for each peak decrease by $\approx 1/N$.

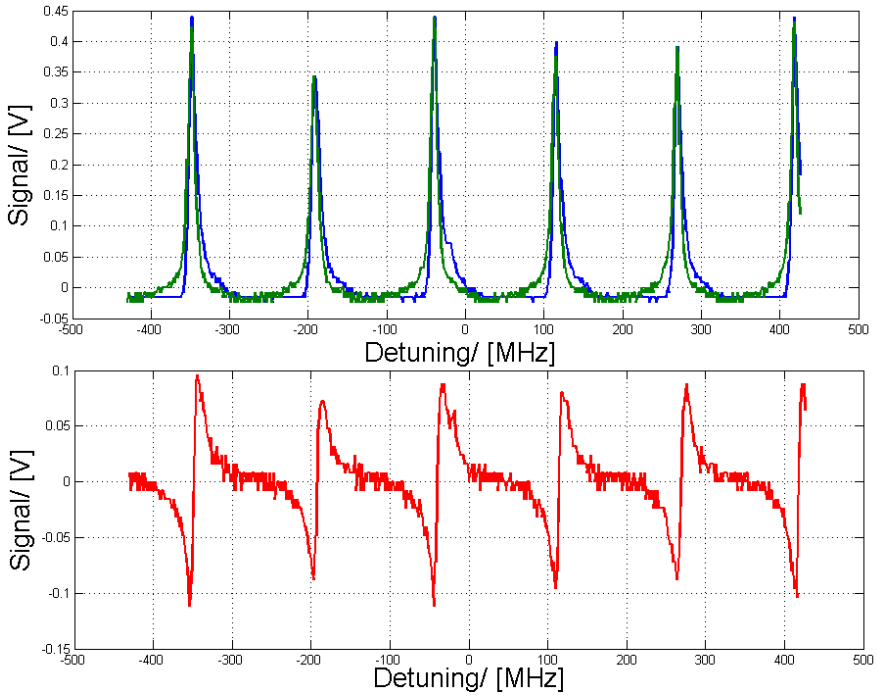

Figure 5.10: (Top) Transmission peaks of two planes of polarization through the cavity at a mode-spacing of 152 MHz. (Bottom) The error signal produced.

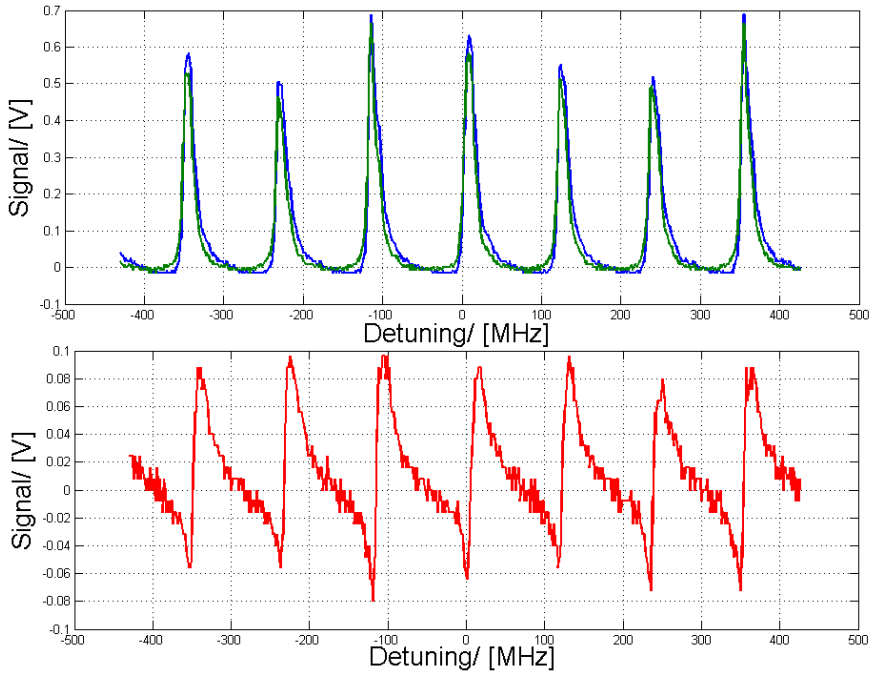

Figure 5.11: (Top) Transmission peaks of two planes of polarization through the cavity at a mode-spacing of 116 MHz. (Bottom) The error signal produced.

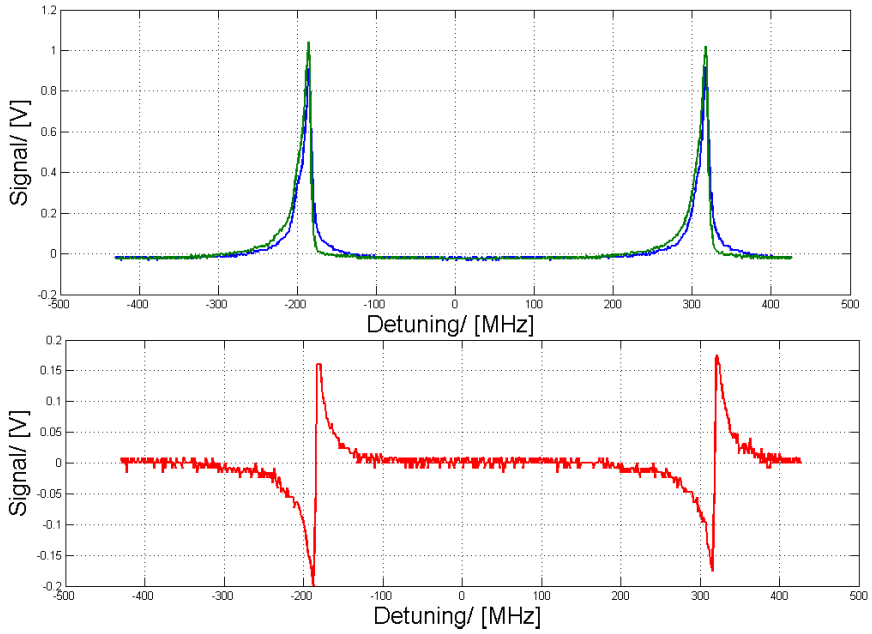

Figure 5.12: (Top) Transmission peaks of two planes of polarization through the cavity at a mode-spacing of 501 MHz (confocal). (Bottom) The error signal produced.

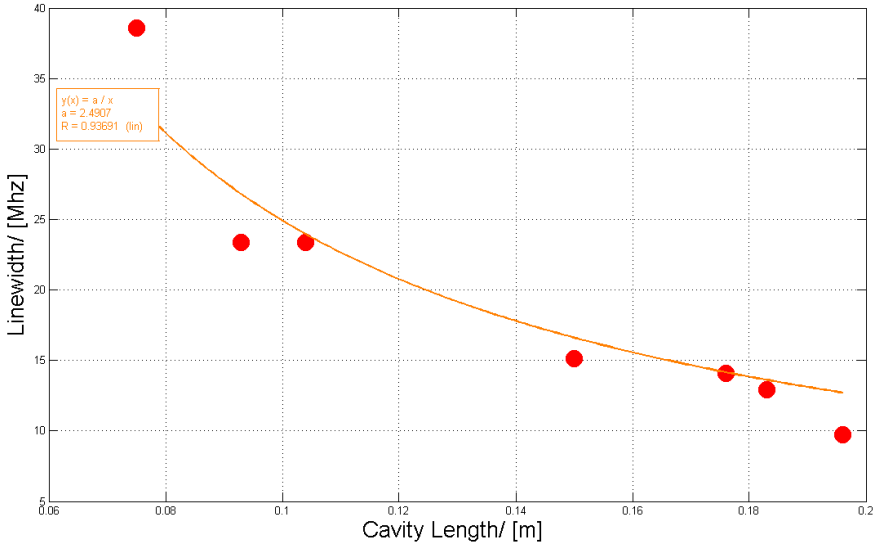

Figure 5.13: Linewidth of the cavity (with Brewster window) as a function of cavity length, a 1/x line fit is used to find an estimate of the Finesse, which was found to be 66 ± 5.

5.4 Pound Drever Hall locking scheme

The second method for locking the cavity to be discussed is a Pound Drever Hall (PDH) like technique. Built upon initial work by Pound with a microwave cavity [46], the technique was described by Drever and Hall in 1983 [18]. The basic principles of this technique are the same as Frequency Modulation (FM) spectroscopy. A laser beam is phase modulated and produces a frequency spectrum consisting of a carrier ω_c and two sidebands at $\omega_c \pm \omega_m$ whose electric field is given by

$$E_{inc} = E_0 e^{i(\omega_c t + \beta \sin \omega_m t)}, \tag{5.9}$$

and can be written in the form

$$E_{inc} = E_0 \left[J_0(\beta) e^{i\omega_c t} + J_1(\beta) e^{i(\omega_c + \omega_m)t} - J_1(\beta) e^{i(\omega_c - \omega_m)t} \right], \tag{5.10}$$

where β is the modulation depth. The transmitted beam is given by

$$E_{tran} = E_0[F(\omega_c) J_0(\beta) e^{i\omega_c t} + F(\omega_c + \omega_m) J_1(\beta) e^{i(\omega_c + \omega_m)t} - F(\omega_c - \omega_m) J_1(\beta) e^{i(\omega_c - \omega_m)t}], \tag{5.11}$$

where F is the transmission coefficient. This differs from traditional PDH as we are considering the transmitted beam and not the reflected. This has some different features, which will be discussed in section 5.4.2. The power of the beam measured on the photodiode is $P_{tran} \propto |E_{tran}|^2$ and after some algebra can be shown to have the form

$$\begin{aligned} P_{tran} = {} & P_c |F(\omega)|^2 + P_s \left| F(\omega_c + \omega_m) \right|^2 + \left| F(\omega_c - \omega_m) \right|^2 \\ & + 2\sqrt{P_c P_s}\, \Re[F(\omega_c) F^*(\omega_c + \omega_m) - F^*(\omega_c - \omega_m)] \cos \omega_m t \\ & + \Im[F(\omega_c) F^*(\omega_c + \omega_m) - F^*(\omega) F(\omega_c - \omega_m)] \sin \omega_m t \\ & + (2\omega_m \; terms). \end{aligned} \tag{5.12}$$

This signal from the photodiode is sent to a mixer which compares it to a Local Oscillator (LO) at the

modulation frequency ω_m. The sign of the mixer's output is different on either side of resonance and zero when the system is exactly on resonance.

When the modulation frequency ω_m is sufficiently high such that the carrier is on resonance with the cavity when the sidebands are not, the mixer and low pass filter will filter out everything in equation 5.12 but the term varying with $\sin(\omega_m t)$ and the error signal ϵ will be given by

$$\epsilon = 2\sqrt{P_c P_s} Im\left[F(\omega_c)F^*(\omega_c + \omega_m) - F^*(\omega_c)F(\omega_c - \omega_m)\right] \tag{5.13}$$

A plot of this error signal is shown in figure 5.14

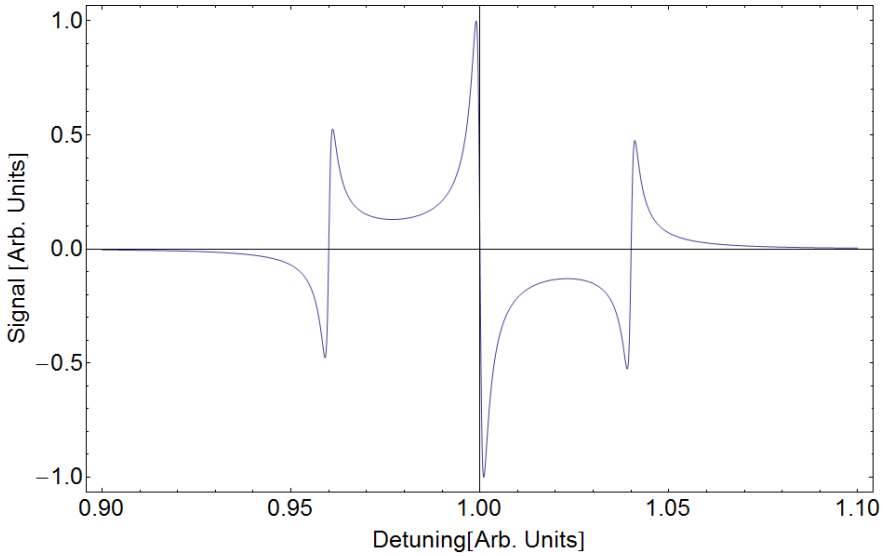

Figure 5.14: Error signal produced by the PDH technique.

5.4.1 Setup

The setup for this technique is shown in figure 5.15, the laser current is modulated using a four channel direct digital synthesis (DDS) evaluation board (analogue devices, AD9959/PCBZ-ND). The DDS allowed for relative adjustment of the phase between the LO and RF signal. This current modulation replaces the phase modulator described in section 5.4. This modulated light is incident on the cavity and some fraction is transmitted through and detected on a photodiode (Thorlabs DET100A/M). The photodiode signal is sent to a mixer (Mini-Circuits ZRPD-1) where is it mixed with a LO signal at the same frequency as the current modulation. The output of the mixer is low pass filtered with a home-built active low pass filter (fourth-order

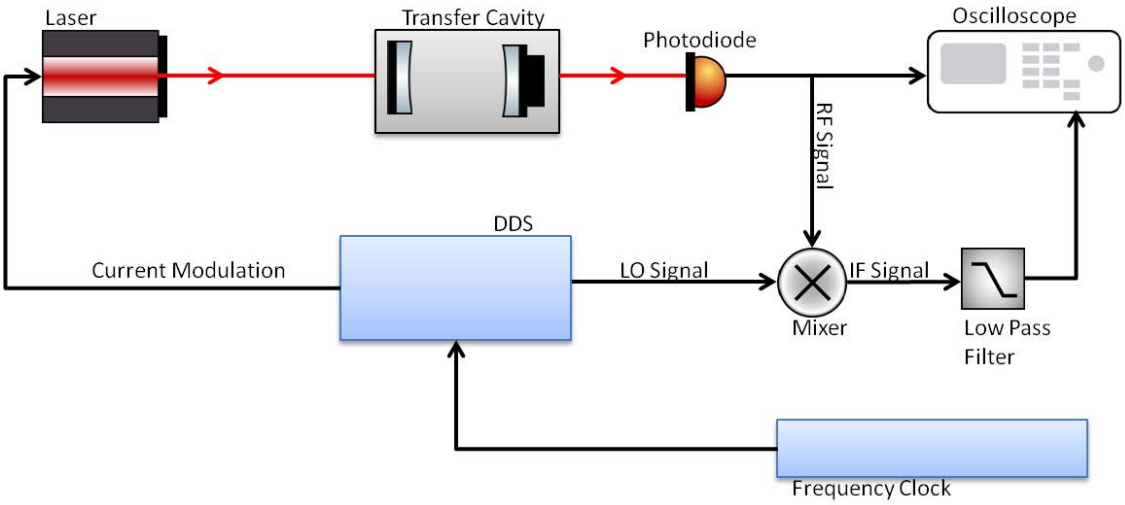

Figure 5.15: Setup of the PDH technique, the laser is current modulated at the modulation frequency ω_m producing phase modulated light which is sent through the cavity. The signal from the cavity is sent to a mixer where it is mixed with the LO and the output of the mixer is low-pass filtered and viewed on the oscilloscope.

Butterworth) with cutoff frequency 200 kHz. The error signal is observed on an oscilloscope. Results were taken from one Guoy degenerate position with a mode spacing of 42 MHz and the modulation frequency ω_m was varied from 21-39 MHz.

Scanning the modulation frequency down from 39 MHz to 21 MHz, at the higher end of the modulation frequency the sidebands begin to overlap with the adjacent carrier and the error signal observed is a convolution of the three peaks, this is evident is the error signals (figure 5.17). As we lower the modulation frequency, the sidebands do not overlap with adjacent carriers anymore and the error signals resemble (figure 5.17). Interestingly when the modulation frequency is lowered still, at exactly half the mode spacing i.e $\omega_m = 21$ MHz, the sidebands overlap and produce error signals identical to that of the carrier (figure 5.18). This feature of the system gives us an extra factor of 2 in mode spacing without the equal loss in signal strength. In this case it means that instead of having lock points every 42 MHz for this configuration, effectively there are lock points every 21 MHz. A manageable amount of detuning which can be achieved using an AOM.

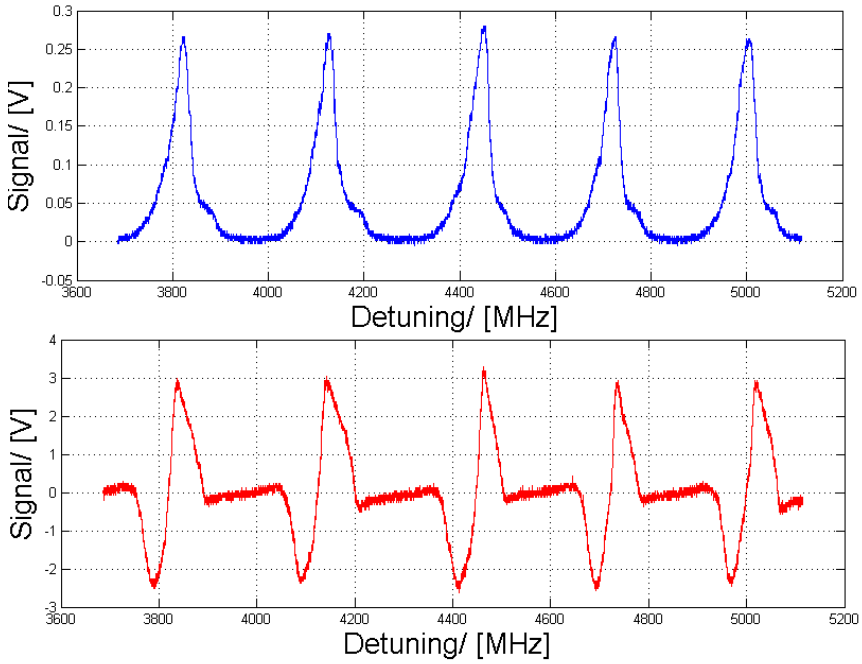

Figure 5.16: (Top) Transmission peaks of the PDH signal through the cavity with mode spacing of 42 MHz at a modulation frequency of 35 MHz. (Bottom) The error signal produced.

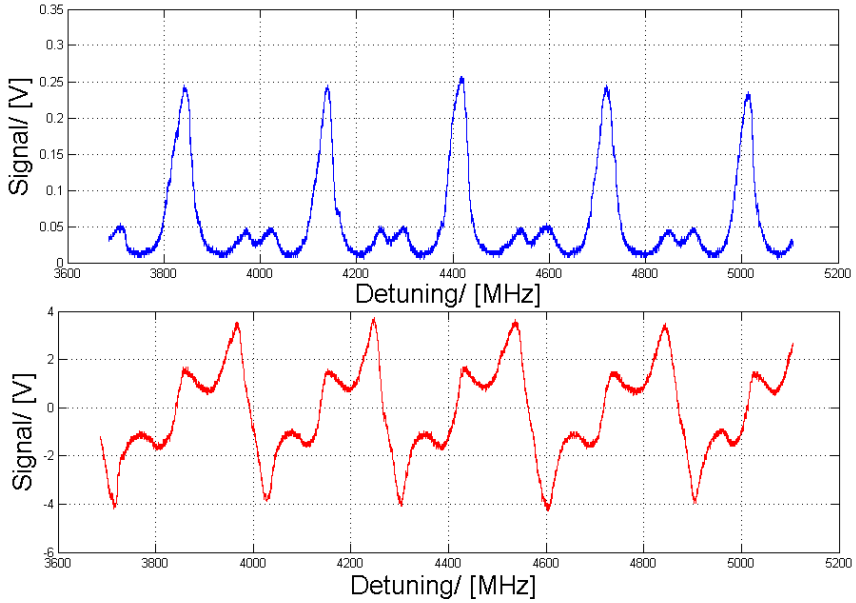

Figure 5.17: (Top) Transmission peaks of the PDH signal through the cavity with mode spacing of 42 MHz at a modulation frequency of 25 MHz. (Bottom) The error signal produced.

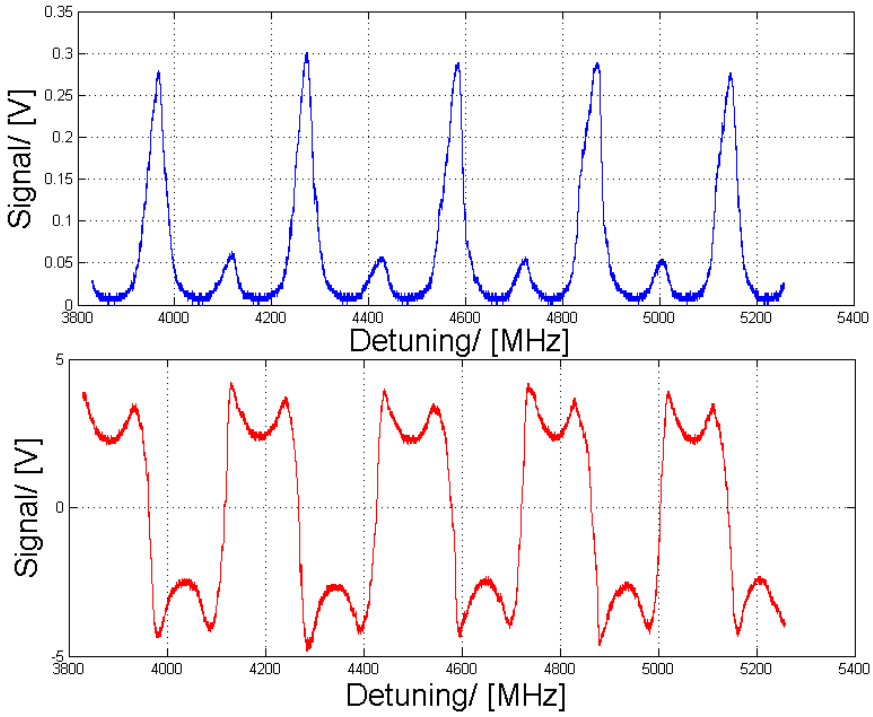

Figure 5.18: (Top) Transmission peaks of the PDH signal through the cavity with mode spacing of 42 MHz at a modulation frequency of 21 MHz. (Bottom) The error signal produced.

5.4.2 Transmission PDH vs Reflection PDH

As mentioned earlier, a PDH like signal done in transmission is used in this experiment instead of traditional reflection PDH and the reasons for which are presented in this section. When PDH is done in reflection, when the carrier is resonant with the cavity the sidebands are not and thus are reflected from mirror surface. At resonance the carrier beam is actually the coherent sum of two beams, namely, the directly reflected beam and the leakage beam from the circulating field inside the cavity. These two beams are of equal amplitude and out of phase by 180 degrees. They thus destructively interfere and the total intensity of the reflected beam vanishes. Away from resonance, this condition is broken and the beams no longer cancel and the reflected signal has some amplitude. The phase of this light tells you which side of resonance a laser is on. This is measured by beating the carrier with the sidebands as described above.

This situation usually assumes a cavity at confocal with (near)perfect mode matching. However, when using the Gouy degenerate method outlined earlier, on a particular resonance, most of the carrier light is not resonant with the cavity. Only light on that specific resonant set of degenerate modes, the rest are reflected.

This adds an increasingly large background signal which offsets the reflected carrier and increases the signal to noise ratio as you subdivide the resonance peaks. This is not ideal and thus we run a PDH like signal in transmission to circumvent this problem, in this case only the signal of interest is transmitted and does not sit on a background.

One drawback of running transmission PDH is the fact that the response of the system is limited by the storage time of the cavity. In reflection PDH as stated earlier, the carrier is a superposition of two beams, the directly reflected and the leakage beam. The directly reflected beam contains the instantaneous phase information of the laser and any phase deviations of the laser immediately change the amplitude of the carrier and are registered by the error signal. In transmission PDH the carrier and sidebands however have to enter and exit the cavity before any measurements of the phase deviations of the lasers can be done. The decay time τ_c of a cavity can be estimated with the expression

$$\tau_c = \frac{1}{2\pi\Delta\omega}, \tag{5.14}$$

where $\Delta\omega$ is the linewidth of the cavity. For our cavity we have a linewidth of 5.13 MHz, which leads to decay time of 31 nanoseconds. This timescale is unlikely to have a drastic effect on the response time of our error signal. It should be noted that if one is interested in using a high finesse cavity with this setup i.e with a narrow linewidth. It will be at the cost of response time of the error signal, for example, for a 5 kHz cavity one can expect a delay of 3 microseconds.

5.5 Discussion

Overall both methods work well at providing good quality error signals. The HC method has the advantage of being simple and does not require radio frequency components and modulators, but suffers from having the Brewster window degrade the Finesse of the cavity. This can be compensated by starting with a cavity of a much higher finesse than needed and/or using a better quality Brewster window. The PDH like method also provides good quality error signals but requires RF components. Ultimately we chose to use the PDH like technique for our experiment, mostly because the HC method required a repositioning of the Brewster window and realignment of the cavity every time the length of the cavity changed. Since one of the most desirable aspects of the Gouy degenerate cavity is the versatility to scan the cavity length to chose a convenient mode spacing this would be severely hampered by the alignment problem of HC.

CHAPTER 6

THE RING CAVITY

This chapter details the design and construction of the ring cavity used in the experiment. The ring cavity is atypical in its design as it has three mirrors in a triangular configuration as opposed to the more common two-mirror linear cavity. This design means that the ring cavity can support two propagation modes in opposite directions. If one injects both propagation modes, the resultant standing wave mode can be translated by changing the phase of one of the input beams. Care is taken in the design of the cavity to get the desired values of g, γ and κ to allow the system to reach the strong coupling regime.

6.1 Design and Fabrication

The main challenge involved in the design of the ring cavity is the incorporation of external laser beams that form an intra-cavity MOT in the middle of the cavity mode. A schematic of the MOT beams and cavity mode is shown in figure 6.1. From this, we can see that in order for the cavity mirrors to not impede the MOT beams, they must be placed in three corners of the square intersection of the MOT beams forming a right angled isosceles triangle. The cavity itself is formed from one curved mirror and two flat mirrors. The flat mirrors act as input and output couplers for the cavity light while the curved mirror has a piezo attached at the back for scanning of the cavity length.

Figure 6.2 shows 3D CAD images of the cavity. Circular holes are carved out of the frame for MOT beam access and the end faces have 0.5 mm deep grooves for holding 6 mm mirrors. The middle groove holds the piezo and curved mirror. The overall height of the cavity is 5.4 cm to allow the MOT and cavity beams to coincide with the centers of the vacuum windows.

One of the main features of the ring cavity, the ability to have two propagation modes is illustrated in figure 6.3. The input and output channels for the modes are shown and depending on the experiment it is

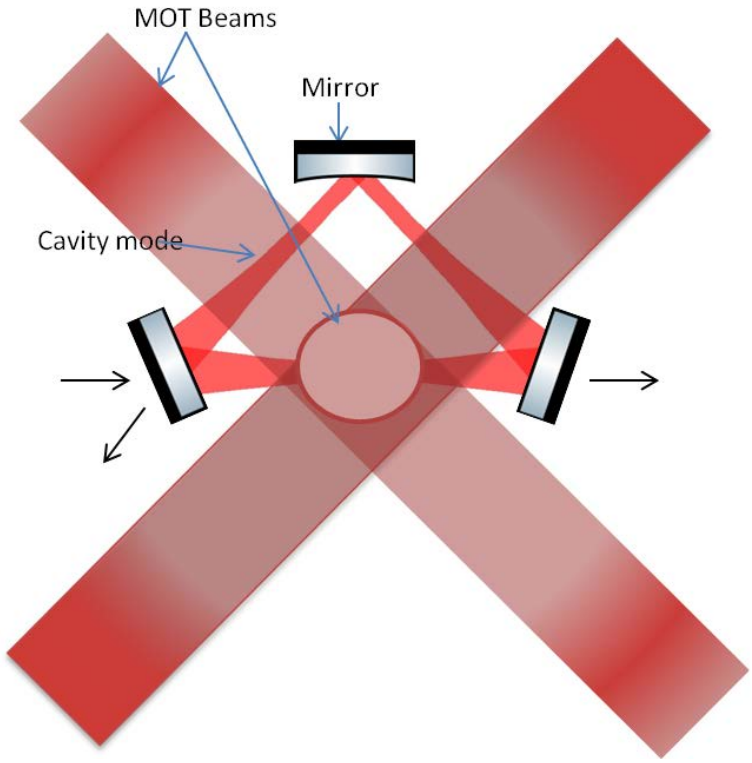

Figure 6.1: Mirror positions of the cavity in relation to the MOT beams.

possible to use one mirror as a input/output coupler or have one mirror as a input/input and the other flat mirror as a output/output coupler.

The mirrors used are 6 mm diameter and 4 mm thick, with dielectric coatings from Layertec. The geometry of the cavity means that the incoupled light is incident on the mirrors at different angles (45 for the curved mirror and 22.5 for the flat mirrors) and since dielectic coatings are angle dependent this will result in differing reflectivities for the mirror sets for one particular coating. The coating is designed for linear s-polarisation and is optimised to cover both 767 nm and 852 nm as shown in figure 6.7. The coating has slightly higher reflectivity for 45 degree angle which corresponds to the curved mirror, which results in improved impedance matching (detailed in the following section).

The cavity was machined inhouse by the Physics department machine shop. The material used was 316 stainless steel as this is the same steel as the vacuum chamber, which helps to avoid differential thermal stresses during baking of the chamber. 316 steel has a low magnetic permeability to make the cavity insensitive to the magnetic field used to generate the MOT. Also it would not get magnetised itself. The cavity has a monolithic design with no degrees of freedom. This was chosen as there was limited space to add any mechanical actuators

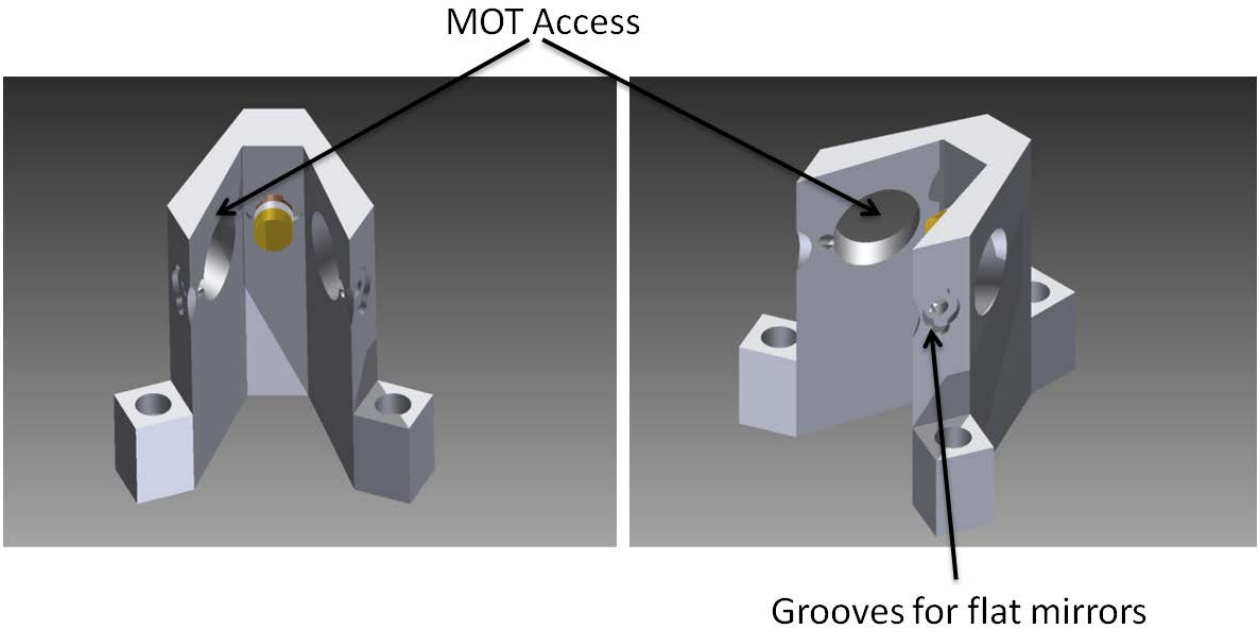

Figure 6.2: 3D CAD model of the ring cavity showing MOT beam access.

to the design and more discrete actuation, for example notch hinges were simply unfeasible for the size of the cavity. Though we lose the versatility of actuation we gain the stability of having a monolithic design as shown in figure 6.4.

After machining, the cavity is cleaned using the cleaning procedure outlined in chapter 7. Once clean the mirrors are glued to the frame using Epotec H-74 epoxy from Epoxy Technology. This glue was chosen for its low outgassing rate, being certified by NASA and for its broad working temperature range of -20 to 300 degrees. The glue is heat cured in a portable oven at 120 degrees for 30 minutes as shown in figure 6.5. For the curved mirror, a ceramic spacer is glued onto the cavity frame before the mirror is glued onto the piezo to prevent electrical contact between the piezo and the cavity frame.

6.2 Mode Volume and Astigmatism

As shown in the previous chapter, one of the factors that that determines the value of g is the mode volume, V, which is given by

$$V = \frac{\pi \omega_t \omega_s p}{2}, \tag{6.1}$$

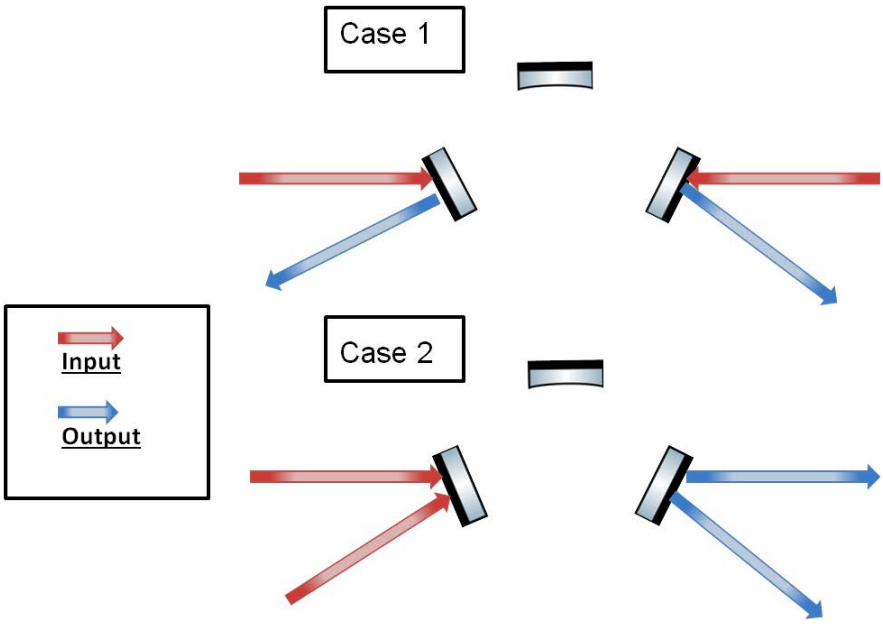

Figure 6.3: Input/Output channels for the cavity.

where p is the round trip length of the cavity, ω_t and ω_s represent the mode waists of the cavity. Normally, as in the case of a two-mirror cavity there is only one value for the mode waist, however in a ring cavity the off-axis reflection of the beam from the curved mirror introduces astigmatism [40]. This results in light rays in the sagittal and tangential plane encountering a different geometry to each other at the mirror surface as shown in figure 6.6.

For an off-axis reflection at an angle, θ, the effective focal lengths for the two planes are given by

$$\text{Tangential focal length} = \frac{R\cos\theta}{2}, \tag{6.2}$$

$$\text{Sagittal focal length} = \frac{R}{2\cos\theta}. \tag{6.3}$$

These have corresponding ABCD matrices given by

$$M_T = \begin{pmatrix} 1 & 0 \\ \frac{-2}{R\cos\theta} & 1 \end{pmatrix} \text{ and } M_S = \begin{pmatrix} 1 & 0 \\ \frac{-2\cos\theta}{R} & 1 \end{pmatrix},$$

where R is the radius of curvature of the mirror and θ is the angle of incidence.

Using the complex beam parameter, q, and the ABCD formalisation, it is possible to calculate the values

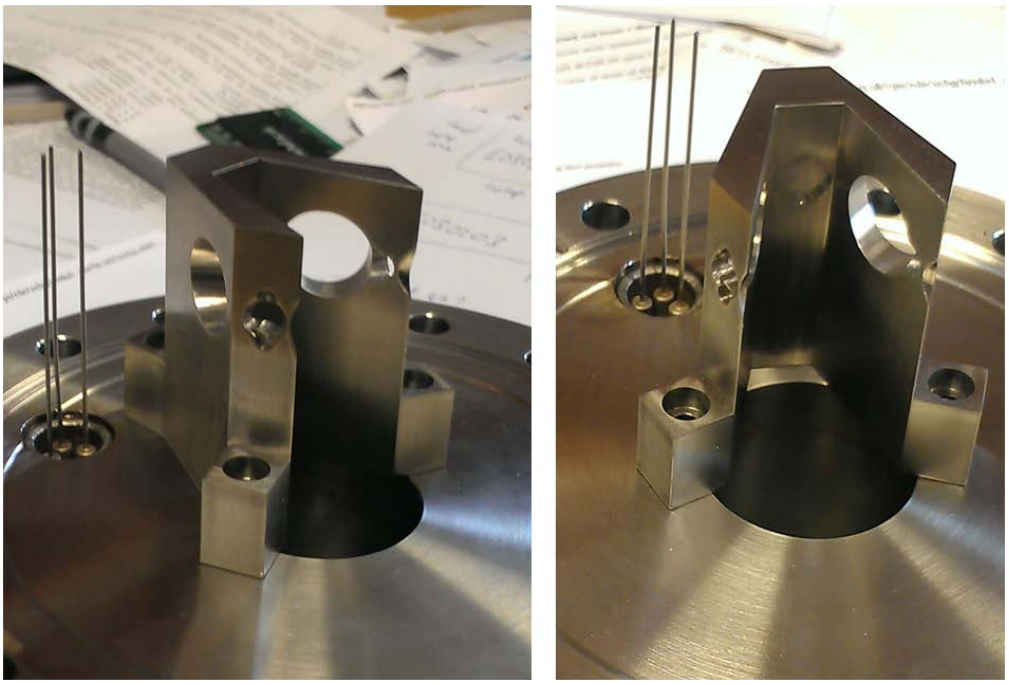

Figure 6.4: Cavity frame after machining.

of ω_T and ω_S. By taking the expression for the q parameter given by

$$\frac{1}{q} = \frac{D-A}{2B} \pm \frac{1}{2B}\sqrt{(A-D)^2 + 4BC} \tag{6.4}$$

and using the fact that at the mode waist $A = D$, this reduces to

$$q = \sqrt{|\frac{B}{C}|}. \tag{6.5}$$

Using the expression for q which is in terms of wavefront radius of curvature and wavelength, given by

$$\frac{1}{q(z)} = \frac{1}{R(z)} - i\frac{\lambda}{n\pi\omega(z)^2} \tag{6.6}$$

and taking the fact that $R(z) \to \infty$ at the mode waist, we get an expression for the mode waists, $\omega_{(T,S)}$ given by

$$\omega_{(T,S)} = \sqrt{\frac{\lambda}{\pi}\sqrt{\frac{B}{C}}}. \tag{6.7}$$

To calculate the values of B and C the ABCD matrix for the cavity is evaluated by taking the q parameter

Figure 6.5: Cavity mirror gluing and heat curing procedure in portable oven.

from the mode waist and traversing one round trip. This is done twice to calculate values for ω_T and ω_S and is given by

Tangential round trip matrix =

$$\begin{pmatrix} 1 & d \\ 0 & 1 \end{pmatrix} \begin{pmatrix} 1 & 0 \\ \frac{-2}{R\cos\theta} & 1 \end{pmatrix} \begin{pmatrix} 1 & d \\ 0 & 1 \end{pmatrix}$$

Sagittal round trip matrix =

$$\begin{pmatrix} 1 & d \\ 0 & 1 \end{pmatrix} \begin{pmatrix} 1 & 0 \\ \frac{-2\cos\theta}{R} & 1 \end{pmatrix} \begin{pmatrix} 1 & d \\ 0 & 1 \end{pmatrix},$$

where d is the distance from the mode waist to the curved mirror. After evaluating the matrices for d, R and θ values of 3.41 cm, 10 cm and 22.5° respectively we find that $\omega_T = 92.86\ \mu m$ and $\omega_S = 121.53\ \mu m$. From this it can be seen that the mode waist does not form a circle but rather has an elliptical shape. Substituting these values into equation 6.1 for the mode volume gives a value of 1.21 mm^3.

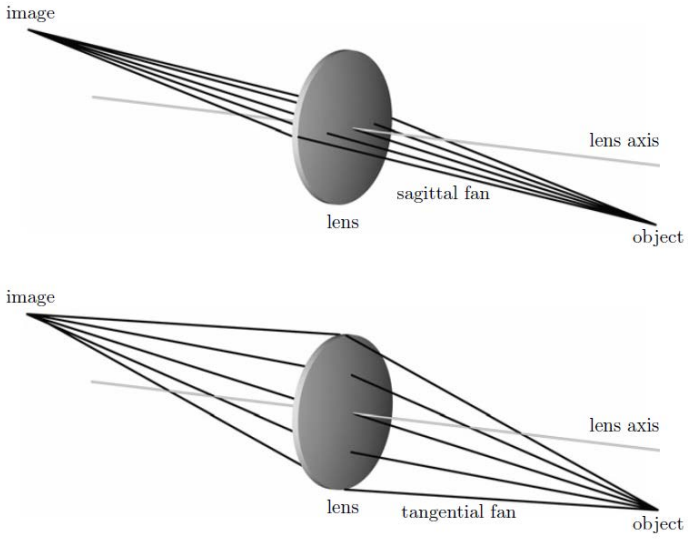

Figure 6.6: Astigmatism abberation in which sagittal and tangential rays become non-degenerate [40].

6.3 Finesse and Linewidth

The finesse and linewidth of the cavity are mostly determined by the reflectivities of the mirrors. Since the cavity will host two sets of light, the probing light at 767 nm and the trapping potential at 852 nm it is important that both sets of wavelength are characterised for their finesse and linewidth. A graph of the mirror reflectivities is shown in figure 6.7. The reflectivity of dielectric mirrors is dependent on the angle at which the light strikes the mirror. For our triangular cavity light is incident on the curved mirror at 45° and at the two flat mirrors at 22.5°. If we represent the reflectivities of the cavity mirrors as

$$\begin{aligned} \text{Curved Mirror} &= R_1 \\ \text{Flat Mirror} &= R_2 \end{aligned}$$

from the graph in figure 6.7 for 767 nm light $R_1 = 99.96\%$ and $R_2 = 99.86\%$ and for 852 nm light $R_1 = 99.95\%$ and $R_2 = 99.87\%$. From here we can use the equation for the linewidth introduced in chapter 4 in the form

$$HWHM = \frac{1}{2}\frac{2c}{\sqrt{m}L\pi} \tag{6.8}$$

and taking into account that $R_{1,2} = r_{1,2}^2$[1] we get m that is given by

$$m = \frac{4\sqrt{R_1}\sqrt{R_2^2}}{1-\sqrt{R_1}\sqrt{R_2^2}}. \tag{6.9}$$

[1] $R_{1,2}$ as defined here is the power reflectivity of the mirror, the $r_{1,2}$ used to define these equations is the amplitude reflectivity

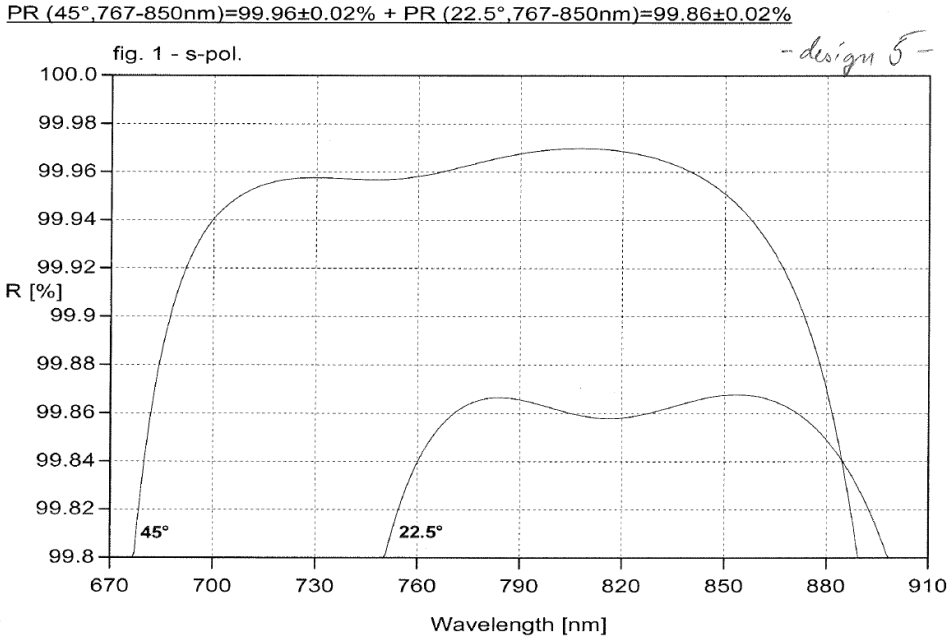

Figure 6.7: Data from the manufacturer showing the reflectivities of s-pol light on the dielectric ring cavity mirrors at 45° and 22.5° incident angle over desired wavelength range.

From this we get a HWHM linewidth of the cavity also known as κ for the two wavelengths as

$$\begin{aligned} \kappa_{767nm} &= 2\pi \times 1.18 \text{ MHz} \\ \kappa_{852nm} &= 2\pi \times 1.08 \text{ MHz} \end{aligned}$$

The Finesse of the cavity, which as described in chapter 4 relates to the cavity's ability to store light after successive round trips and is given by

$$F = \frac{\pi}{2}\sqrt{m}. \tag{6.10}$$

For the two sets of light, we get Finesse values of

$$\begin{aligned} F_{767nm} &= 1962 \\ F_{852nm} &= 2025. \end{aligned}$$

The Free Spectral Range (FSR) of the cavity is the same for both wavelengths as it only depends on the length of the cavity and is given by

$$FSR = \frac{c}{p}. \tag{6.11}$$

For our cavity length of 6.82 cm we get a FSR of 4.4 GHz. This sets the lower limit on the scan range that the piezo must perform in order to observe a cavity fringe.

6.4 Impedance matching and mode matching

To maximise the amount of light coupled to the cavity, it is important to make sure the cavity is impedance and mode matched. Impedance matching in this case is similar to that of electric networks theory, which states that a generator delivers maximum power to a load when the source impedance is equal to the load impedance [21]. In optics this rule is also true, although in this context impedance is a figure of speech and has no units. For an optical cavity, maximal light is coupled into the cavity when the round trip power loss is equal to the transmission of the input mirror. If we define a parameter, r_m, as the fraction of the remaining cavity field after one trip (excluding the transmission through the input mirror), the input mirror as r_1 and the other mirrors as r_2 and r_3, then the cavity is impedance matched when $r_m = r_1$. Assuming no absorptive or scattering losses $r_m = r_2 r_3$.

To measure how well a cavity is impedance matched, it is useful to introduce a mismatch parameter, σ, which quantifies how far from the ideal impedance matched condition a system is in and is given by

$$\sigma = \frac{1 - r_1}{1 - r_m}. \tag{6.12}$$

With this parameter it is possible to estimate the coupling ratio of the incoupled intensity, I_c, to the incoupled intensity at perfect impendance matching, $I_{c,matched}$ using the expression,

$$\frac{I_c}{I_{c,matched}} = \frac{4\sigma}{(\sigma + 1)^2}. \tag{6.13}$$

The following table lists all the mirror parameters for calculating the coupling ratio for the ring cavity at both 767 nm and 852 nm

	r_1	r_2	r_3	r_m	$\frac{I_c}{I_{c,matched}}$
767nm	$\sqrt{0.9986}$	$\sqrt{0.9996}$	$\sqrt{0.9986}$	$\sqrt{0.998256}$	0.984
852nm	$\sqrt{0.9987}$	$\sqrt{0.9995}$	$\sqrt{0.9987}$	$\sqrt{0.998265}$	0.974

From this we can see that there is a theoretical maximal impedance matching of over 97% and there is negligible difference in impedance matching for the mirror coatings of the two different wavelengths. This theoretical maximum was achieved by designing the mirror coatings such that the input and output coupling mirrors (r_1 and r_3) have a lower reflectivity than the curved central mirror (r_2), which in this context served to preserve the amplitude of the circulating field by allowing very minimal transmission through it. A maximum impedance matching of 100% can be achieved by setting r_1 as the input and output coupler and having r_2

and r_3 have a reflectivity which tends to 1 (i.e 0.99999...). Conversely if we used stock mirrors with the same reflectivity for all 3 mirrors, for this system it would yield a maximum impedance matching of 88%.

Mode matching refers to the shaping of the incoming beam's mode profile to match that of the resonant mode of the cavity. As shown in chapter 5, it is possible to excite multiple modes in a confocal 2-mirror cavity and have these modes be degenerate to one another. For a ring cavity this is not possible and any mode coupled into a cavity of this type will have distinct resonant modes.

Therefore in order to have maximal light coupled into the cavity it is essential that mode profile of the incoming beam match the propagation mode of the cavity. This is done by using a set of lenses to shape the waist and divergence of the beam to match the waist and divergence of the cavity mode. The complex beam parameter, q, can be used to specify the properties of a Gaussian beam at any point in its propagation, therefore by mapping the complex beam parameter of the incoming laser beam with that of the cavity mode, mode matching can be achieved.

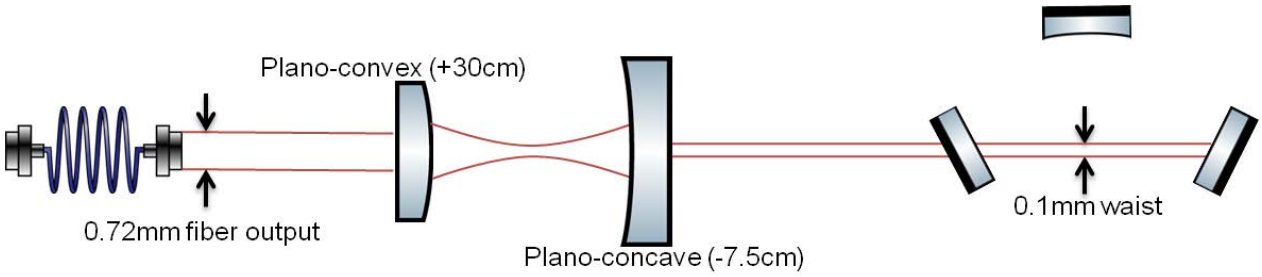

Figure 6.8: Aberration balancing mode matching system.

Figure 6.8 shows a drawing of the lens system to be used for mode matching. Two lenses form a telescope whose focal waist is made coincident with that of the cavity mode. The beam exits a Schafter + Kirchhoff (60FC-4-A4-02) fiber output coupler with a diameter of 0.72 mm. The lens systems comprises of a 30 cm and -7.5 cm lens which form a 4× demagnification telescope making a spot of 0.1 mm which corresponds to the calculated mode waist of the cavity.

To reduce the amount of aberrations in the system, we employed a method of aberration balancing which involved matching the aberration coefficients of the lenses used to minimise the overall contribution to spherical aberrations of the system [13]. Figure 6.9 shows the aberration coefficients of several lenses. The total spherical aberrations of a two lens system can be calculated using the Longitudinal Spherical Aberration (LSA) equation [13]

$$LSA = \frac{k_1 f_1}{(f/\#)^2} + \frac{k_2 f_2}{(f/\#)^2}, \tag{6.14}$$

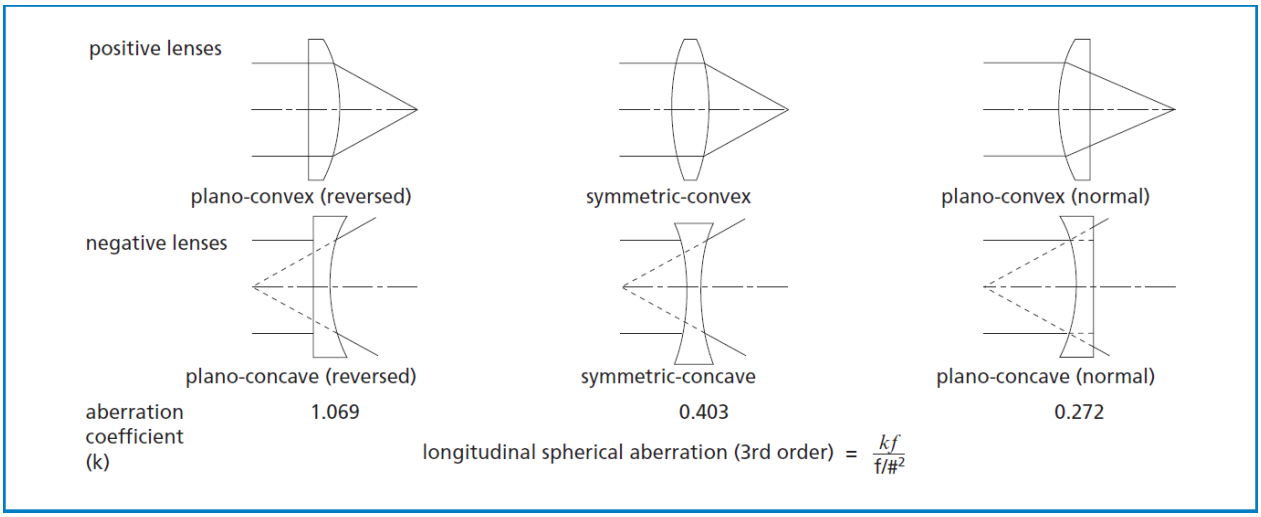

Figure 6.9: Aberration coefficients for typical lens shapes [13].

where $f_{1,2}$ is focal length, $f/\#$ is the f-number and k is the aberration coefficient. After setting the equation to 0, we get the expression

$$\frac{f_1}{f_2} = \frac{k_1}{k_2}. \tag{6.15}$$

The ratio k_1/k_2 sets the magnification level for a given lens system. For our system we require a demagnification of ≈ 4 so by choosing a positive plano-convex and a negative plano-concave with focal lengths +30 cm and -7.5 cm respectively and aberration coefficients 1.069 and 0.272 respectively, the condition in equation 6.15 is satisfied and spherical aberrations are minimised.

6.5 Cavity Stability

As shown in chapter 4, only certain mirror geometries can support a cavity. The stability criterion equation is used to determine if a stable cavity can be formed according to

$$|A + D| \leq 2, \tag{6.16}$$

where A and D are values from the round trip ABCD matrix of the cavity. As shown previously, ring cavities have two round trip ABCD matrices and both must satisfy the stability criterion. The evaluated forms of the ABCD matrices have the form

Tangential round trip matrix =

$$\begin{pmatrix} 0.0343 & 0.0353 \\ -28.2843 & 0.0343 \end{pmatrix}$$

Sagittal round trip matrix =

$$\begin{pmatrix} 0.5172 & 0.0518 \\ -14.1421 & 0.5172 \end{pmatrix}$$

From this we get a tangential $A + D$ value of 0.0686 and sagittal $A + D$ value of 1.0344 which both satisfy the stability criterion.

6.6 Cavity Alignment

As the cavity has a monolithic design, special care had to be taken in the alignment of the beam onto the cavity mode. The alignment procedure was done in two stages, firstly on the optical table in free air and then repeated when the cavity was under vacuum is the experimental chamber. For the first stage the degrees of freedom used for alignment were the angle and position of the incoming beam and the position of the central curved mirror relative to the two flat mirror. The position of the curved mirror is moved to compensate for any tilts away from normal of the mirrors or the physical body of the frame itself. These tilts would manifest as planar deviations of the cavity mode axis as illustrated in figure 6.10. A tilt on the mirrors causes the beam to incident on the curved mirror away from its center of curvature resulting in the beam being deflected at some angle away from normal causing the beam to walk. By moving the curved mirror up and down, moving the beam plane up and down or a combination of both it is possible to find the new center of the curvature for the system where the beam can undergo multiple round trips without the beam walking.

With a new center of curvature found the incoming beam is aligned onto the input coupler with two high-precision mirror mounts. A white card placed on the output coupler viewed through an infrared camera is used to view the spots of the transmitted beams. With better alignment more spots appear and eventually converge into one, as shown in figure 6.11. With the alignment set the mirrors are glued and cured. Once the cavity is inside the vacuum chamber the same procedure for alignment is done minus the mirror translation degree of freedom. As well as observing the spots on the output of the cavity, by turning the dispensers on and tuning the incoming light to be resonant with the atoms, it is possible to make the beam inside the cavity visible by the fluorescence of the atoms it intersects, as shown in figure 6.12. This allows for careful tuning of the incoming beam angle and position until all the beam paths overlap and resonance is achieved.

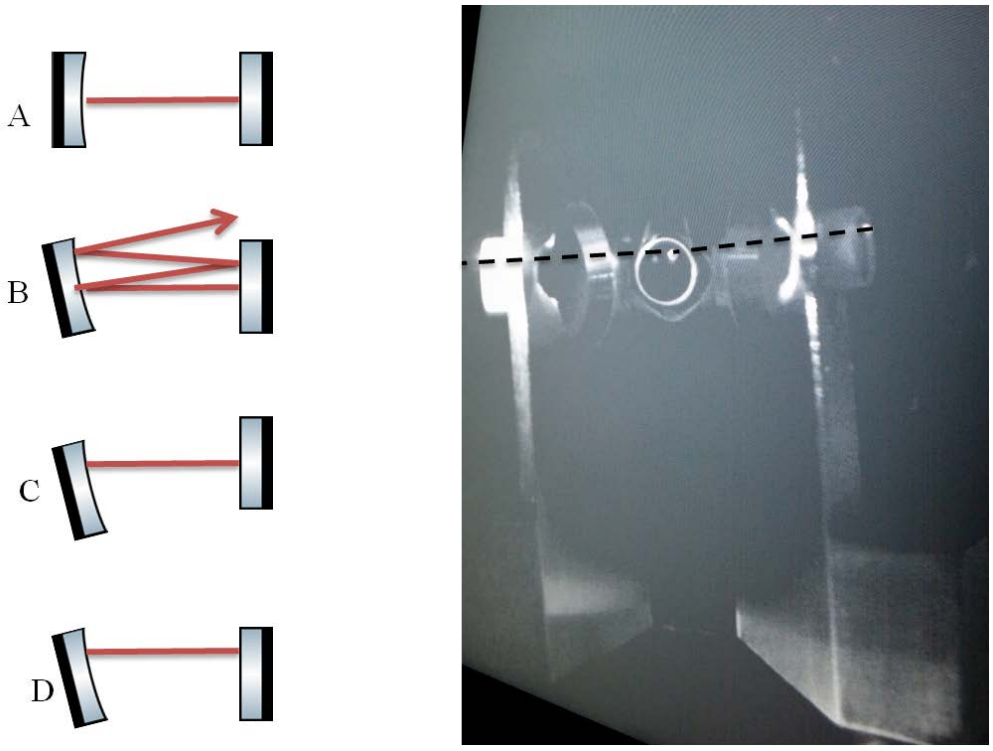

Figure 6.10: Left: (A), beam plane and mirror positions for ideal case with no misalignment. (B) Tilt of the curved mirrors causes the beam path to become unstable and the beam walks. (C) Translation of the curved mirror to find new stable center of curvature for the cavity axis. (D), Cavity axis is translated to match the new center of curvature of the tilted mirror where the mode is stable. Right: New cavity axis for the ring cavity to compensate for deviations from planarity in our system.

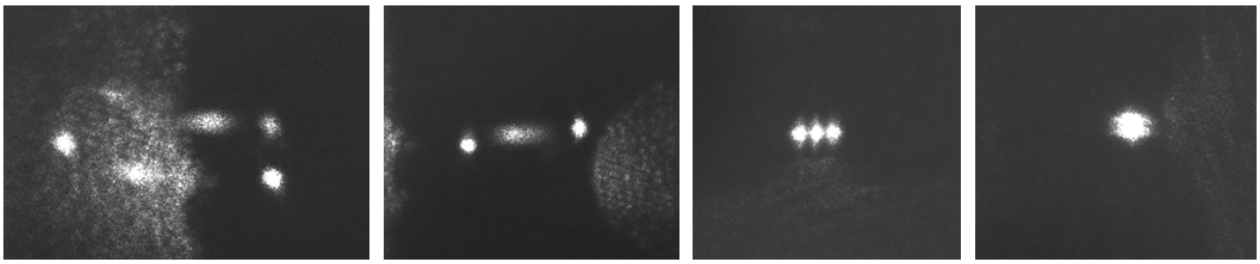

Figure 6.11: From Left to Right: Multiple passes through the cavity eventually converge to form one stable cavity mode.

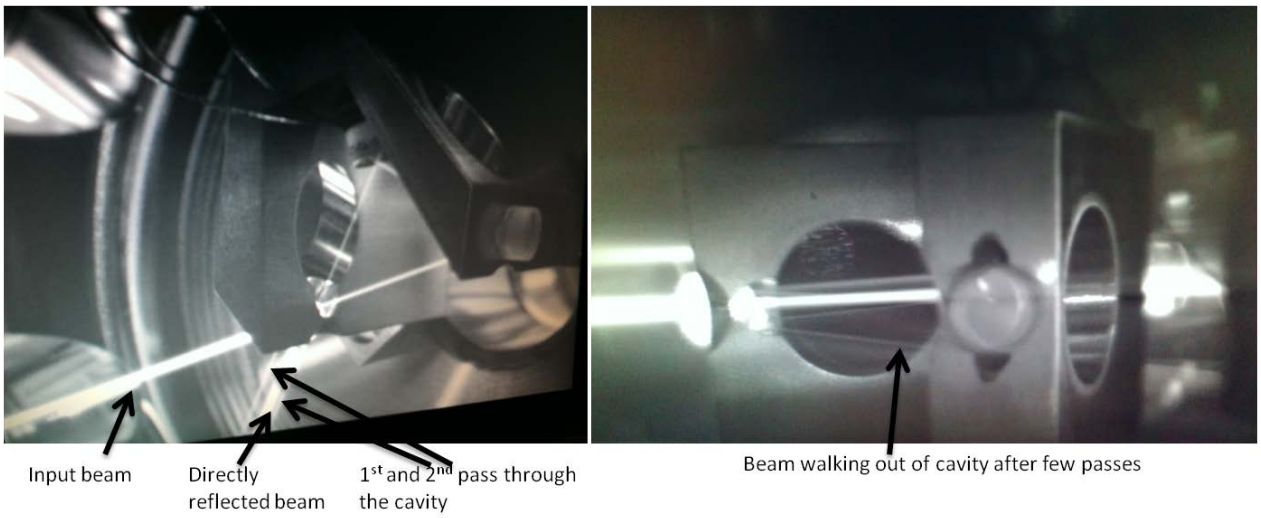

Figure 6.12: Using the fluorescence of the atoms the beam paths of the cavity mode are clearly visible, unstable cavity with beam walking out of alignment after a few passes is visible in the right picture.

CHAPTER 7

THE VACUUM SYSTEM

Experiments with cold atoms require to work at pressures much below atmospheric in the ultra high vacuum (UHV) regime, which is from 10^{-9} to 10^{-11} mbar. At this pressure the lifetime of the MOT is increased as there are less collisions with background atoms. The vacuum system is therefore the core of the experiment and everything else interfaces through it. The main points of consideration when designing this vacuum system were the integration of the ring cavity inside the vacuum and sufficient optical access for the MOT and cavity beams.

7.1 The Vacuum Chamber

The main chamber is a spherical octagon from Kimball Physics (MCF600m-SphOct-F2C8 6.00), it consists of two 6" CF ports, top and bottom and six 2.75" CF ports around the circumference. Eight of these ports are used for optical axis, one for mounting the dispenser arm and the last for connecting to the pumping arm of the vacuum system as shown in figure 7.1. A single chamber design was chosen with only a 3D MOT for trapping as it greatly simplifies the complexity of the vacuum system. However, since we will be loading atoms into the 3D MOT straight from background pressure, there will be a limit on how many can be captured and cooled. When a time comes that precooled atoms are needed from a 2D MOT, the system is designed for easy integration of a 2D MOT system by simply replacing the nipple with the dispenser feedthrough with a 2D MOT chamber. To reduce sensitivity to the magnetic field produced by the MOT, the chamber is made out of stainless steel 316L. Most of the other vacuum parts are also stainless steel 316L and only A4 bolts and washers were used to construct the vacuum.

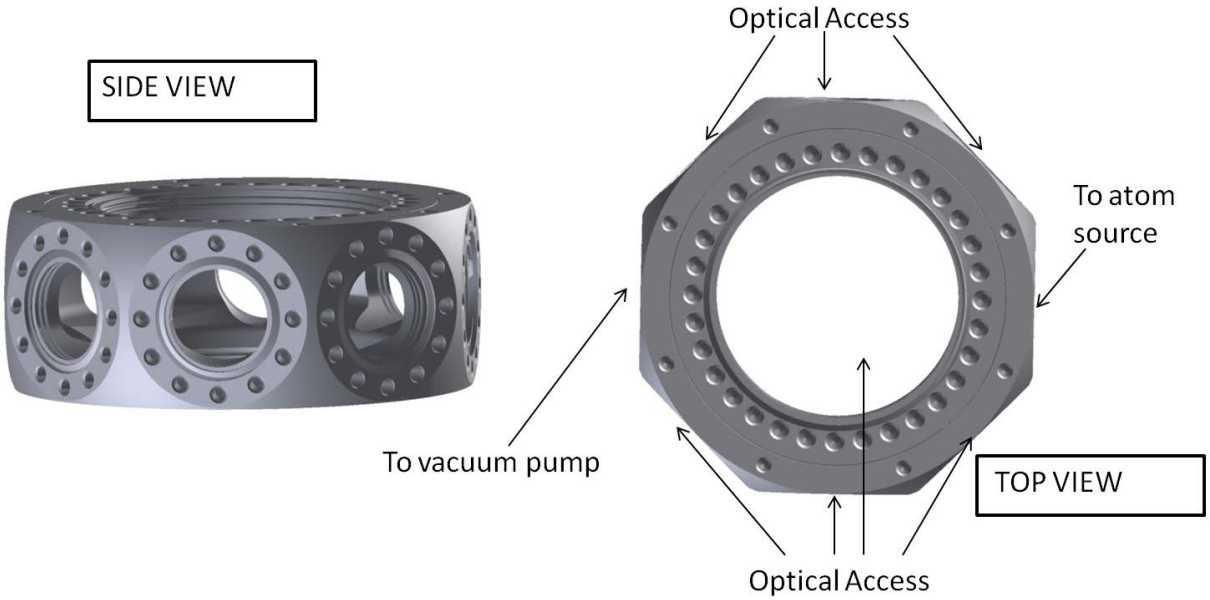

Figure 7.1: The spherical octagon used as the main experimental chamber of the experiment.

7.2 Viewports

The windows used for the chamber are kodial zero length viewports from Torr Scientific (VPZ38BBARLN). They have a broadband anti-reflective coating optimised for 700 - 1000 nm range with a specified minimum reflectance of 1% per face. The 2.75" CF viewports after coating have a clear aperture of 30 mm, this sets the maximum diameter of the MOT beams to be used in the experiment. The top 6" CF viewport has a clear aperture of 80 mm. The viewport flange material is made of stainless steel 316L as well. With regard to viewports, the popular choices are usually between fused silica and kodial glass. Fused silica has superior optical qualities (higher purity and fewer inclusions) but kodial glass has a higher bakeout temperature of $350°C$ as opposed to the maximum bakeout temperature of fused silica of $200°C$. The higher bakeout temperature was what ultimately led to us to choose kodial.

7.3 Vacuum Parts

The main consideration when choosing vacuum parts were on the maximum bakeout temperature and where stainless steel parts are used a 316L version was always sought. The part with the lowest bakeout temperature sets the maximum temperature the system can undergo during assembly. Connected to the chamber on the atom source side is a 2.75" CF nipple (FN-0275) from Kurt J Lesker. Connected on the end of the nipple is

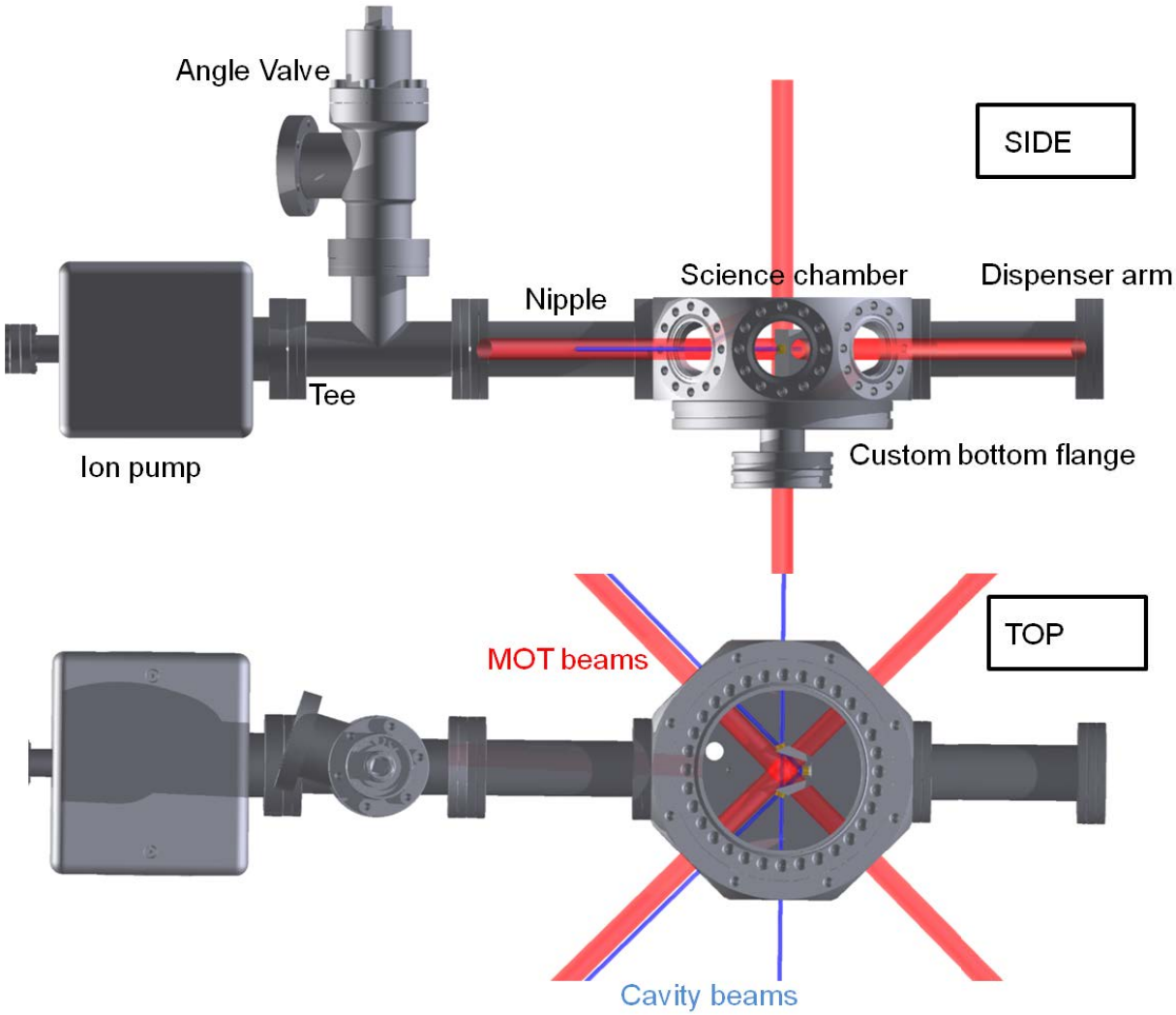

Figure 7.2: Top and side view of the full vacuum design.

an electrical feedthrough (Kurt J Lesker, EFT0043033) for providing current to drive the atom dispensers. On the vacuum pump side of the chamber is connected another 2.75" CF nipple which in turn is connected to a 2.75" CF tee. On the two output ports of the tee is connected an all-metal angle valve (VAT Vacuum Products Ltd, 54132-GE02-0001) which connects the vacuum system to a roughing/turbo pump system (Pfeiffer, TSU071/MVP). On the other port is connected a 20L/s starcell ion pump (Agilent Technologies, 9191145 Vacion Plus 20). The angle valve serves to connect the vacuum to the turbo pump and when a sufficient pressure is reached we can close the valve and switch to the ion pump without breaking vacuum, this way the turbo need not be a permanent part of the vacuum system.

7.4 Conductance calculations

In order to give a good understanding of mass flow in vacuum it is useful to describe how the freedom of movement experienced by a gas changes with decreasing pressure. At room temperature an air molecule's average velocity is governed by the Maxwell-Boltzmann velocity distribution and has a value $v \approx 5 \times 10^4$ cm/s. As the molecule propagates it collides with other air molecules in a particular density. The average distance between collisions is referred to as the mean free path and is inversely proportional to the pressure. For example O_2 or N_2 molecules at 1 mtorr pressure have a number density of 3.5×10^{13} cm^3 with a mean free path of 5 cm [9].

Within the vacuum chamber at atmospheric pressure the mean free path is roughly as described above, which is much smaller than the physical dimensions of the chamber. In this case the gas flow is determined by the intermolecular interaction of the air molecules. This results in viscous forces which make the gas behave as a homogeneous fluid. As such, gas flow in this regime is characterised as viscous flow. When the vacuum is pumped and the pressure, hence number density of the molecules decreases, the mean free path of the molecules increases until it is larger than the vacuum chamber itself. In this instant the gas flow is no longer characterised by the particles interactions, but rather the random motion of the individual molecules as they bounce around the walls of the chamber. In this regime gas flow is characterised as molecular flow. The transition from viscous to molecular flow happens typically at around 100 mtorr (0.1 mbar).

Discussion of conductance in the vacuum is limited to the molecular flow regime as the pressure of the chamber is much lower than the transition threshold for all cases of normal vacuum operation. The volume flow rate of a pipe is defined by its pumping rate [37] in Litres/second,

$$S = \frac{dV}{dt}, \tag{7.1}$$

where V is the volume of the pipe. The mass flow rate of a pipe is related to the volume flow rate and the pressure by the expression,

$$Q = PS, \tag{7.2}$$

where Q is defined as the throughput in mbar Litres/second and P is the pressure in mbar. The ability of a vacuum pipe to transmit mass is defined as its conductance, C. The throughput depends on the conductance of the pipe and the pressure difference across the pipe and has the expression,

$$Q = (P_1 - P_2)C. \tag{7.3}$$

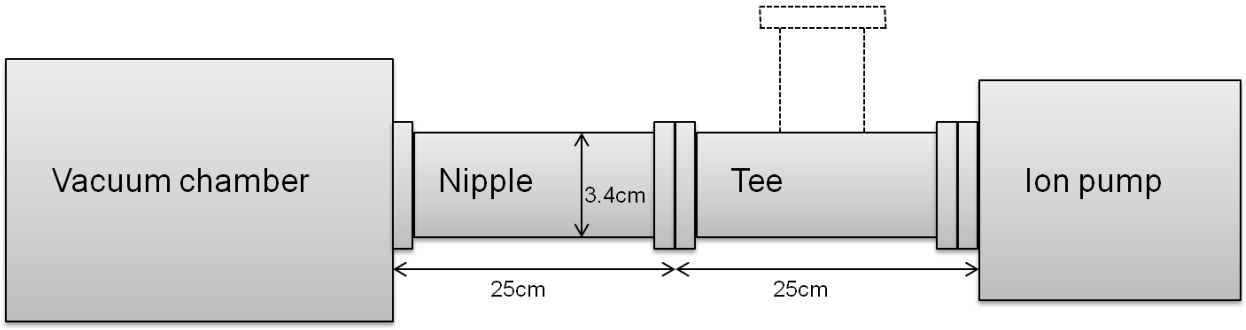

Figure 7.3: The effective path of pumping from the vacuum chamber to the ion pump.

The conductance of a pipe is measured in Liters/second, this is the same units as the pumping speed defined earlier. For a vacuum system to have efficient pumping it is necessary to select a pump that has an equal or higher pumping speed than the conductance of the vacuum. To work out the conductance of the vacuum system it is necessary to add up the conductances of the components between the vacuum chamber and the ion pump. Figure 7.3 shows the path between the chamber and pump for our system. There are two pipes for conductance consideration, a nipple and a tee. The upper arm of the tee is ignored for conductance calculation as there is no path for atoms to exit from there. To add the conductance of two or more pipes in series, similarly to electric theory we can replace the connected system with a single equivalent conductance, C_{series}, given by

$$C_{series} = \left[\frac{1}{C_1} + \frac{1}{C_2}\right]^{-1}. \tag{7.4}$$

The conductance of a pipe in the molecular flow regime with length L and diameter D can be calculated using the equation,

$$C = 2.6 \times 10^{-4} \nu \frac{D^3}{L}, \tag{7.5}$$

where ν is the average molecular velocity in cm/s and length and diameter are in centimeters. For air at room temperature this equation becomes,

$$C = 12\nu \frac{D^3}{L}. \tag{7.6}$$

For our system $D = 3.4$ cm and $L = 25$ cm for both the nipple and the tee. Putting these numbers into equation 7.6 and using equation 7.4 to calculate the resultant conductance we get a value of 18.8 L/s. This shows that our 20 L/s ion pump is enough for efficient pumping of the vacuum system.

7.5 Custom Bottom Flange

The bottom flange for the cavity was required to be custom built as it had to house the ring cavity and the electrical feedthrough for the piezo. Standard flanges from vacuum vendors were unsuitable for the job, therefore a standard flange was bought and modified for the experiment. The base flange was a 6" CF flange from MDCvacuum (110025). Figure 7.4 shows the real estate requirements for the flange. 1,2 and 3 are the bolt holes for mounting the cavity, 4 is a through hole where the electrical feedthrough for powering the cavity piezo would be welded. As the feedthrough pins protrude more than 30 mm they could potentially block the MOT beams and/or the cavity beams. Therefore, it was important to place the feedthough away from any of these beam paths. At the same time we had to ensure they were also not impeding the atom source. This left behind the cavity on the pumping side of the chamber as the only viable option. Marker

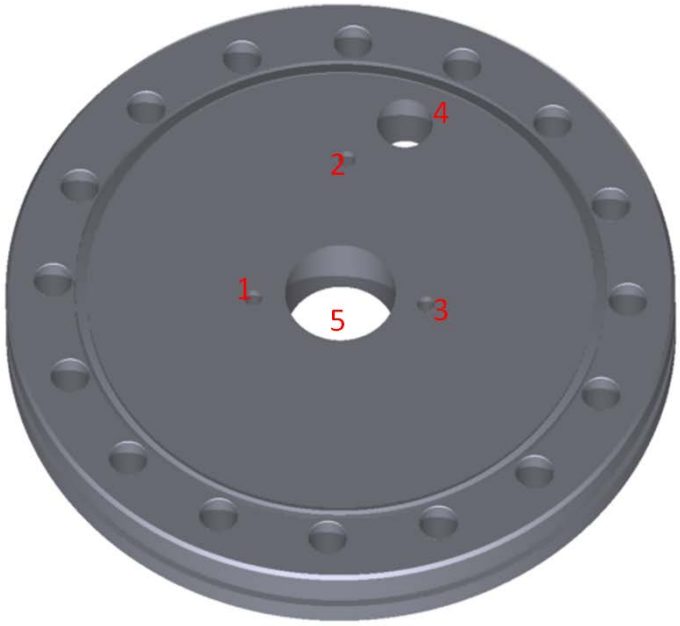

Figure 7.4: The custom bottom flange for the vacuum chamber with the positions of the cavity bolt holes (1,2,3), electrical feedthrough (4) and MOT beam hole (5) indicated.

5 indicates the position for the hole to give optical access for the top and bottom MOT beams. Originally we had planned to simply attach a viewport directly to the bottom flange. However, we discovered that the bolt holes for a 2.75" CF viewport would coincide with the bolt holes for the cavity on the other side of the bottom flange. This left us with the option of increasing the viewport size, which was not viable as the viewport mirror diameter would be larger than the bolt holes for the cavity would allow. Also a smaller

viewport was not an option as the clear aperture of the windows would not be large enough for the MOT beams. The final solution came in the form of an extending pipe welded to one side onto the hole and a 2.75" CF flange welded on the other side. A viewport is then attached to the bottom flange as shown in figure 7.5.

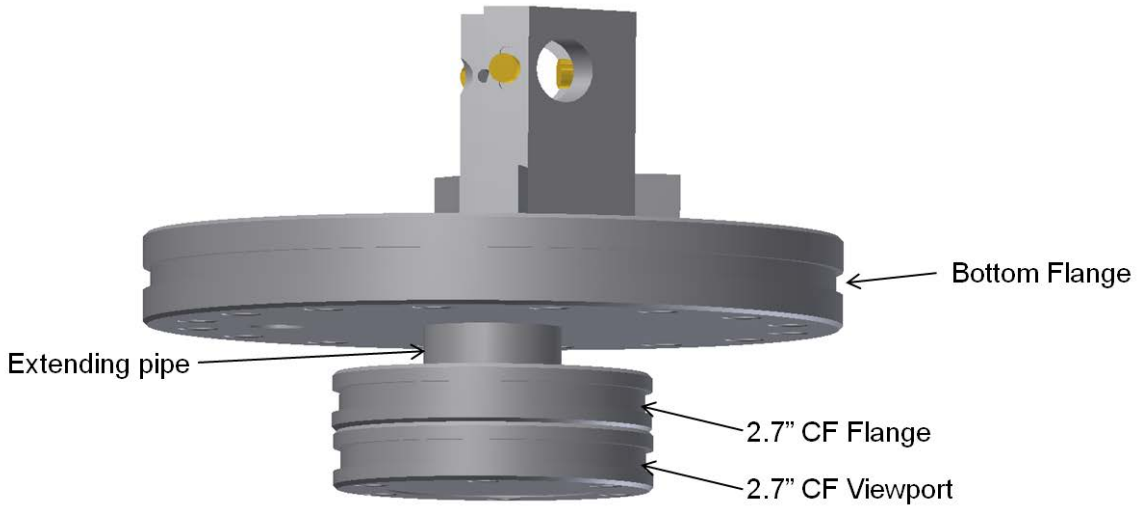

Figure 7.5: The custom bottom flange for the vacuum chamber showing the extending pipe welded between the bottom flange and a 2.75" CF flange and a viewport subsequently attached to the flange.

7.6 Dispenser Arm

The atom sources for the experiment are Potassium dispensers from SEAS Getters (K/NF/4.5/25 FT10+10). A dispenser is a thin trapezoidal shaped stainless steel vessel with a Potassium compound inside as shown in figure 7.6.

At room temperature the compound is stable, but when a few amps are passed through the dispenser it heats up to a few hundred degrees. This causes a reduction reaction which releases Potassium atoms. Due to the high current and narrow exit slit the atoms released from the dispenser have a high velocity and a nozzle effect would also be expected, where higher velocity atoms exiting the slit collide with and speed up slower moving atoms released earlier. This has the overall effect of shifting the velocity distribution of the atom jet to the higher end of the spectrum. As we are loading the MOT directly from the background it is not ideal to have a supersonic jet of atoms aimed at the MOT beams as the typical trapping potential for a MOT is small compared to the thermal energies of the atoms. To produce an atom source with a more balanced thermal distribution, the dispensers are instead aimed at the nipple they are housed in. The atoms stick to

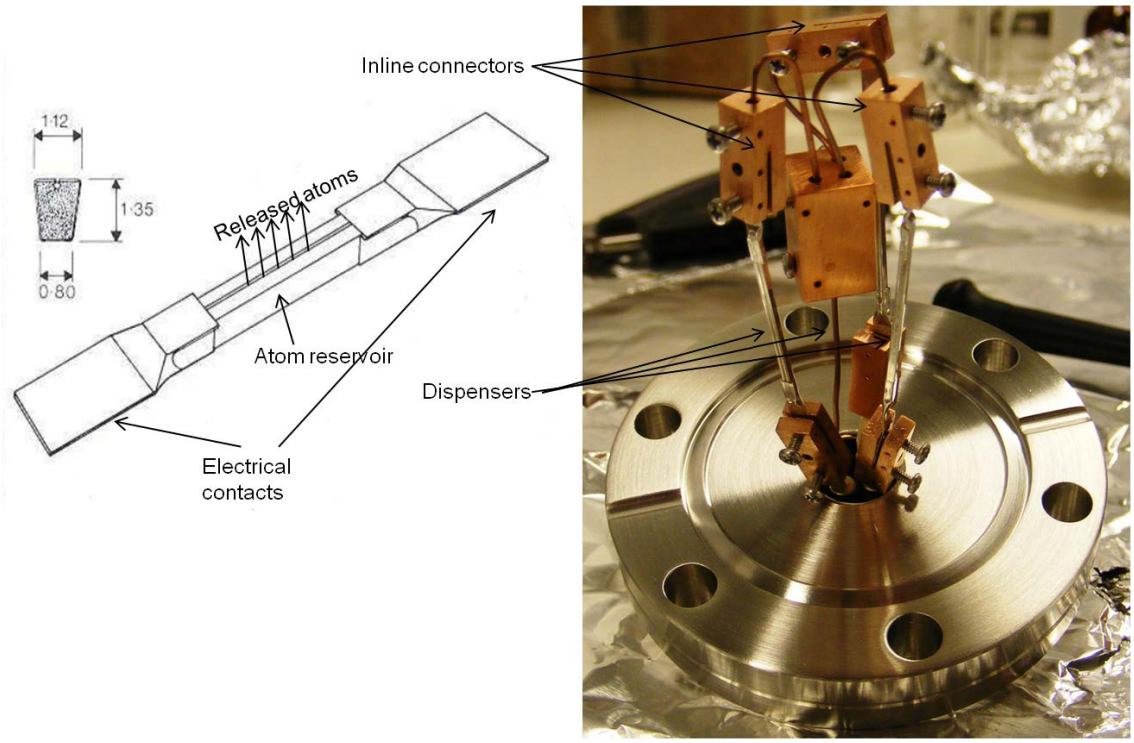

Figure 7.6: Cross section of an atom dispenser showing typical dimensions in mm and notable features (left) and the electrical feedthrough driving the dispensers and the configuration of the inline connectors securing the dispensers (right).

and coat the inner walls of the pipe. Flexible resistive heaters (Thorlabs, HT10K) are wrapped around the outer circumference of the nipple and the pipe is heated to roughly fifty degrees Celsius as shown in figure 7.7. The atoms desorp from the walls with an even Maxwell Boltzmann thermal distribution and atoms at the lower energy spectrum are subsequently captured by the MOT beams and form the MOT.

In total three dispensers are placed in the system, they are attached to an electrical feedthorough (Kurt J Lesker, EFT0043033) which has four pins. Three for providing driving current for the dispensers and one common pin. The dispensers are attached to the pins through custom copper inline connectors as shown in figure 7.6. The connectors have a hole on one end to attach to the pins and a slot on the other to secure the electrical contact tab of the dispenser. A large inline connector is used at the top to connect the dispensers to the common pin. Care is taken during assembly to ensure the connectors and the dispensers do not touch each other or the walls of the nipple, as to not cause any shorts.

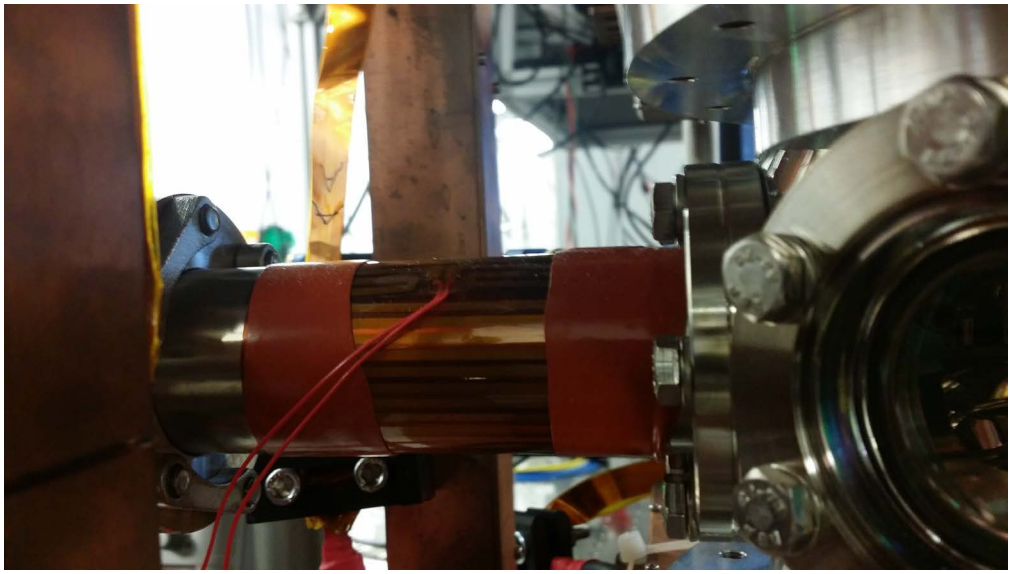

Figure 7.7: Flexible resistive heaters wrapped around the dispenser arm.

7.7 Vacuum Assembly

As a wide variety of components had to exist inside the vacuum, it was essential that they all be exceptionally clean. Two cleaning procedures were specified depending on the initial state of the component. For custom components that were greasy from the manufacturing process like the cavity frame and the copper inline components, the following procedure was used.

1. Removal of excess bulk with hard brush under running tap.
2. Ultrasonic bath of Liquinox with a dilution ratio of 1:10 with distilled water, ten minutes.
3. Ultrasonic bath of distilled water, ten minutes.
4. Ultrasonic bath of Acetone, fifteen minutes.
5. Ultrasonic bath of Isopropanol, ten minutes.

For components coming from vacuum manufactures for example the tee, nipples and feedthroughs it was assumed that they are 'pre-clean' and therefore had a less rigorous cleaning procedure. The following procedure was used.

1. Ultrasonic bath of distilled water, ten minutes.
2. Ultrasonic bath of Acetone, fifteen minutes.
3. Ultrasonic bath of Isopropanol, fifteen minutes.

Some components came vacuum ready and did not need to be cleaned. This included the piezo, cavity mir-

rors and copper gaskets. The piezo and copper gaskets were opened just before assembly and given a simple Acetone and Isopropanol wipe with lens paper.

Once cleaned the next step was to assemble the parts, the most sensitive operation of this stage being the attaching of the ring cavity to the bottom flange. Two main issues were taken into consideration, firstly the possibility of the cavity and the screws used to secure it seizing during the bake. Seizing occurs when like metals in close contact are heated to high temperatures, this is the main reason anti-sieze lubricant is used when bolting vacuum components together. However in this case as anti-sieze lubricant is not vacuum compatible it can not be used on the bolts that secure the ring cavity. Seizing however does not occur between different types of metals, to this end we used brass bolts to secure the cavity. Brass is a relatively soft metal compared to stainless steel so therefore would not sieze with the stainless steel at high temperatures. At worst case the brass bolt would deform and need replacing but would not damage the threading in the bottom flange bolt holes. Though we are using brass bolts it is not uncommon to use Silver coated stainless steel bolts in this situation.

The second issue for consideration is the potential for virtual leaks to occur in the bolt holes of the bottom flanges. Virtual leaks occur when you have a volume of air trapped within the chamber, as the gas is slowly released from the trapped volume it acts as if there is a leak in the vacuum system from that location. In our system as we are securing the ring cavity into a blind hole, if the bolt does not touch the bottom of the hole when fully bolted a small volume of gas would be trapped and can only escape by migrating through the bolt and hole threads as shown in figure 7.8. This problem is solved by drilling a vent hole in the bolt to allow the gas to escape in bulk.

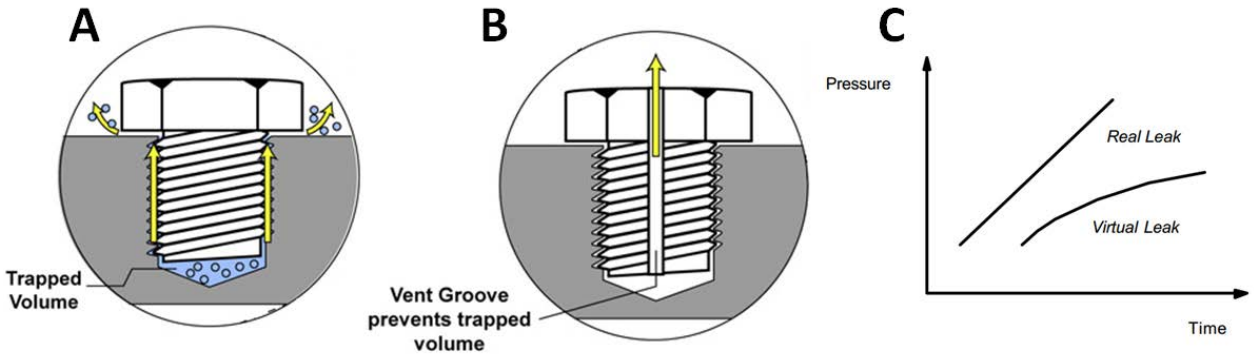

Figure 7.8: 2D slice across a vacuum part showing (A) The appearance of a virtual leak when a volume of air is trapped by a bolt in a blind hole. (B) Vent hole that allows the trapped volume to escape. (C) Graph showing the difference between a real leak and virtual leak.

However in the event a leak is present in a vacuum system it is possible to differentiate the presence of a real leak from a virtual one. The leak rate from a virtual leak will eventually decrease over time as the reservoir of gas is depleted. Whereas a real leak has a virtually unlimited reservoir and therefore the pressure in the vacuum would increase at a constant rate as shown in figure7.8.

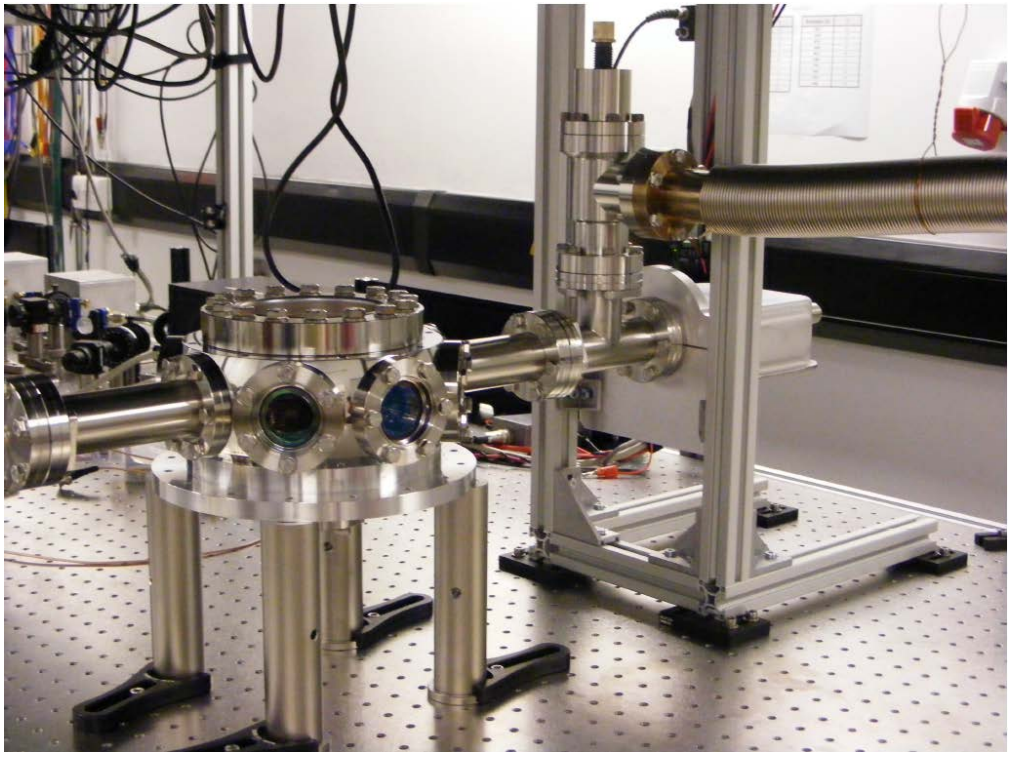

Figure 7.9: Fully assembled vacuum system.

After attaching the cavity the rest of vacuum components are assembled and sealed as shown in figures 7.9, 7.10. The vacuum system is supported onto the optical table by a custom circular aluminum stand bolted onto the vacuum chamber. It is held up by four 1" mounting posts and on the other end of the vacuum system there is a custom vertical mount securing the ion pump flange. The vertical mount has adjustable height to ensure the system across its length is on the same plane and weight is distributed evenly across. This is to ensure that there are no stresses on the vacuum flange connections which could lead to a leak developing. The next step in the process is to bake the vacuum system. This is done to eliminate the residual outgassing of the components after pumping.

Outgassing is the desorption of gases or vapors from the material surfaces of the components, this has the effect of increasing the pressure of the vacuum being pumped. Outgassing rates are typically much slower

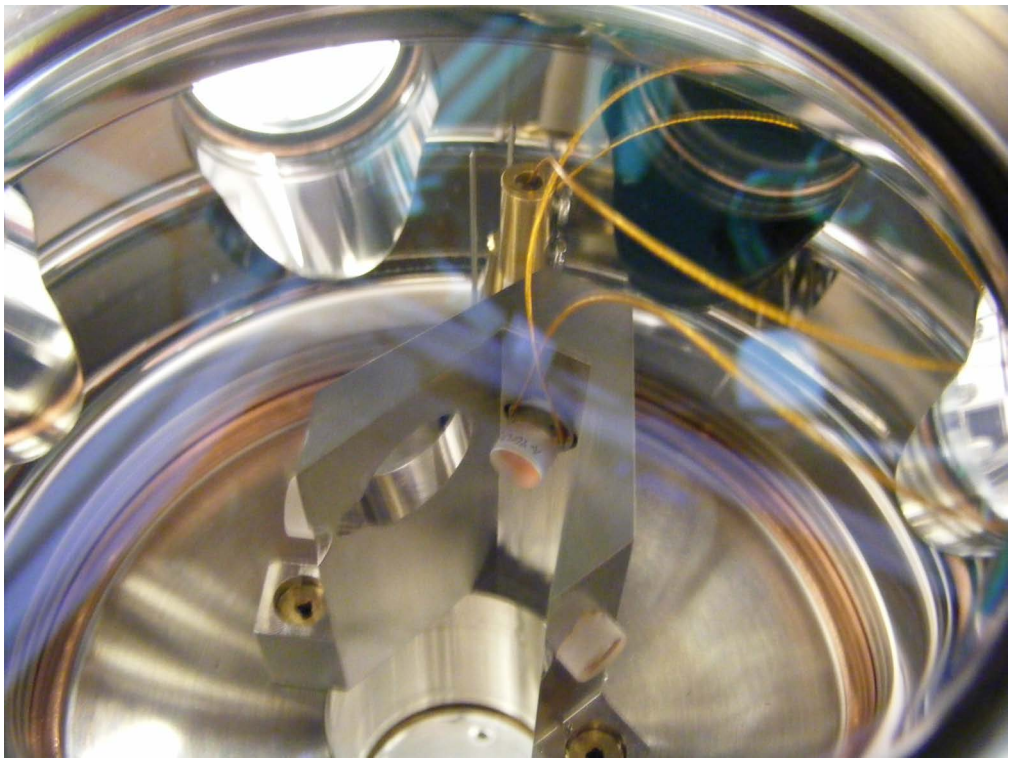

Figure 7.10: The cavity inside the vacuum chamber.

than any reasonable time frame of which you can simply wait until the components are fully desorped of outgassing material. So to speed up the process the entire vacuum system is baked to high temperature, typically 100-300 degrees Celsius depending on the system. This has the effect of dramatically increasing the rate of desorption of the material surfaces which ultimately leads to a lower overall vacuum pressure.

On deciding on a temperature of which to do a bake it is important to take into account the maximum operating temperatures for all the components inside the vacuum. The max operating temperatures for all our intra-vacuum components are given in the following table,

Stainless steel parts	$500°C$
Piezo power feedthrough	$450°C$
Dispenser current drive feedthrough	$450°C$
Piezo	$200°C$
Ring cavity mirrors	$300°C$
Viewports	$350°C$
Brass bolts	$500°C$
Dispensers	$500°C$
Copper inline connectors	$300°C$
Macor spacer for piezo	$800°C$

From this it can seen that the limiting temperature is the max operating temperature of the piezo, therefore this sets the limit of the baking procedure. The majority of the outgassing is water vapour from the stainless steel surfaces. Therefore, as long as the bake is done at over $100°C$ it should be sufficient and offsetting a lower temperature bake with a longer duration one will achieve the same results. To bake, the system is wrapped in heating tape with care taken to avoid direct contact of the heater tape with the viewports glass surfaces as this would cause inhomogenous heating across the glass which cause thermal stresses that can crack the glass.

The system is then wrapped in multiple layers foil to provide insulation. The temperature of the tape is slowly ramped over the course of two days until a steady temperature of roughly $160°C$ is reached. The bake is maintained for a week before ramping down. Figure 7.11 shows the trend of the pressure change as we baked. There is an inital spike in pressure as the chamber gets to temperature which we can associate with an increase in the desportion rate of the system and this stays relatively high during the duration of the bake. When the bake is ramped down we can see that the pressure also decreases and ultimately settles at a value magnitudes lower than the initial pressure at 5×10^{-9} mbar. The pressure is measured using a gauge attached to the turbo pump end of the system and reading the current of the ion pump and converting it to a pressure reading.

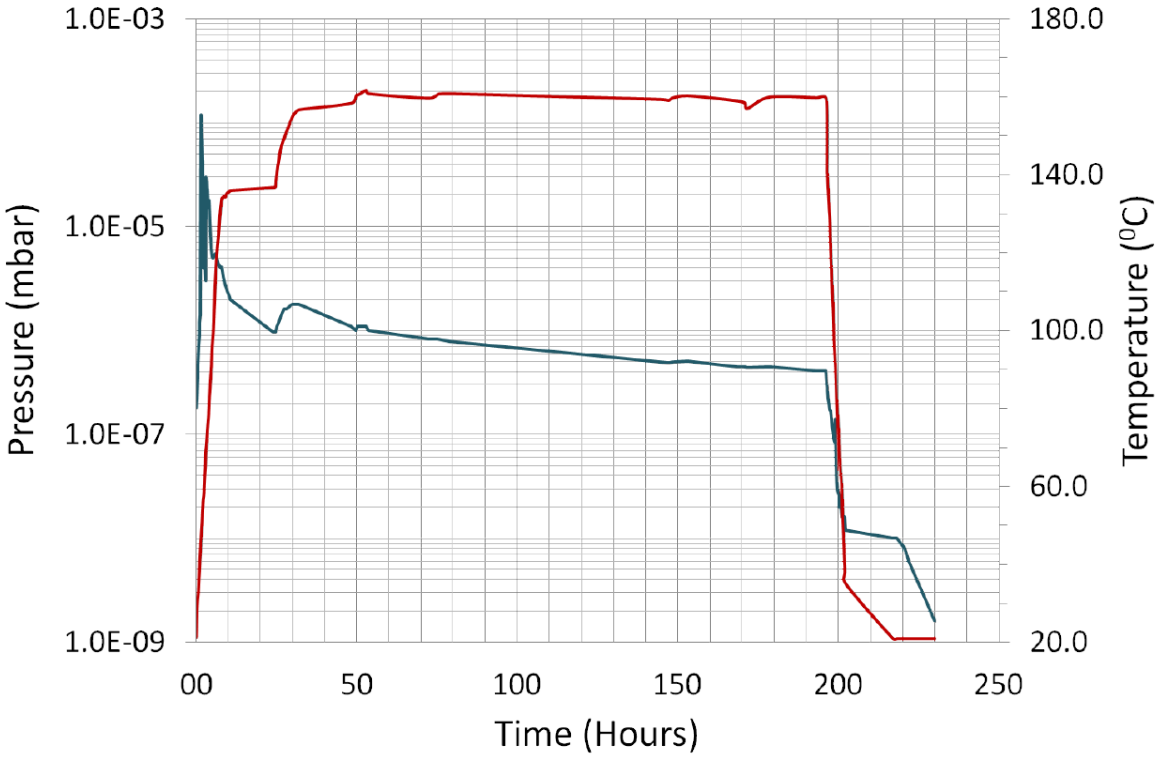

Figure 7.11: Pressure change in the vacuum as the system is baked with temperature (red) and pressure (blue).

CHAPTER 8

BUILDING THE EXPERIMENT

The experimental results of this chapter have been published in [38], [42]

L Mudarikwa, K Pahwa, and J Goldwin. Sub-Doppler modulation spectroscopy of potassium for laser stabilization. Journal of Physics B: Atomic, Molecular and Optical Physics, 45, 2012.

K Pahwa, L Mudarikwa, and J Goldwin. Polarization spectroscopy and magnetically-induced dichroism of the potassium D2 lines. Opt. Express, 20, 2012.

This chapter details the designing and building of the systems involved in producing the magneto-optical trap. Firstly the lasers systems for generating the light at the right wavelengths and the methods we studied to stabilise the wavelength of the lasers. The magnetic coil system used to provide magnetic trapping for the atoms is described, which has a non standard geometry for 3D MOT setups and finally the MOT itself is characterised to calculate the number of cold atoms trapped.

8.1 Laser Systems

For the cooling and trapping of atomic species, specifically alkali metals, lasers are required whose frequencies are near the cooling transitions of the atoms. These lasers have to be stable to within the natural linewidth of the atoms, which is typically a few MHz. This section describes the buiding of the lasers used for cooling and the techniques used to stabilise their wavelength.

8.1.1 Custom ECDLs

Three lasers used in the experiment are custom built extended cavity diode lasers (ECDLs). The lasers are in the Littrow configuration [27] in which an external diffraction grating is used to extend the length of the

laser cavity used for generating optical feedback. The longer cavity has the effect of lowering the linewidth of the cavity and the wavelength selectability of the diffraction grating further reduces the linewidth of the laser. Figure 8.1 shows a schematic of a basic ECDL in Littrow configuration.

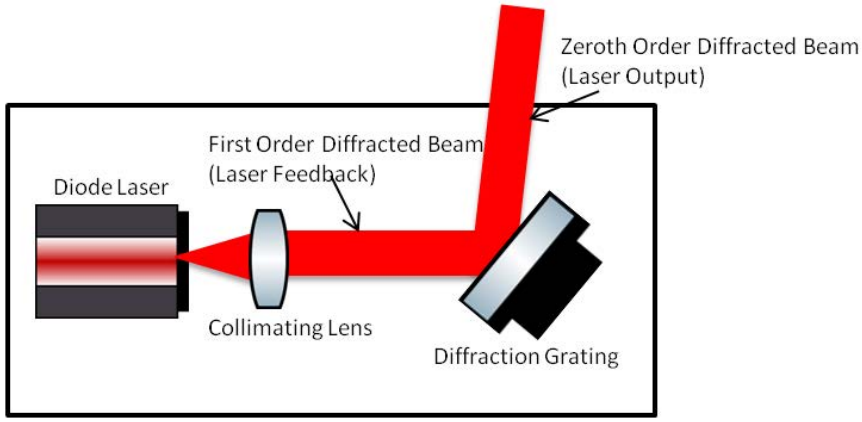

Figure 8.1: The EDCL in the Littrow configuration.

For our experiment ECDLs were custom built by the machine shop at the School of Physics at Imperial College, London. They consist of an aluminum square outer body which serves as an interface for the electrical connections for the laser, it has a thick base which serves as a heat sink and an interior aluminum block acts as the laser head for the device. The laser is an AR coated GaAs semiconductor diode from Eagleyard (EYP-RWE-0790-04000-0750-SOT01-00001). The diode is housed inside a lens tube with a collimating lens on the output (Thorlabs, C240TME-B). The diffraction grating used is a 1200 lines/mm holographic grating which is glued to a kinematic mount (Radient Dyes, MNI-H-2) and a piezo is placed between the kinematic mount and the interior block. The knobs on the kinematic mount are used for wide tuning of the laser output wavelength while the piezo is used for finer scanning of the laser wavelength as well as for active feedback in the stabilisation setup. The interior aluminium block sits ontop of a flat peltier module (RS Components, 490-1525) to provide active temperature stabilisation of the laser head. A small thermistor is used to measure the temperature.

The lasers are operated at a wavelength of 766.7 nm at a current of $\approx$ 70 mA giving an output power in the range of 18 - 20 mW and the temperature is stabilised at $17°C$. Current is provided by the Thorlabs Benchtop LD Current Controller (LDC202C) for one the lasers and Wavelength Electronics laser diode driver (MPL250) for the other two. Temperature control is provided by the Thorlabs Benchtop Temperature Controller (TED200C) for one of the lasers and Wavelength Electronics Temperature Controller (PTC2.5K-CH) for the other two. The beam waist of the master laser was measured using the razor blade translation

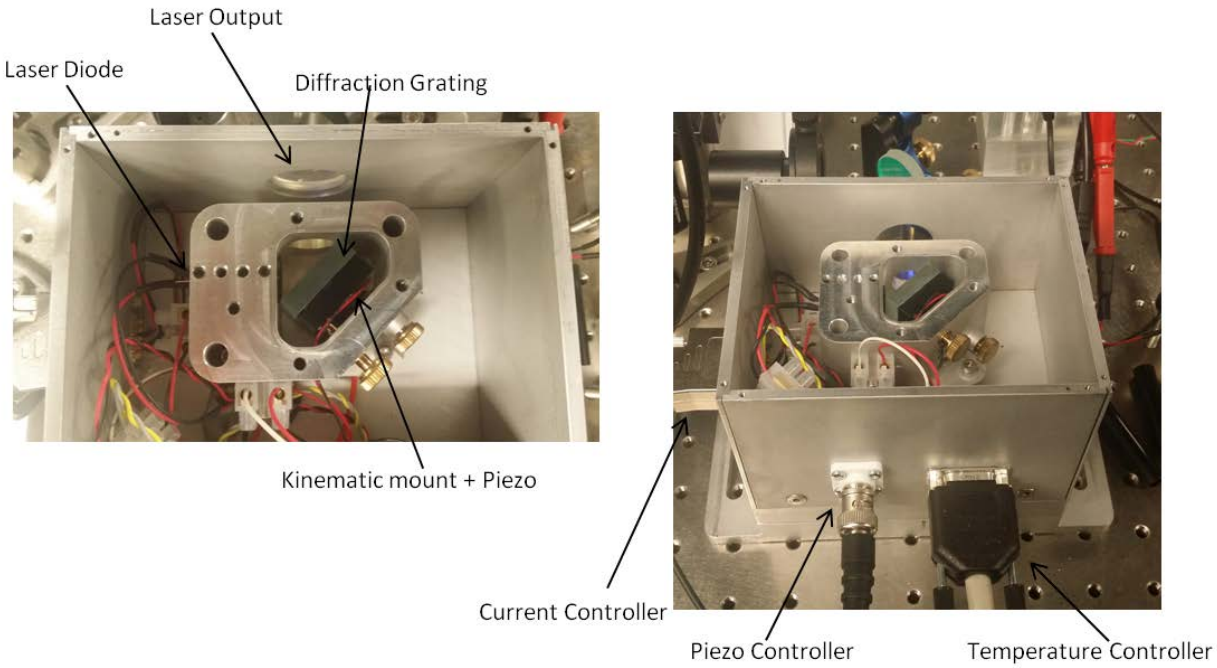

Figure 8.2: The EDCL mechanical construction.

technique. This works by measuring the beam power on a photodiode while cutting across the beam with a razor blade. The unblocked power of the beam is given by

$$P(x) = \int_{x}^{-\infty} I_0 e^{-2\frac{(x-x_0)^2}{\omega^2}}, \tag{8.1}$$

where I_0 is the peak intensity of the beam, x_0 is the position of the razor at peak intensity and x is the position of the razor as it cuts across the beam. This equation can be integrated and the resultant expression given below can be fitted with an error function to calculate the beam waist, ω

$$P(x) = \frac{1}{2}\sqrt{\frac{\pi}{2}} I_0 (1 + Erf[\sqrt{2}\frac{x - x_0}{\omega}]), \tag{8.2}$$

where Erf is the error function. Data is taken for the vertical and horizontal width of the beam and is shown in figure 8.3. From this, beam measurements of $\omega_x = 1.59 \pm 0.03$ mm and $\omega_y = 1.506 \pm 0.006$ mm were observed, these readings were taken 4 meters away from the laser output face.

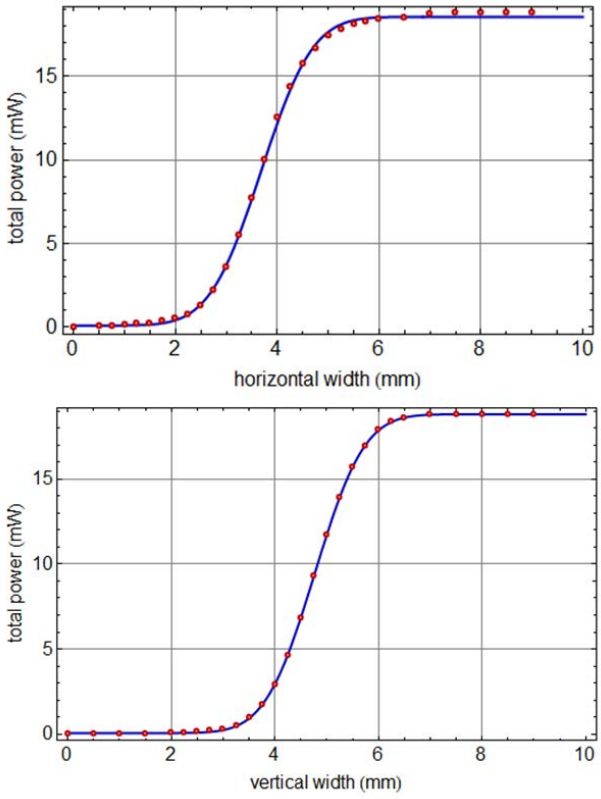

Figure 8.3: Measurement of the beam size of the laser output. TOP: Measurement of the horizontal width. BOTTOM: Measurement of the vertical width.

8.1.2 Atomic Laser Locking Techniques

For active stablilisation of the lasers we investigated a number of atomic locking schemes, they fell into the categories of modulation based techniques and modulation free techniques. The work on this has been published into two papers and can be found in references [38], [42].

Saturated Absorption Spectroscopy

One of the simplest methods of obtaining frequency discriminants near the cooling wavelength is sub-Doppler saturated absorption spectroscopy [52], [24], [16]. In this method a weak probe beam is passed through an atomic cell and at the same time a strong pump beam of the same frequency is counter-propagated through the cell. Normally if there was no pump beam the probe signal through the cell would be roughly a Gaussian absorption feature, Doppler-broadened to a width of a few hundred MHz. When the pump is introduced the two beams are only simultaneously resonant for atoms with zero velocity along the optical axis. For

these atoms the pump beam reduces the ground-state population, and therefore the absorption, leading to a narrow Lorentzian feature known as a Lamb dip [43], [3]. Figure 8.4 shows the typical layout for a saturated absorption setup and the corresponding signal.

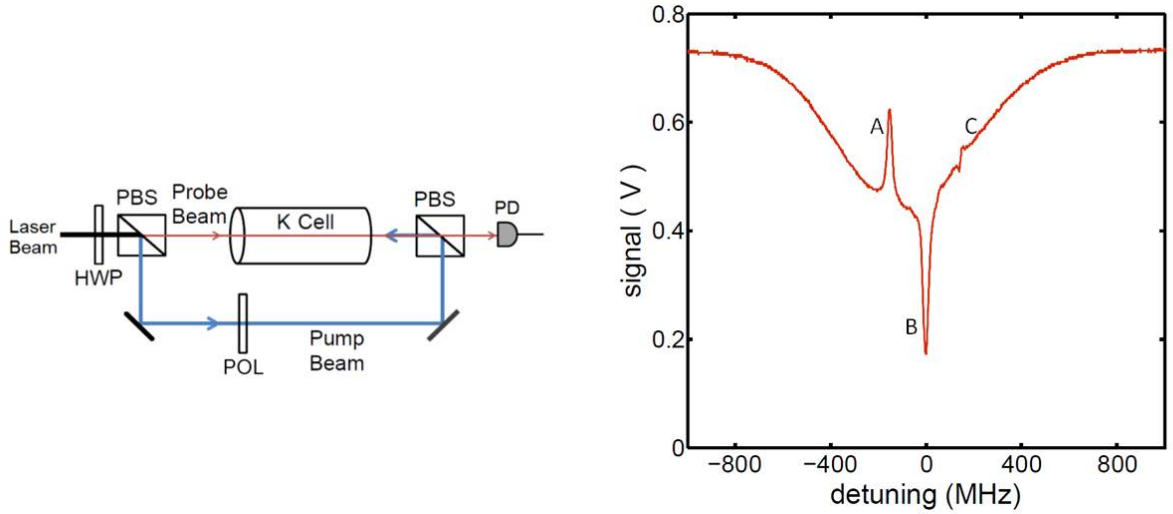

Figure 8.4: Setup for saturated absorption spectroscopy and the corresponding spectral features of the probe beam.

A laser beam is split by a polarising beam splitter (PBS) with a half-wave plate (HWP) used to control the intensities of the subsequent beams. The beams are passed through opposite directions of a Potassium vapour cell (Thorlabs, CP25075-K) which is heated to $45°C$ and the probe beam is made incident on a photo-diode. The saturated absorption spectrum shown in figure 8.4 shows the narrow spectral features which are used as frequency discriminants. These spectral features correspond to transitions of the D2 line of Potassium. Figure 8.5 shows the energy level diagram for these tranistions for ^{39}K and ^{41}K isotopes with natural abundances of 93.3% and 6.7% respectively.

Feature A in figure 8.4 is a composite of the ^{39}K F=2→F'=1,2,3 transitions. Feature B is a so called ground state crossover transition, these are transitions for frequencies halfway between the two ground states and the excited state. Atoms moving in opposite directions with a Doppler velocity halfway between F=1 and F=2 which we call ν_+ and ν_- are resonant at the same time with the F=1 → F' and F=2 → F' transitions for the pump and probe beam respectively. This leads to optical pumping of the probe beam ground state, which results in increased probe absorption at that frequency. This manifests as a dip at the crossover frequency. Feature C is a composite of the ^{39}K F=1 → F'=1,2,3 transitions and ^{41}K ground state crossovers, hence the slight dispersive shape. However, since it is barely resolved, it is largely ignored for this work. The isotope

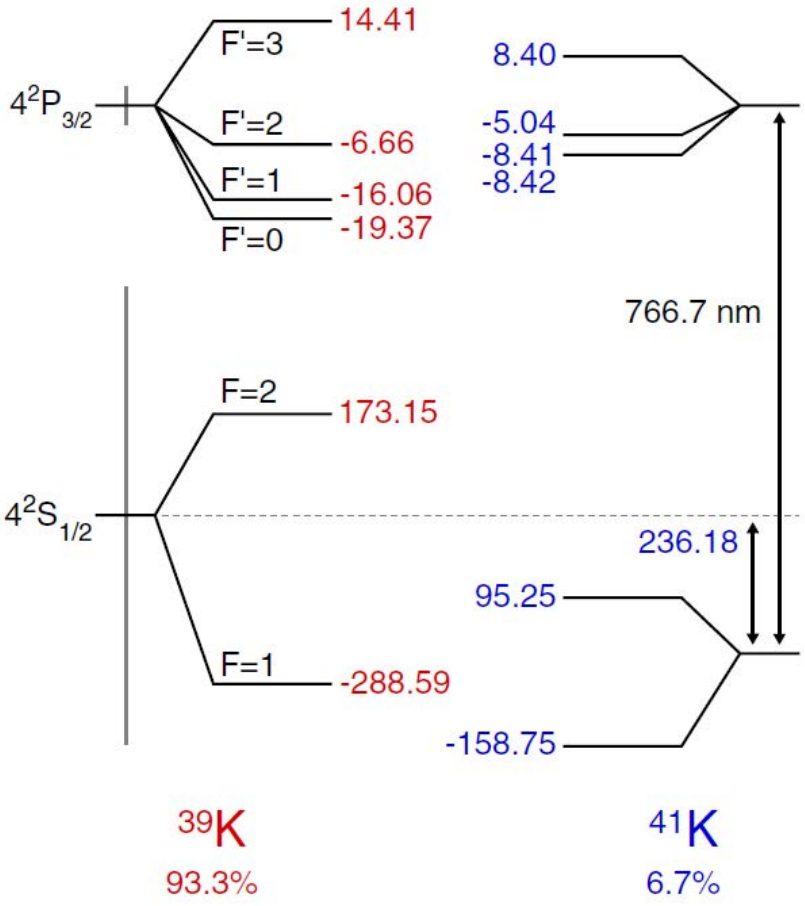

Figure 8.5: Energy level spectrum for the D2 line of ^{39}K and ^{41}K. The grey lines crossing over the ground and excited levels show the Doppler linewidth and natural linewidth respectively. Units are in MHz detuning from the fine structure transition.

shifts for Potassium are small compared to the Doppler width, therefore all the transitions overlap to form a single Doppler profile.

However in this form these features are unsuitable for use. A typical servo control requires an error signal which is proportional to changes in frequency in the vicinity of a zero-crossing, which sets the lock point. To this end a variety of methods have been developed for producing more robust error signals.

Modulation Spectroscopy

The first set of experiments done involved modulation of the frequency of the beams, the first of these was the direct modulation of the probe beam [36]. To obtain phase modulation, we used a home-built electro-optic modulator (EOM). An operational amplifier and resonant resistor-inductor capacitor (RLC)

circuit were used to drive the crystal at 9.62 MHz. The modulation was generated by a four channel direct digital synthesis evaluation board (analogue devices, AD9959/PCBZ-ND) which allowed adjustment of the relative phase between the local oscillator (LO) and the radio-frequency (RF) signal from the photodiode during demodulation. Figure 8.6 shows the setup for direct modulation and the error signals produced. The counter-propagating pump and probe beams have orthogonal linear polarisations so they can be easily

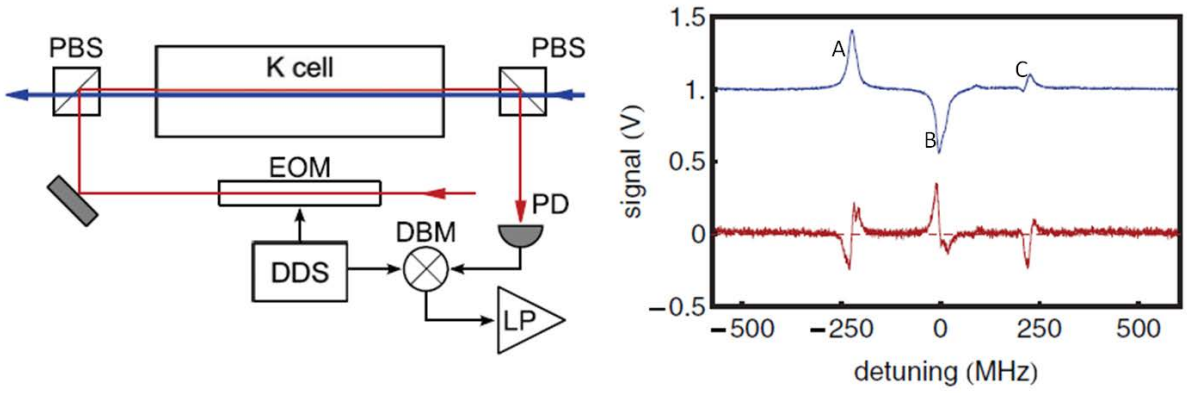

Figure 8.6: (Left) The setup for direct modulation spectroscopy. The blue line represents the pump beam and red is the probe. (Right) Upper trace shows a substracted saturation absorption signal and the lower trace the direct modulation signal.

separated and combined using PBSs. The pump beam interacts non-linearly with the atomic medium to cause differential absorption of the carrier and side-bands of the probe beam. This differential absorption results in the error signal shown in figure 8.6. This signal looks like the derivative of the absorption peak, similar to the frequency modulation technique for optical cavities studied in chapter 5. The composite structures of the features A and B have shown up as kinks in the error signal. An undesirable kink in the B feature appears near the zero crossing. This kink can be moved away from the center by using suitable pump and probe powers.

The second modulation technique studied was modulation transfer spectroscopy [54], [64]. In this case instead of directly modulating the probe, the modulation is on the pump beam which then transfers it to the probe beam. Figure 8.7 shows the setup for modulation transfer and the error signals produced. The modulation is transfered from the pump to the probe beam through a four-wave mixing process [57], [19] where the carrier and one sideband of the pump beam mixes with the probe to form a fourth frequency component which is a sideband of the probe, this occurs for each sideband of the pump beam. We found modulation transfer to work better at low modulation frequencies and we used 1.82 MHz for the measurements shown

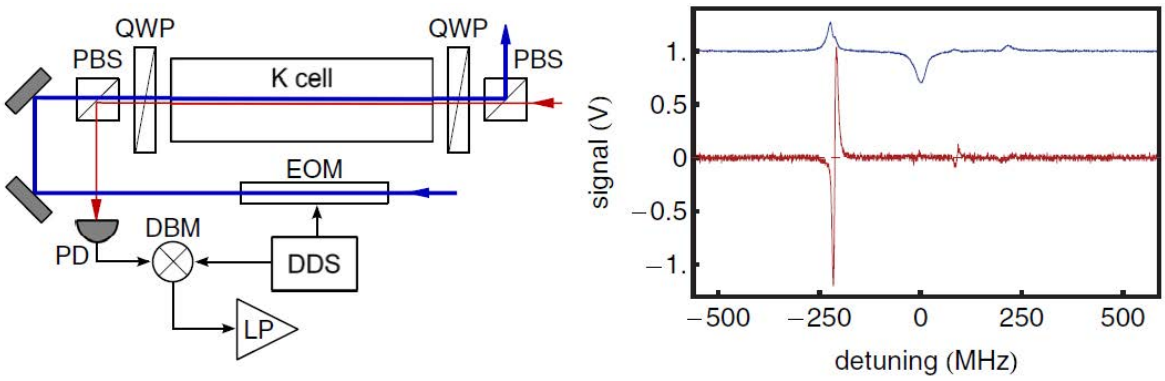

Figure 8.7: (Left) The setup for modulation transfter spectroscopy. The blue line represents the pump beam and red is the probe. (Right) Upper trace shows a substracted saturation absorption signal and the lower trace the modulation transfer signal.

here. The polarisation of the pump/probe beams produced the best results when changed from orthogonal linear to σ_+-σ_- circular polarisation. The signal amplitude for the A feature error signal more than doubled but at the cost of the errors signals for the B and C features. Modulation transfer favors cycling transitions were the inherently weak four-wave mixing process can occur multiple times, this explains why feature A, which has a cycling transition F=2→ F'=3 has a large signal and the rest are suppressed. This also has the additional effect of suppressing the Doppler background.

Modulation Free Spectroscopy

The second set of experiments involved investigating modulation free methods of atomic spectroscopy. The first technique studied was polarisation spectroscopy [63], [26], [58]. This technique utilises a circularly polarised pump beam to induce optical anisotropy in the atomic medium. This anistropy manifests as an asymemetric population redistribution of the Zeeman substates. Figure 8.8 shows the setup for generating polarisation spectroscopy.

A solenoid wrapped around the K cell is used to produce a weak magnetic field (22.8mG) along the optical axis setting quantisation axis for the atoms. For a field pointing in the pump beam direction, left-hand circularly polarised light will drive σ_+ transitions into high Zeeman sublevels resulting in a non-uniform redistribution of these states. A linearly polarised beam can be considered a coherent superposition of left and right circularly polarisation, therefore a linearly polarised probe beam through the K-cell will experience differing phase shifts and aborpostion due the birefringence and dichroism induced by the pump.

From the figure we can see the pump is circularly polarised by passing it through a quarter wave plate

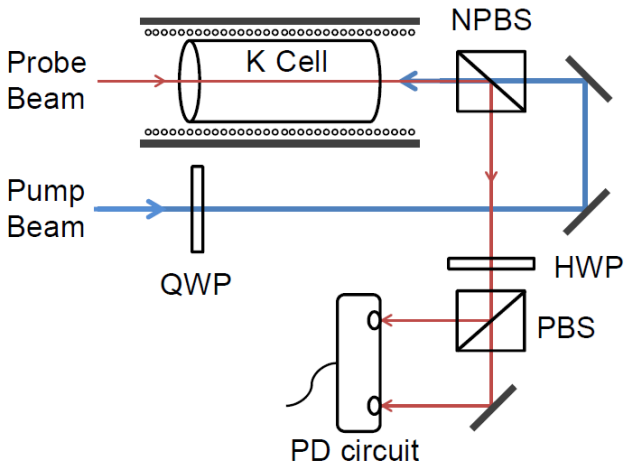

Figure 8.8: Setup for generation polarisation spectroscopy signal.

(QWP) before passing through the K-cell. A linearly polarised beam is counter-propagated through the cell and a PBS is used split the beam into its component circular polarisation parts. These two subsequent beam are incident on a custom built subtracting photodiode circuit. The circuit has two photodiodes which each receive the beam and the difference between the beams is outputted to an oscilloscope. In the absence of the pump no anisotropy is present in the atomic medium and the two output beams of the PBS are equal. However, when the pump is introduced the linear probe gains an ellipticity and the difference signal becomes non-zero. Figure 8.9 shows the error signals generated from this method.

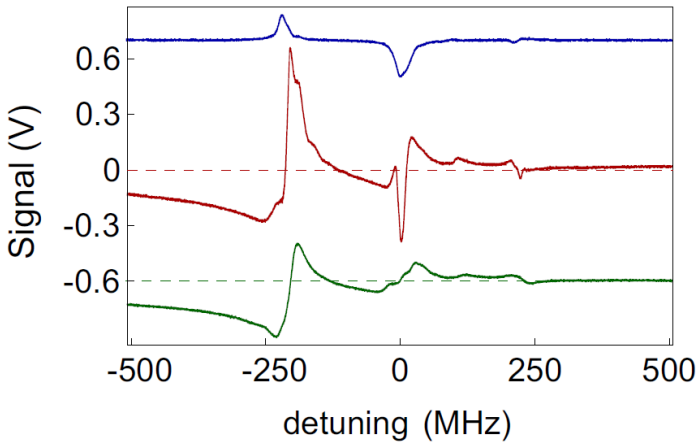

Figure 8.9: Error signals produced by polarisation spectroscopy. (Red) Signal produced using a NPBS in the setup and (Green) signal produced using a gold mirror.

The red error signal in figure 8.9 was produced using the setup shown above. We chose to use a non-polarizing (50:50) beam splitter (NPBS) to combine the pump and probe beam as this would give us perfect overlap. However, the NPBS does not perfectly preserve the polarisation state of the beams and has the potential to distort the signal. To this end we changed the setup slightly and replaced the NPBS with a gold mirror, keeping the rest of the setup the same. The results of this are shown in the green error signal in figure 8.9. Although the gold mirror solves the polarisation problem, for its use it was required that the pump and probe beam cross each other at a small angle in the K-cell, specifically 40 mrad for our setup. This had the effect of increasing the residual Doppler broadening and the smaller effective pump-probe overlap region produced a smaller error signal compared to one obtained with the NPBS. All other setups therefore used the NPBS instead of the gold mirror.

The next modulation free spectroscopy technique we investigated was the magnetically induced dichroism technique [62], [32], [44]. This technique utilises a magnetic field to induce a Zeeman shift in the atomic medium which shifts the positive and negative m_F states in opposite directions. This splitting results in a frequency dependent circular dichroism in the medium. For a Zeeman shift in the order of the absorption line width, a dispersive shape is obtained as first introduced by Corwin *et al* [11]. In a Doppler broadened medium, this has the disadvantage of requiring a very large magnetic field ($\approx 100G$) and the frequency drifts are in the order of a a few MHz. Using a linearly polarised pump beam results in sub-Doppler magnetic dichroism. This has the advantage of requiring a much weaker inducing magnetic field as now the Zeeman shift in the order of the natural linewidth as opposed to the Doppler linewidth. Sub-Doppler magnetic dichroism in this form did not work on our setup and we could not produce satisfactory error signals. The sub-Doppler dispersive features were dominated by a large Doppler broadened background which meant the error signal did not have a zero-crossing. We believe that the large Doppler background of our signal was a result of the polarisation impurities caused by the wave-plates used in our setup.

A solution to this problem was found in the form of using two pairs of spatially separated pump and probe beams. This has the effect of increasing the atomic anisotropy and reducing the Doppler background. Figure 8.10 shows a diagram of the setup used to produce the error signals.

Two different setups of the split beam spectroscopy were studied. The first, which we call Type I has separated $\sigma_{\pm}$ pump beams which increase the dichroism in the medium by pumping atoms into higher m_F states as opposed to a linearly polarised pump which produces a roughly uniform population of m_F states. Each probe beam is of the same polarisation as the corresponding pump resulting in a stronger absorption

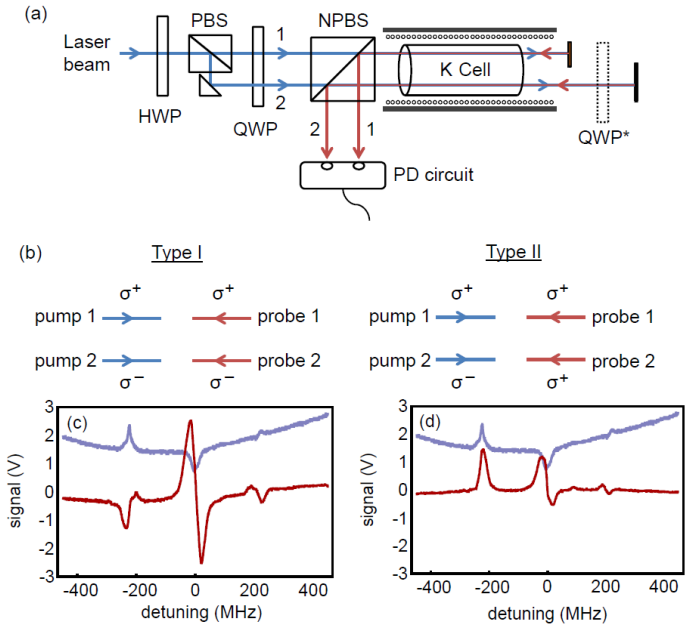

Figure 8.10: (a) Setup used to produce split beam magnetically induced dichroism signals. The dashed quarter-wave plate QWP* is absent in Type I spectroscopy and present in Type II. (b) Comparison of pump and probe polarizations for Type I and II configurations. (c) Type I spectroscopy error signal (d) Type II spectroscopy error signal.

than usual. A background does remain due to the differential Doppler absorption. This background can be reduced by using probe beams of the same polarisation at the expense of an asymmetric dispersion due to the different Clebsch-Gordan coefficients seen by the two probes, this modification to the setup we refer to as Type II.

Comparing the two spectra produced by these techniques we can see that Type II produces only a slightly flatter background but has relatively small dispersive features. In contrast, the Type I configuration produces a larger, more symmetric error signal, especially at the crossover. The relative prominence of the crossover suggests that hyperfine pumping plays a significant role similar to the crossover signal produced by saturated abosorption spectroscopy shown earlier.

8.1.3 Overview of the Laser Locking Scheme for the Experiment

The lasers systems for the experiment can be split in two broad categories. Firstly, the lasers used to generate the MOT, this includes a master laser and two slave lasers. Secondly, the lasers for the ring cavity, which include a Toptica DLpro 852 nm laser for locking the ring cavity and providing the optical potential for the FORT, plus a Toptical DLpro 76 7nm laser for probing the ring cavity. The master laser is locked using one

of the atomic laser locking techniques described in the previous section, specifically the Type I split beam magnetically induced dichroism technique (SBMD). This technique was chosen because it had the largest amplitude as well as having the lock signal at the crossover transition. This allows for easy detuning to the cooling transitions either side of this feature and also as a modulation free method we do away with the need of radio frequency electronics and modulators.

For locking the two slave laser we use the frequency offset lock (FOL) technique [50]. This technique is used to lock the slave lasers with respect to the master laser, figure 8.11 shows a schematic of the laser lock technique.

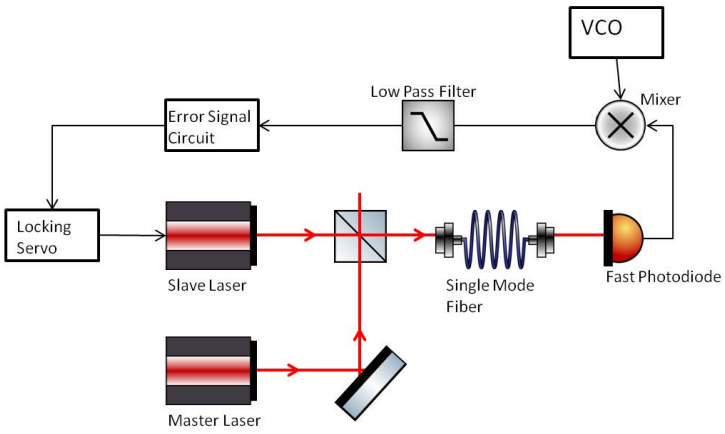

Figure 8.11: Offset lock technique used to stabilise the slave lasers with respect to the master laser.

A beat note is generated between the stabilised master laser and a slave laser by combining the two laser beams into a single mode fiber and detecting the output of the fiber on a fast photodiode (Hamamatsu Photonics, G4176-03). The beat note frequency is given by $\omega_B = \omega_M - \omega_S$, where ω_M and ω_S are the frequencies of the master and slave lasers respectively. The output of the photodiode is fed to a mixer (Minicircuits, ZFM-2+) where it is mixed with a reference signal generated by a voltage controlled oscillator (VCO). The output of the mixer is low pass filtered to extract the low frequency ($\omega_B - \omega_r$) component, where ω_r is the reference signal. This output is fed to an error signal circuit to generate a lock signal to stabilise the slave laser. The frequency of the offset lock can be tuned by changing the reference signal frequency. Both slave lasers are locked to the master using this technique and are ≈200 MHz blue and red detuned from the master laser respectively.

For locking the cavities in the experiment we use the Pound-Drever-Hall (PDH) like technique as described in chapter 5. An overview of the laser locking scheme for the whole experiment is shown in figure 8.12. From

this we can observe that the stability of the lasers and cavities for the experiment are all drawn from the master laser. The master laser is locked with the SBMD technique, then the two slave lasers are offset locked relative to the master. The transfer cavity is locked to the master laser using the PDH like technique and in turn it locks the DLpro 852 nm laser to itself with the PDH like technique. Lastly, the ring cavity is locked to the DLpro 852 nm laser using the PDH like technique.

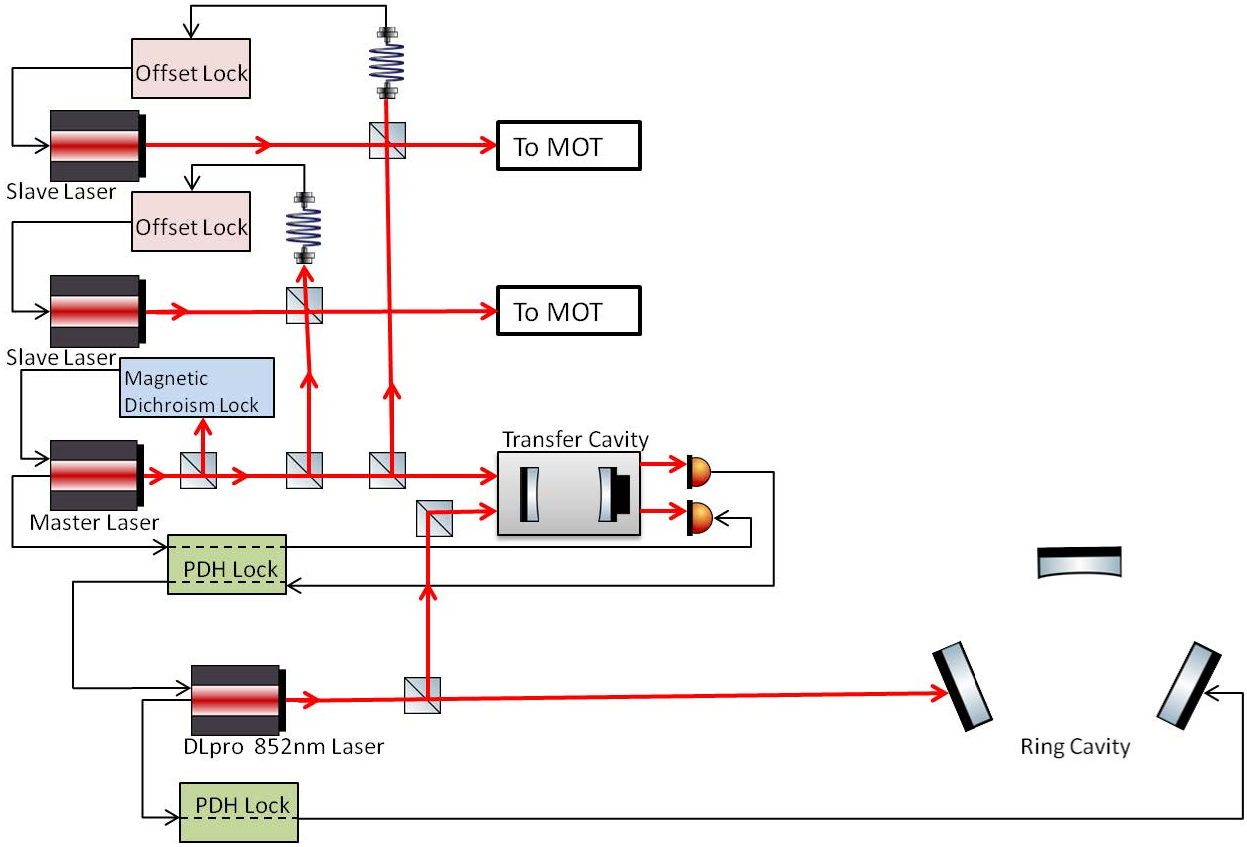

Figure 8.12: Locking scheme for the experiment, the direction of arrows denotes the direction of the lock.

8.2 Magneto-Optical Trapping of Potassium

8.2.1 Laser Cooling and Trapping

Laser cooling as a method to cool atoms was first suggested by Hänsch in the 1980s and the 1997 Nobel prize was awarded to Steven Chu [10] for the first experimental realisation of laser cooling, William D. Phillips for breaking the Doppler limit [45] and Claude Cohen-Tannoudji for the theoretical identification of the process

[15]. The basis of these methods relies on the fact that the interaction of atoms and light can produce forces, namely a scattering force and a dipole force.

The scattering force arises due to momentum transfer between an atom and a photon. When a photon from a laser is absorbed by an atom it acquires a momentum, $\hbar k$, in the direction of the laser beam. In the case of spontaneous emission it is isotropic and hence over many cycles the total momentum change averages to zero. Whereas for the laser, the momentum kick is in the same direction every time and thus add up, resulting in a force felt by the atom. This is known as the scattering force and the magnitude of which is given by

$$F_{sc} = \hbar k \gamma_{sc}, \tag{8.3}$$

where γ_{sc} is the photon scattering rate. For a two-level atom this scattering rate is given by

$$\gamma_{sc} = \gamma \frac{I/I_{sat}}{1 + ((\Delta - \vec{k}.\vec{v})/\gamma)^2 + I/I_{sat}}, \tag{8.4}$$

where Δ is the detuning of the laser from the resonant frequency of the atomic transition. I is the laser intensity and I_{sat} is the saturation intensity. Γ is the inverse of the excited state lifetime. $\vec{k}.\vec{v}$ denotes the Doppler shift of the laser as seen from the atom frame of reference. This Doppler shift forms the basis of laser cooling. For a red detuned beam (from the lab frame of reference) an atom moving towards the beam will be Doppler shifted into resonance and thus scatter more photons and conversely an atom moving along the beam direction is Doppler shifted away from resonance and scatter less photons. Therefore this red detuned beam has overall decelerating effect on the atom, known as 'optical molasses'. Applying red detuned laser beams in all six Cartesian directions results in a decelerating force in all directions, this is known as '3D optical molasses'.

The temperature achievable by this method is reached when the Doppler cooling rate balances with the heating rate of the atom caused by the random recoil kick caused by spontaneous emission of the atom. This is known as Doppler temperature and is given by

$$T_D = \frac{\hbar \gamma}{2k_B}. \tag{8.5}$$

γ for Potassium is 3 MHz, which leads to a Doppler temperature of 145 μK. Although this Doppler force can cool atoms, since it is only velocity dependent it cannot trap atoms. For this, a position dependent potential is also required.

This position dependent potential comes in the form a magnetic field gradient. The combination of optical and magnetic forces for atom trapping and cooling is known as the magneto-optical trap (MOT) [48]. The MOT is the most widely used technique for atom cooling and is used in thousands of labs around the world. For a two level atom with ground state $F = 0$ and excited state $F' = 1$ an anti-Helmholtz pair of magnetic coils produces a magnetic field gradient which splits the Zeeman levels of the excited state into three sub-levels ($m_F = -1, 0, 1$). By interrogating the atom with circularly polarised light the following selection rules apply:

σ_+ polarised light only drives F=0→F'=1,$m_F = 1$ transitions,

σ_- polarised light only drives F=0→F'=1,$m_F = -1$ transitions.

From figure 8.13, an atom in the positive z side of the graph will be preferentially pushed towards the origin as the F=0→F'=1,$m_F = -1$ transition which is closest to laser frequency can only be driven by σ_- polarised light. This, combined with the Doppler cooling effect described above means that the total force of the MOT on an atom is now velocity and position dependent.

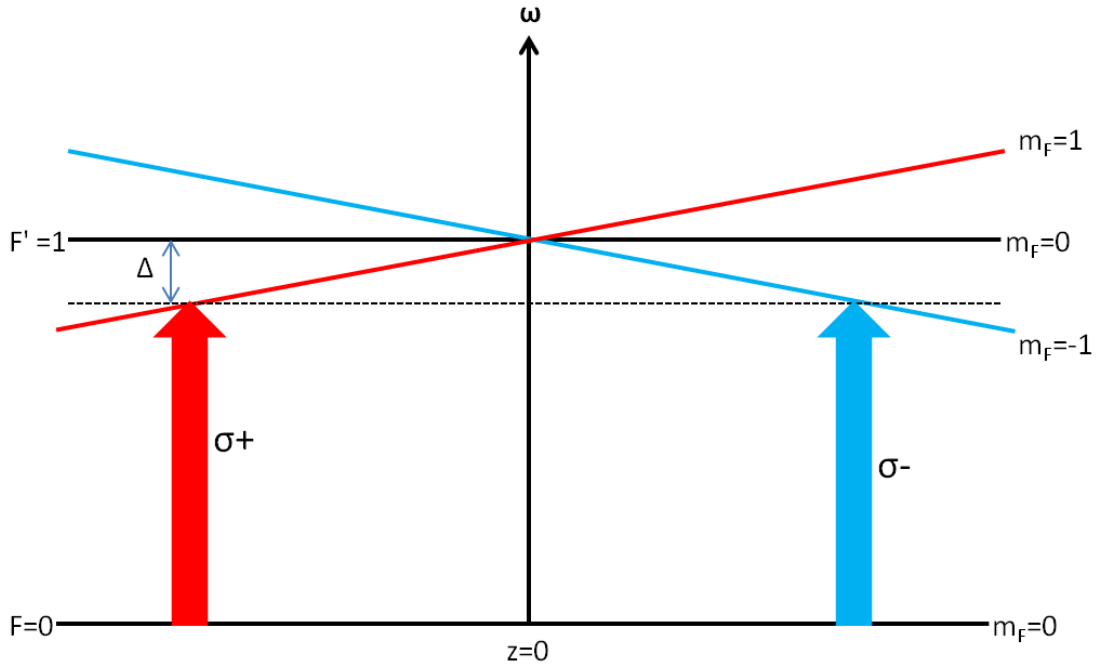

Figure 8.13: Model of the trapping mechanism for a MOT using circularly polarised light and a magnetic field gradient.

8.2.2 Elongated MOT Setup

A conventional 3D MOT produces a roughly spherical cloud of cold atoms at the center of the trap. However, for our experiment as we require an intra-cavity MOT interfaced directly into the cavity mode, we need the maximal number of atoms to be trapped in the cavity mode. This can be achieved by having an elongated MOT to get better overlap with the cavity mode.

For a conventional 3D MOT, the coil used to generate the magnetic field produce a field gradient which is uniform in all directions. For a 2D MOT, which is used to precool atoms before loading them into a 3D MOT there is no trapping potential along the longitudinal axis. Instead, a pushing beam is used to moved the precooled atoms into the 3D MOT. For our 3D MOT we exploit this feature of the 2D MOT to create an elongated MOT [53]. To compensate for not having a trapping potential in the longitudinal axis the two pairs of laser beams in this axis do not follow the symmetry axes of the magnetic field. They are instead aligned 45° to the longitudinal axis as shown in figure 8.14 to provide an optical force confining the atoms in this axis. This also has the added benefit that since there is no MOT beam in the longitudinal axis it is possible to probe the cavity along this axis.

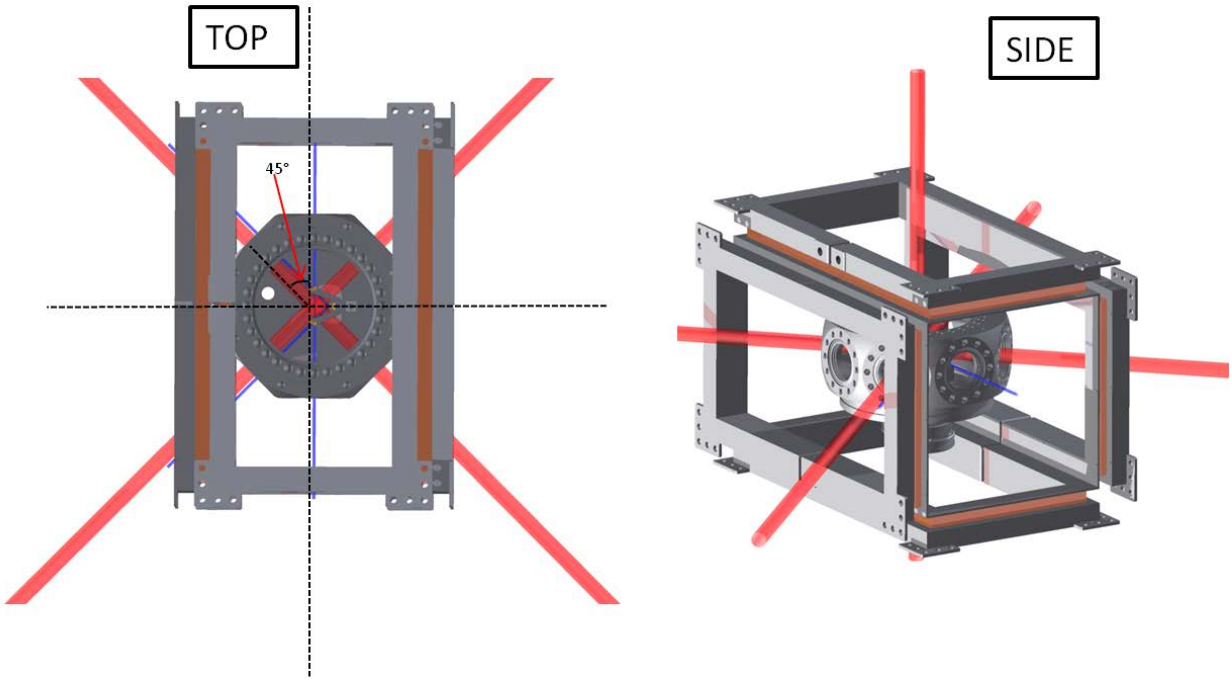

Figure 8.14: 3D MOT coil setup for creating an elongated MOT. Red beams are for the MOT and blue beams are for the cavity.

The geometry for the coil system is also shown in figure 8.14. We use two pairs of rectangular shaped

coils in a cage structure to generate a 2D quadruple magnetic field. There are copper frames housing the coils with hollowed cores to allow for water cooling of the coils. The coils themselves are wound from kapton insulated copper strips of 14 mm by 0.25 mm dimensions. Each frame has forty turns of the copper wound around it and the current density, J, of each coil can be calculated by using the equation,

$$J = \frac{IN}{A}, \tag{8.6}$$

where where A is the cross-sectional area of the rectangular coil and N is the number of turns around the coil and comes to 8.6 A/mm^2. A small slit is present in each coil frame to prevent eddy currents. All four coils are wired in series and powered by a linear power supply supply, (Statron Geratetechnik: 3257.1, 0-36V/0-40A). A picture of the fully assembled coil system is shown in figure 8.15

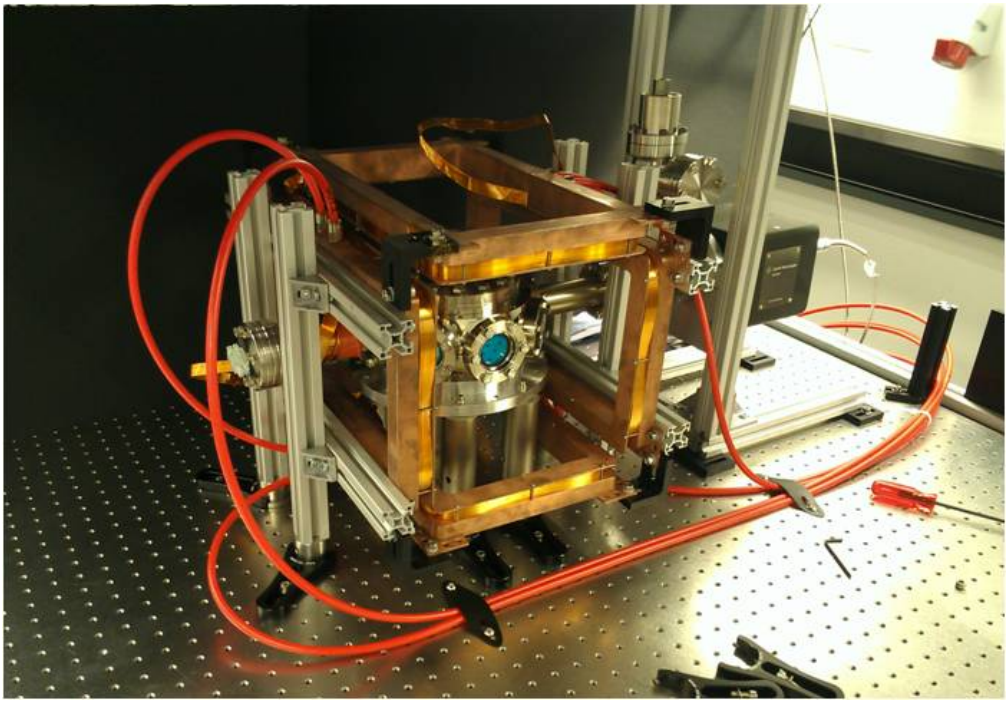

Figure 8.15: Fully assembled coil system to generate the magnetic field for the MOT with the water cooling system installed.

8.2.3 Observation of Intra-cavity MOT

For cooling Potassium we drive the atoms near the F=2→F'=3 transition of the D2 line. This is the cycling transition for Potassium and one of the slave lasers described earlier is detuned 8.221 MHz from this transition

and acts as the cooling laser. A second laser is also required to maintain the atomic population of the cooling transition. This is done by pumping near the F=1→F'=2 transition, the second slave laser is detuned 2.06 MHz from this transition and acts as the repumper laser. Figure 8.16 shows the level structure for the cooling and repump transitions. Due to the small excited state hyperfine splitting of Potassium the atoms

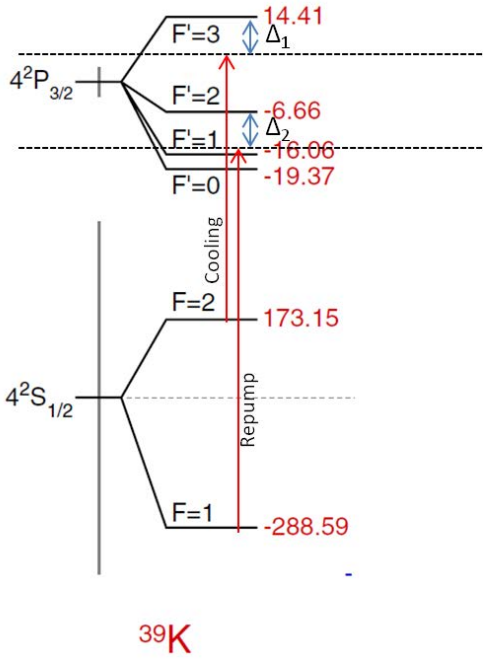

Figure 8.16: The energy level diagram for ^{39}K D2 transitions where the cooling and repump transitions are highlighted, Δ_1 is the detuning of the cooling beam and Δ_2 is the detuning of the repump beam. Units are in MHz detuning from the fine structure transition.

more easily decouple from the cycling transition into the other excited states as compared to other alkali atoms. Therefore, the optical repumping required is large. For our system we operate with a ratio of cooling and repump light of ≈1:1. A total power of 75 mW in both the trapping and repump laser is used to create the MOT. The beams have a diameter of 7.5 mm and each pair of beams is circularly polarised with opposite polarity.

Figure 8.17 shows an image of the intracavity Potassium MOT captured by a CCD camera (Allied vision technologies Pike F-145). The light scattered from the MOT can be used to calculate the number of atoms in the MOT and its density, which can subsequently be used to calculate the number of atoms coupled to the cavity mode. To image the MOT we use fluorescence imaging. For this, light scattered from the MOT has to be collected on a CCD camera. We use a single convex-convex lens with a focal length of 75 mm between the MOT and the camera. Our geometry did not allow for a line of sight positioning between the MOT and

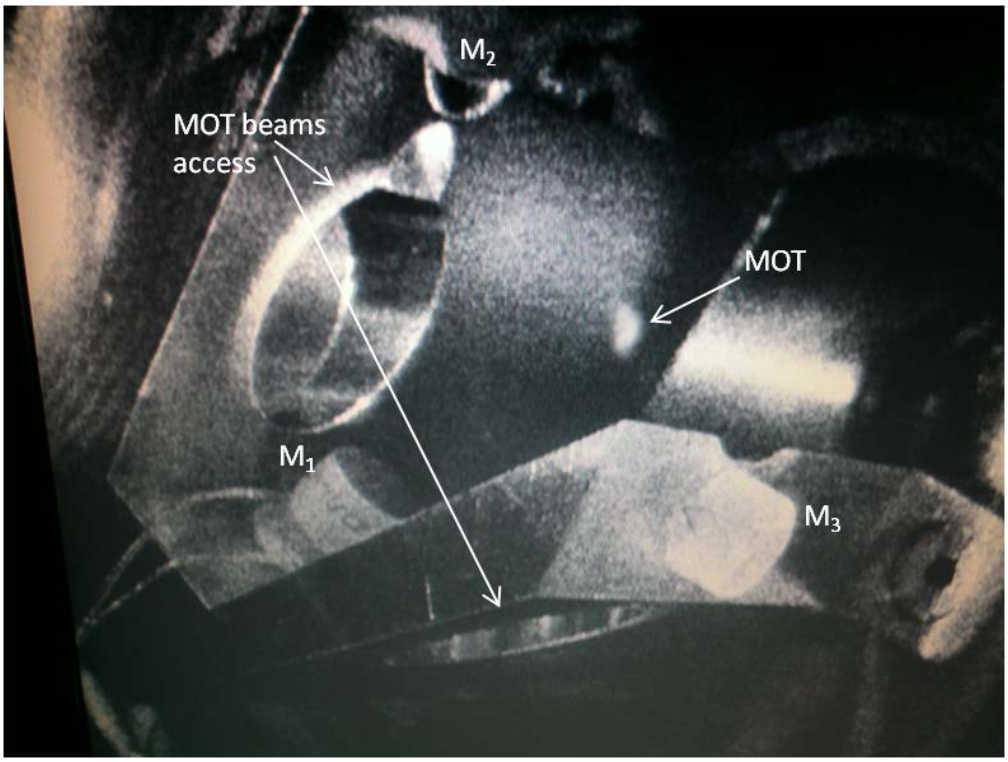

Figure 8.17: The intra-cavity MOT.

the camera so therefore a mirror is used redirect the path of the fluorescence. The thin lens formula is used to determine the position of the camera and lens with respect to the MOT and is given by

$$\frac{1}{f} = \frac{1}{u} + \frac{1}{v}, \tag{8.7}$$

where f is the focal length of the lens, u is the distance from the MOT to the lens and v is the distance from the lens to the camera. The spatial dimension of the CCD camera are about the same order as the size of the MOT. To get good coverage of the MOT it was necessary to demagnify the image of the MOT onto the camera surface. f, u and v were chosen to give a demagnification of $\approx$2. For a lens of focal length 75 mm a demagnification of two can be achieved by setting $u/v = 2$. In our system we have these set to as $u = 225 \pm 20\ mm$ and $v = 112 \pm 20\ mm$ giving a demagnification, $d = 2.00 \pm 0.5$. To image the MOT, pictures are taken with and without the MOT to subtract the background noise. The subtracted image is fitted to a 2D Gaussian function as shown in figure 8.18 which gives the rms widths of the MOT along the y and z axis. Assuming the MOT is symmetrical along the x-y plane we get the following rms witdths of the MOT

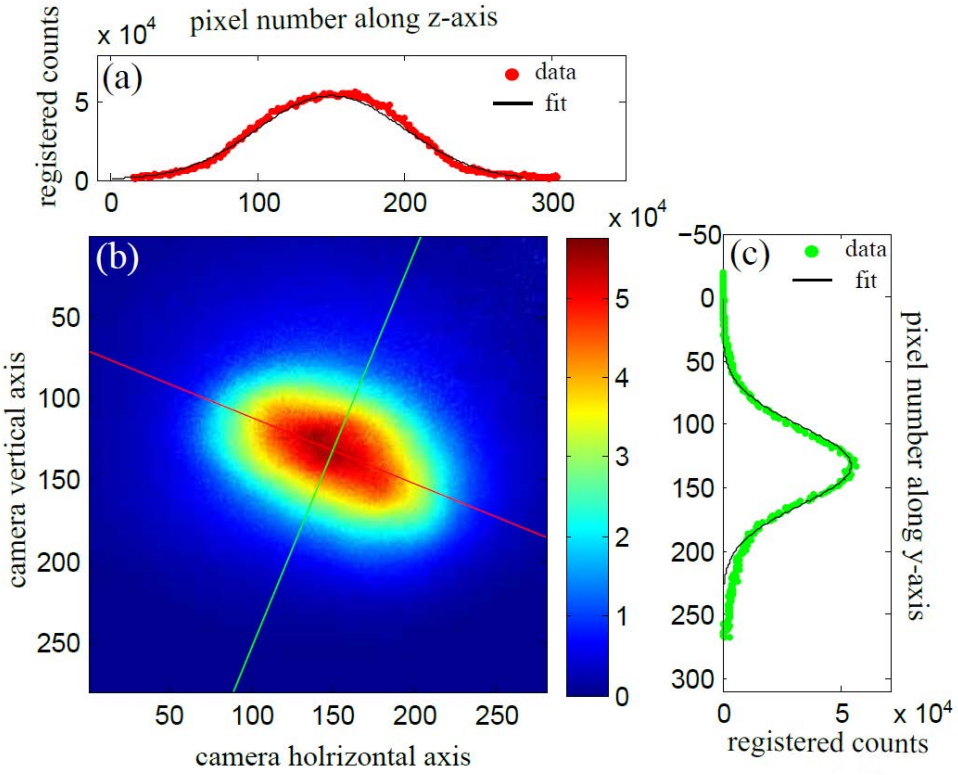

Figure 8.18: The 2D Gaussian fit of the MOT.

$$\sigma_x = 0.31\ mm,$$

$$\sigma_y = 0.31\ mm,$$

$$\sigma_z = 0.52\ mm.$$

From this, we can see that the MOT is slightly elongated in the z-direction. However, this is much less elongation that we were expecting, which we believe may be due the size of the MOT beams not being big enough or the capture velocity of the MOT being too low at the extremities of the MOT.

To calculate the number of atoms in the MOT, we measure the power of the light emitted by the fluorescing atoms. This power is proportional to the excited state fraction of the atoms in the MOT and is given by

$$P_{MOT} = \gamma_{sc} N_{MOT} E, \tag{8.8}$$

where N_{MOT} is the atom number and E is the energy of each photon. As the MOT radiates light in all directions, only a small fraction is incident on the CCD. This fractional solid angle $d\Omega$ can be calculated

using,

$$d\Omega = \frac{\pi r^2}{4\pi u^2}, \tag{8.9}$$

where r is the radius of the imaging lens. For our system we get a $d\Omega$ value of 7.96×10^{-4}. The number of photons collected by the camera over an exposure time τ is given by

$$N_{CCD} = N_{MOT} d\Omega \tau \gamma_{sc}. \tag{8.10}$$

The number of photons collected by the camera is inferred from the total number of registered pixel counts on the camera and is given by

$$N_{CCD} = \frac{N_{counts}}{\eta}, \tag{8.11}$$

where η is the quantum efficiency of the camera. This was calculated by calibrating the camera with a weak laser beam of known power and recording the count rate as the power is varied, it came to $\approx 2.17 \times 10^{-3}$ *counts/photon*. With this, the following expression can be used to calculate the atom number,

$$N_{MOT} = \frac{N_{counts}}{d\Omega \tau \gamma_{sc} \eta}. \tag{8.12}$$

The scattering rate γ_{sc} has to be modified to take into account the presence of the repumper beam. As described earlier, the small hyperfine splitting of Potassium requires us to use a cooling repump ratio of 1:1. This has the effect that the repumper contributes to the excited state populations. Taking this into account, we estimate that for our system we have a scattering rate of $0.2727\gamma_{sc}$. With this, we calculate that we have an atom number of

$$N_{MOT} = 3.18 \times 10^7.$$

CHAPTER 9

LIGHT IN THE CAVITY

9.1 Reduced Dipole Matrix Element

From chapter 6, it was seen that resonance had been achieved and light had been coupled into the cavity mode. This chapter looks at the initial results of getting light into the cavity and progress towards strong coupling. As shown previously, the equation for the Rabi frequency is given by

$$g = \sqrt{\frac{\mu^2 \omega_c}{2\hbar\epsilon_0 V}}. \tag{9.1}$$

V is a function of the cavity parameters and was calculated in chapter earlier. μ is the reduced dipole matrix element. The dipole matrix element is a measure of the transition strength of an atom driven by nearly resonant optical beam. For our system, we are interrogating the D2 transition of Potassium ($^2S_{1/2} \rightarrow^2 P_{3/2}$). This dipole matrix element is given by $\langle F m_F \left| e\mathbf{r} \right| F' m'_F \rangle$ where $|F m_F\rangle$ and $|F' m'_F\rangle$ are the hyperfine sublevels under interrogation by the optical beam. e is the electronic charge and $\mathbf{r}$ is the position operator. To calculate the matrix elements, it is useful to represent this equation as a product of a reduced dipole matrix element and Clebsch-Gordan coefficients using Wigner-Eckart theorem [6] as shown in the following equation

$$\langle F m_F \left| e r_q \right| F' m'_F \rangle = \langle F \left|\left| e\mathbf{r} \right|\right| F' \rangle \langle F m_F \left| F' 1 m'_F q \right\rangle, \tag{9.2}$$

where q is the label of the polarisation component on $\mathbf{r}$ and has values $q = \pm 1$ for $\sigma^{\pm}$ polarised transitions and $q = 0$ for π transitions. This equation can be rewritten in terms of Wigner 3-j symbols in the form

$$\langle Fm_F \left| er_q \right| F'm'_F \rangle = \langle F \left|\left| e\mathbf{r} \right|\right| F' \rangle (-1)^{F'-1+m_F} \sqrt{2F+1} \begin{pmatrix} F' & 1 & F \\ m'_F & q & -m_F \end{pmatrix}. \tag{9.3}$$

This reduced matrix element can simplified further by using the Wigner 6-j symbols to factor out the F and F' dependence and has the form

$$\langle J \left|\left| e\mathbf{r} \right|\right| J' \rangle = \langle F \left|\left| e\mathbf{r} \right|\right| F' \rangle (-1)^{F'+J+1+I} \sqrt{(2F'+1)+(2J+1)} \begin{Bmatrix} J & J' & 1 \\ F' & F & 1 \end{Bmatrix}. \tag{9.4}$$

Another Wigner 6-j symbol further simplifies the reduced matrix element to involve only the L quantum number as shown in this expression,

$$\langle J \left|\left| e\mathbf{r} \right|\right| J' \rangle = \langle L \left|\left| e\mathbf{r} \right|\right| L' \rangle (-1)^{J'+L+1+S} \sqrt{(2J'+1)+(2L+1)} \begin{Bmatrix} L & L' & 1 \\ J' & J & 1 \end{Bmatrix}. \tag{9.5}$$

For the D2 transtion of Potassium the reduced dipole matrix element has the form $\langle J = 1/2 \left|\left| e\mathbf{r} \right|\right| J' = 3/2 \rangle$. A numerical value for the reduced dipole matrix element can be calculated from the lifetime of the transition using the following expression.

$$\frac{1}{\tau} = \frac{\omega_0^3}{3\pi\epsilon_0\hbar c^3} \frac{2J+1}{2J'+1} \left| \langle J \left|\left| e\mathbf{r} \right|\right| J' \rangle \right|^2, \tag{9.6}$$

where τ is the measured lifetime of the D2 transition and has a value of 25.8 ns. Rearranging equation 9.6 and inputing the value of τ we get $\langle J = 1/2 \left|\left| e\mathbf{r} \right|\right| J' = 3/2 \rangle = 2.48 \times 10^{-29}\ Cm$, which is given in units of Coulomb meters. This reduced matrix element is μ defined earlier in equation 9.1. This value of μ is averaged over the whole transition from F=2 to F'=3 of the D2 line. However, in our case we are probing the individual transitions of the m_F sub-levels. The strengths of the m_F transitions are expressed as fractions of the total reduced dipole matrix element. Figure 9.1 shows the relative strengths of the m_F transitions in units of μ.

The probe light for the ring cavity has linear s polarisation, so therefore can only excite π transitions[1], specifically the $m_F = 0 \rightarrow m_F = 0'$ transition. This transition has a value of $\frac{3}{5}\mu$. Substituting this value of the effective μ back into equation 9.1 we get a value of the Rabi frequency, $g = 2\pi \times 101.2$ kHz.

[1] Assuming the spin quantisation axis is along the cavity axis

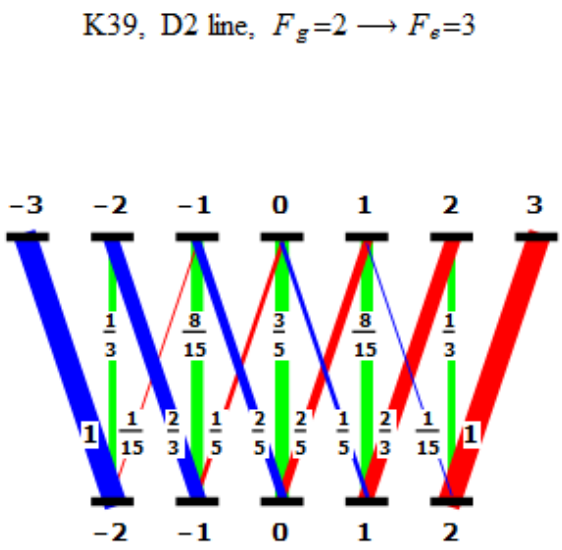

Figure 9.1: The relative strength of the m_F transitions for the D2 $F = 2 \rightarrow F' = 3$ transition of Potassium in units of μ. Greens are π transitions, blue are σ_- and red are σ_+.

9.2 Observation of Cavity Peaks

As shown in chapter 6, the cavity was successfully aligned and resonance was achieved. Photodiode signals of the transmission peaks through the cavity were taken and shown below in figure 9.2. The HWHM linewidth of the cavity is measured and comes to

$\kappa_{767nm} = 2.2 \pm 0.2$ MHz

With this is also possible to get an estimate of the Finesse of the cavity using the relation

$$Finesse = \frac{FSR}{Linewidth}. \tag{9.7}$$

The FSR of the cavity is 4.4 GHz, therefore using the above equation we can calculate that we have an estimated Finesse of 636±40. The measured linewidth is larger and estimated Finesse smaller than the calculated values in chapter 6. This is likely due to contamination of the mirror surfaces from the Potassium vapour in the chamber.

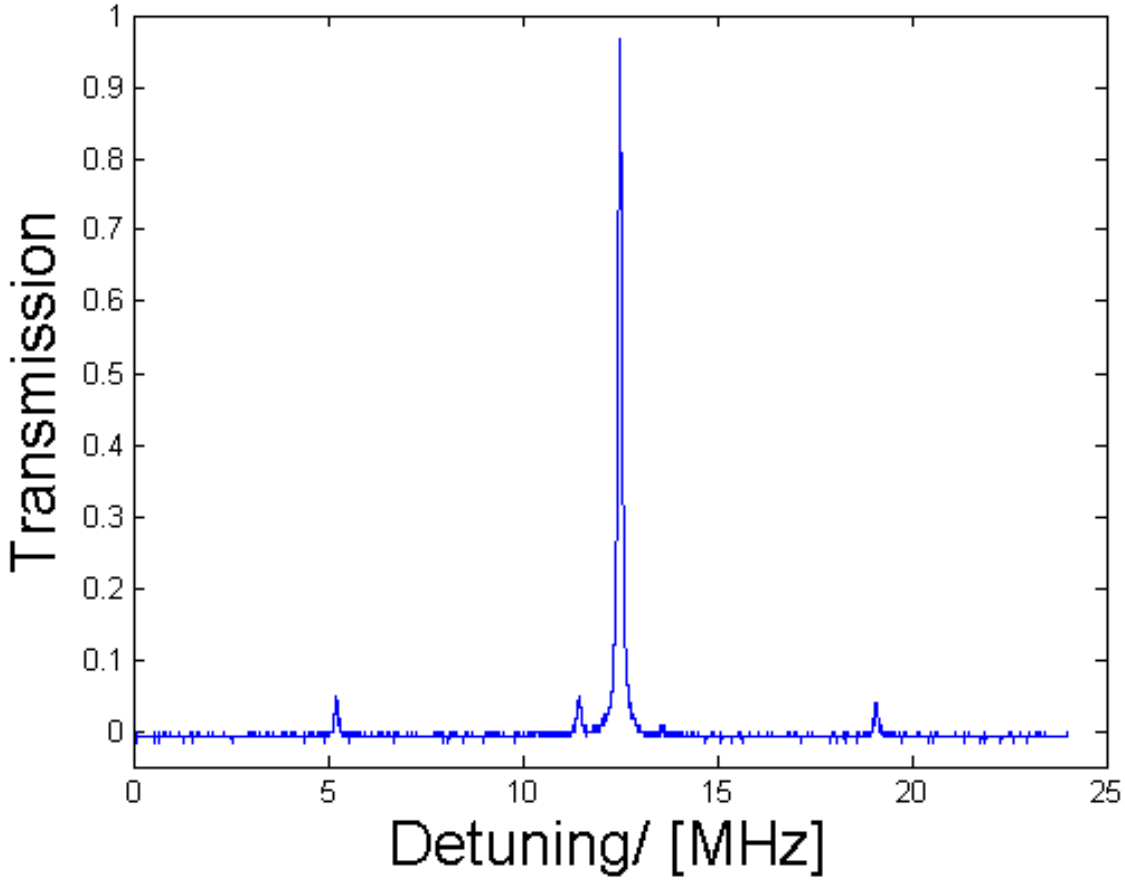

Figure 9.2: Transmission peak through the ring cavity.

9.3 Atoms in the Cavity Mode

In order to achieve strong coupling, it is necessary to trap atoms in the cavity mode from the MOT. In the previous chapter an intra-cavity MOT was achieved and the size of the MOT, number of atoms in the MOT and the atom density were calculated. With this, it is possible to calculate what fraction of the MOT is coincident with the cavity mode and therefore how many atoms are trapped in the cavity mode. The number of atoms in the cavity mode, N_{eff} can be calculated from the equation

$$N_{eff} = \int n(x,y,z)\frac{I(x,y,z)}{I_0}dV, \tag{9.8}$$

where $n(x,y,z)$ is the density of the MOT and $I(x,y,z)/I_0$ is the normalised intensity of the cavity mode. These terms can be broken down to give

$$n(x,y,z) = n_0 e^{-\frac{1}{2}(\frac{x^2}{\sigma_x^2}+\frac{y^2}{\sigma_y^2}+\frac{z^2}{\sigma_z^2})}, \tag{9.9}$$

where n_0 is the peak density of the MOT and $\sigma_{x,y,z}$ represent the rms widths of the MOT. The cavity mode intensity can be given as

$$I_{x,y} = I_0 e^{-2[(\frac{x}{\omega x})^2+(\frac{y}{\omega y})^2]}, \tag{9.10}$$

where I_0 is the peak intensity of the cavity mode. Equation 9.8 can be integrated to give,

$$N_{eff} = \frac{N_{MOT}\omega_x\omega_y}{\sqrt{(4\sigma_x^2+\omega_x^2)(4\sigma_y^2+\omega_y^2)}}. \tag{9.11}$$

For our MOT of dimensions $\sigma_x = 0.31\ mm$ and $\sigma_y = 0.31\ mm$ we get a value of N_{eff} given by

$$N_{eff} = 0.03 N_{MOT}. \tag{9.12}$$

To observe strong coupling in our system, as shown earlier we must operate in the collective strong coupling regime characterised by the equation,

$$g_{coll} = \sqrt{N_{eff}}g. \tag{9.13}$$

We have a calculated g of $2\pi \times 100$ kHz and for strong coupling $g \gg (\gamma, \kappa)$, γ and κ have values $2\pi \times 3$ MHz and $2\pi \times 1$ MHz respectively. From this, we can see that we need on the order of 10^3 atoms in the cavity mode to observe strong coupling. Therefore, from equation 9.12 we can calculate that we need a MOT of $\approx 3.3 \times 10^4$ atoms in order to observe strong coupling. This is entirely feasible as the MOTs produced in this experiment are typically in the 10^7 atom number region.

9.4 New Cavity Mirrors

After observing the transmission peaks through the cavity, attempts were made to observe the vacuum Rabi splitting in the cavity. This was done by forming a MOT, sending 767 nm probe light locked to the D2 transition and scanning the cavity mode with a piezo. Figure 9.3 shows the input/output direction of the probe laser through the cavity to a sensitive photodiode (Laser Components, LCSA500-03).

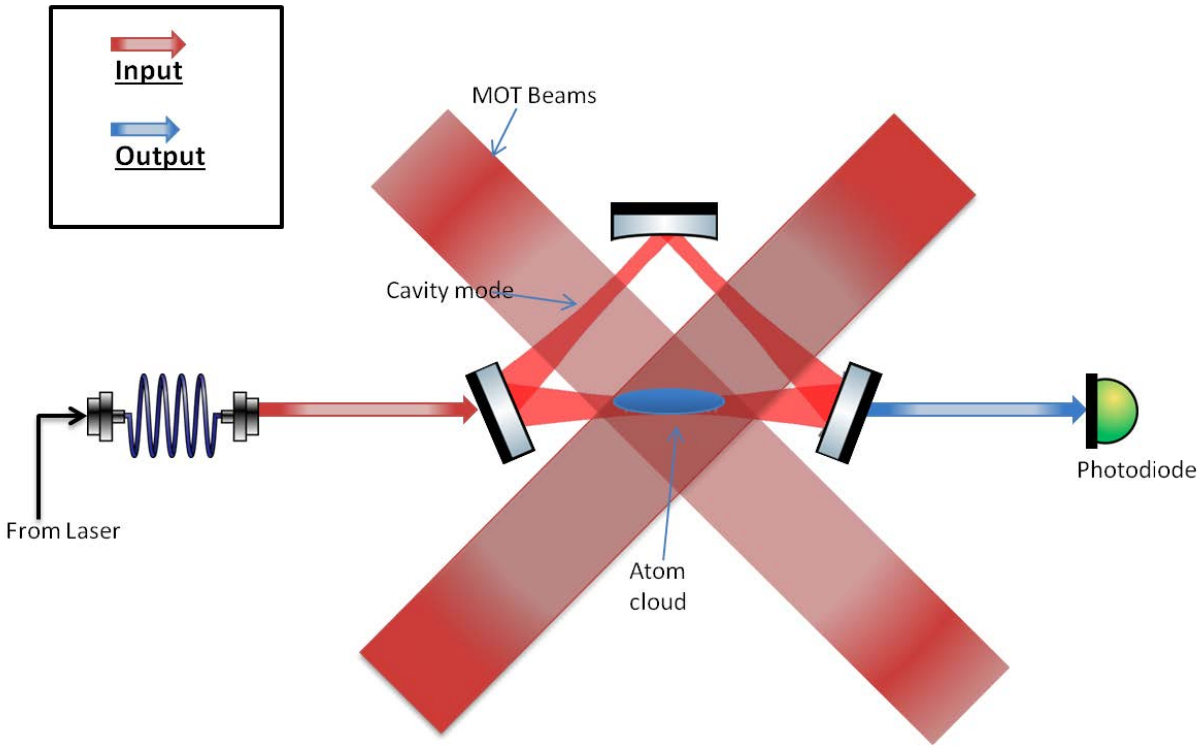

Figure 9.3: Input/output direction of the probe laser.

However, we discovered that we had an issue with the atomic source where Potassium was coating the mirror surfaces and heavily compromising the Finesse of the cavity. The linewidth of the cavity increased to 100s of MHz, making observation of Rabi splitting impossible. Attempts were made to remove the Potassium by heating the vacuum chamber and also using intense UV light aimed at the mirror surfaces, however this did not work.

The cavity was removed from vacuum and attempts were made to clean the mirrors. Ultimately a new set of mirrors had to be installed as shown in figure 9.4. The new mirror set used have the following power reflectivities

$M_1 = 99.96\%$,

$M_2 = 99.0\%$,

$M_3 = 99.0\%$.

The mirror M_1 is the central mirror used for piezo actuation and is the exact same mirror as before. Mirrors M_2 and M_3 are new mirrors. M_2 is a flat mirror and M_3 is a curved mirror with a radius of curvature of 5 cm. They are larger in size than the 6.35 mm mirrors used before with a size of 12.7 mm. However, they do not impede the MOT beams. These mirrors serve as the new input/output couplers. The new cavity was

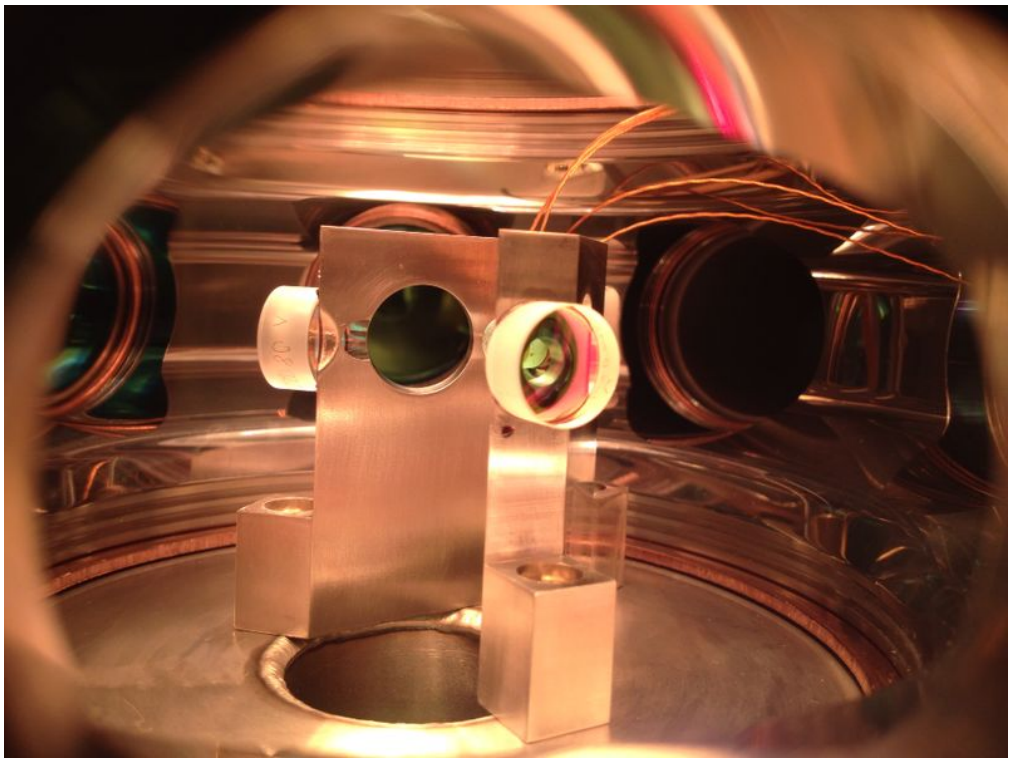

Figure 9.4: The cavity with replaced input/output coupler mirrors.

characterised and found to have the following parameters.

Linewidth= 7.16 MHz,

Finesse= 306.5,

Tangential waist= 39.44 μm,

Sagittal waist= 92.85 μm,

Mode volume = 39.3 mm^3,

Rabi frequency =$2\pi \times$ 120.85 kHz.

An accurate datasheet with the reflectivities of the new mirrors could not be found, so these numbers represent the lower case limit of the given parameters.

9.5 Preliminary Observation of Rabi Splitting

Care was taken when reassembling the vacuum system to minimise the contact of the mirrors with the atomic source. The experimental procedure for observing Rabi splitting was repeated and eventually the first observation of Rabi splitting was achieved, as shown in figure 9.5 Preliminary analysis gives a cavity

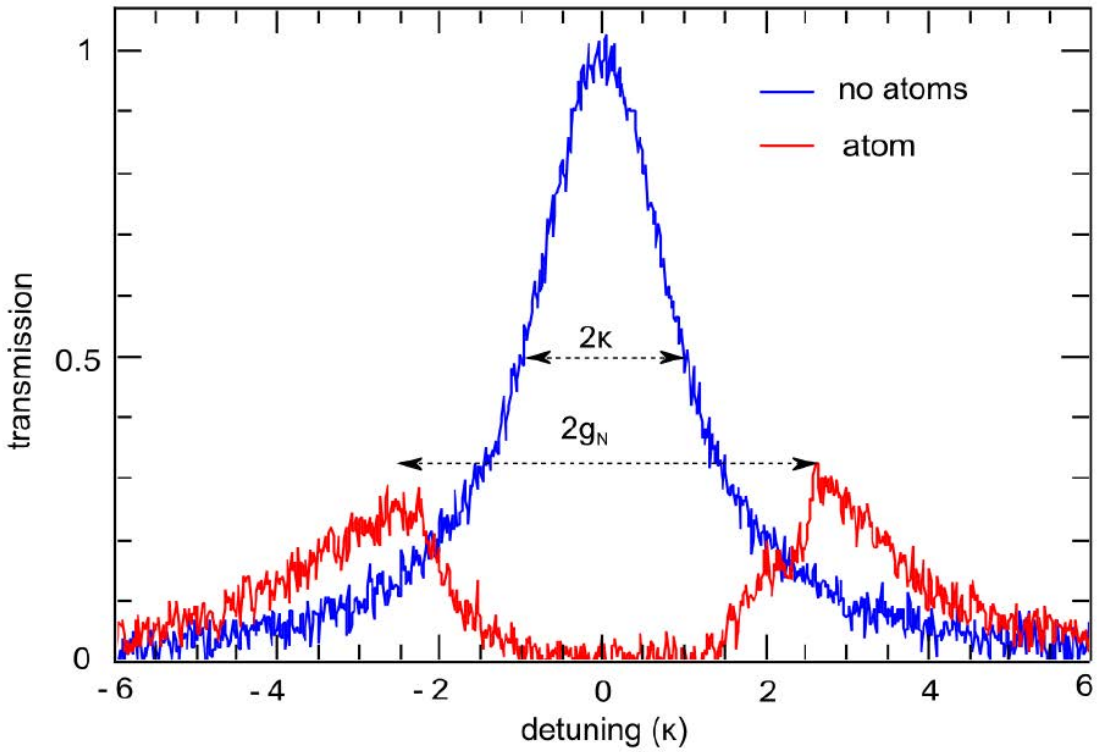

Figure 9.5: First observation of Rabi splitting

HWHM linewidth of ≈8 MHz and a Rabi splitting of ≈20 MHz. From this we can calculate that we have $N_{eff} = 6400$. The broadened linewidth shows that the original problem of Potassium coating the mirror surfaces and compromising the Finesse has not been solved. Further contamination of the cavity mirrors prevented more readings to be taken. As of writing, a new cavity is being designed and a 2D MOT chamber is to be added to the experiment to limit the amount of direct Potassium that the cavity mirrors see.

CHAPTER 10

OUTLOOK

This thesis presented the design and construction of a ring cavity experiment to study cold Potassium atoms in the collective strong coupling regime. The focus of this thesis was on the design and development of the optical cavities used for the experiment. The development of this project was roughly split into two sections. The first was the development of the laser systems needed to generate a MOT and interrogate the ring cavity. We had custom built ECDLs and commercial Toptical DLpro lasers for this purpose. We carried out a detailed study of methods to stabilise these lasers. Firstly, methods to stabilise the master laser for the experiment. We studied atomic spectroscopic techniques for the D2 line of Potassium 39. Firstly, modulation based methods, direct modulation and modulation transfer spectroscopy. Secondly, modulation free methods, polarisation spectroscopy and magnetic dichroism spectroscopy. Ultimately we chose the magnetic dichroism spectroscopy. As it is modulation free, we do away with the need for RF components and modulators and it also produced the largest amplitude signal for locking. This was at the crossover transition, allowing for easy detuning to the cooling and repump transitions required for the MOT.

Concurrently, we also studied methods to transfer the stability of the master laser lock to off-resonant lasers. These would be used to stabilise and serve as a trapping potential for the ring cavity. This came in the form of a transfer cavity. The transfer cavity was designed and constructed. We investigated generalisations of the confocal cavity by changing the length of the cavity to positions with rational Gouy phases. Numerous of these positions were found enabling us to subdivide the mode spacing of the cavity to up to a tenth of the FSR. This enables us to overcome the large detuning requirements when locking to cavitites with large mode spacings. We investigated methods of stabilising the transfer cavity in the form of the Hänsch-Couillard and a Pound-Drever-Hall like spectroscopy. Ultimately we chose the PDH like method as HC suffered alignment problems when changing the length of the cavity due to the Brewster window steering the beam, also the

Brewster window degraded the Finesse of the cavity. For PDH like spectroscopy we had the advantage that if the modulation frequency is set to half the mode spacing an additional error signal suitable for locking is produced. So for a mode spacing of 42 MHz, a modulation at 21 MHz would produce error signals every 21 MHz, a manageable amount of detuning for a AOM.

The second stage of development for the experiment was the design and construction of the ring cavity, vacuum system and magnetic coil system. The ring cavity was designed and constructed to have a κ of $2\pi \times 1$ MHz and g of $2\pi \times 100$ kHz. The atoms have a γ of $2\pi \times 3$ MHz. In order to reach the collective strong coupling regime we required to have at least 10^3 atoms in the cavity mode. Other parameters of the ring cavity were characterised including the mode volume, which had differing mode waist components due to the natural astigmatism that arises in ring cavity. An abberation balancing lens system was setup to provide mode matching for the input/output light coupled to the cavity. Lastly, the impedance matching of the cavity was characterised and mirror coatings were designed to maximise it for both 767 nm and 852 nm light. The vacuum system was designed and constructed. It had a custom bottom flange to house the ring cavity and its electrical feedthrough. The magnetic coil system was designed to produce an elongated MOT to allow for maximal overlap of the MOT and cavity mode. This involved adapting a 2D MOT setup with no trapping in the z-axis to elongate the MOT and then orienting the MOT beams 45° to the longitudinal axis to provide an optical force to confine the atoms in that axis.

The experiment was ran and a MOT was achieved. When trying to observe the atom-photon interactions through cavity transmission, we found that Potassium atoms had coated the mirror surfaces degrading the Finesse of the cavity. Attempts to remove the contamination by heating the chamber and illuminating the mirrors with UV light yielded no success. Ultimately, we had to replace the two input/output coupler mirrors. With the new cavity we were able to observe collective strong coupling for our system. We observed a Rabi-splitting of ≈20 MHz for a cavity linewidth of ≈8 MHz, this suggests that we have a $N_{eff} = 6400$. Further readings were compromised by the Potassium coating problem we encountered earlier.

10.1 Looking Forward

The next stage for the experiment involves a redesign of the system to eliminate the Potassium coating problem. The first step consists of attaching a 2D MOT to the system to precool the atoms before they enter the main chamber. This greatly reduces the pressure of background atoms to potentially degrade the mirrors. We will use a pushing beam to direct the precooled atoms in the 2D MOT through a narrow nipple aimed at the cavity mode center. This way atoms should only be passing through the cavity mode to be

either, trapped in the MOT, straight through to be pumped out of the system or stick to the chamber walls. The second stage is a redesign of the ring cavity itself as shown in figure 10.1. A few notable changes from

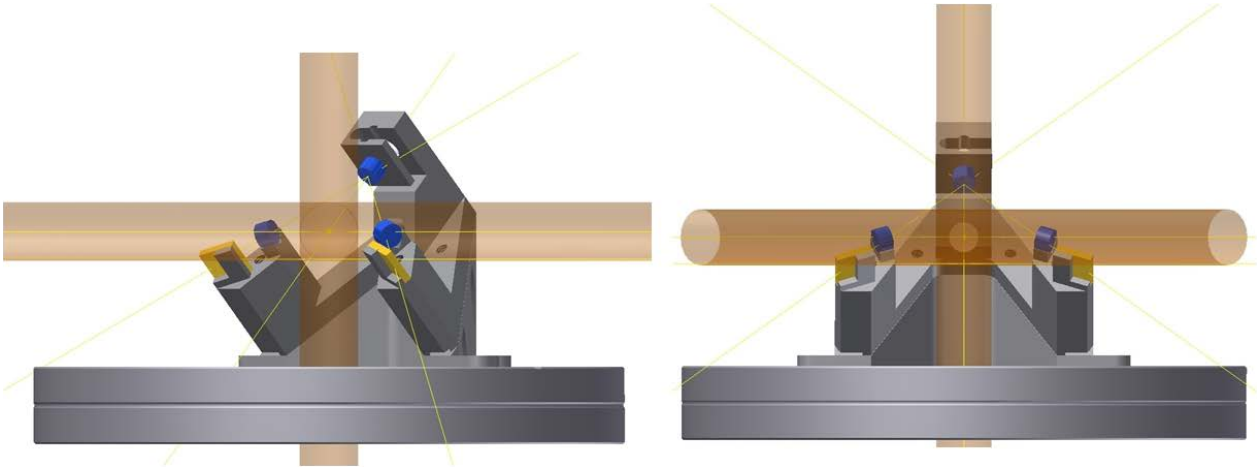

Figure 10.1: CAD design of the new ring cavity.

the old design, the curved mirror is no longer glued directly to the piezo and the piezo now sits behind a flexmount were the mirror is held. The orientation of the cavity has been changed so none of the mirrors are in the direct beam path of the precooled atoms. The input/output coupler mirrors are held in a u-groove so more of the mirror is exposed and beam paths are not blocked by the metal surface. A new 3D coil setup is also currently under consideration, with the prospect of making the MOT more elongated.

Once the new setup is completed and capable of reaching the strong coupling regime, we will begin investigations into creating a bi-directional superradiant cold atom laser. If the group index is made large, corresponding to a very small group velocity, the laser can be made extremely insensitive to mechanical and thermal noise in the laser cavity. Such a laser can operate as an active optical clock, which would combine the high quality factor of optical lattice clocks with immunity from environmental perturbations.

We will use the cold atoms as a gain medium, tuning the group index through Electromagnetically-Induced-Transparency. EIT is a phenomenon observable in a three-level system that reduces the absorption of a medium. It can be described as an optical pumping into a coherent superposition of two ground states when two laser sources are tuned to a common exited state. The linewidth of the EIT signal is very narrow hence its usefulness in atomic clock and metrology applications. We have identified the Raman lasing scheme developed by the Thompson group at JILA (Boulder, Colorado, USA) and the four-wave mixing scheme demonstrated by the Kaiser group (Nice, France) as promising candidates for this work.

APPENDIX A

OCTAVE CODE FOR FITTING MULTIPLE CAVITY PEAKS

During the study of the Gouy degenerate transfer cavity used to produce multiple closely spaced resonance peaks suitable for generating lock signals, it was necessary to characterise these peaks by fitting them with a Lorentzian function. Fitting a single peak is trivial enough however for multiple peaks all on the same graph this process can become tedious. A solution to this problem was developed in the form of an Octave code which took a single trace with multiple peaks and fitted them all simultaneously and provided fitting parameters for each peak.

A.1 Fitting Lorentzians onto Multiple Cavity Peaks

This code works by using a least square fit algorithm to fit a Lorentzian function, specifically the "leasqr" Octave function. The Lorentzian function used has the form

$$y = Y_0 + \frac{2a}{\pi}\frac{\omega}{(4(x-x_0)^2+\omega^2)}, \tag{A.1}$$

where Y_0 is the offset in the y-axis, a is the area of the peak, ω is the linewidth and x_0 is the center position of the peak. The algorithm is implemented in the form

[yfit,pfit,cvg,iter,corp,covp,covr,stdresid,Z,r2]=leasqr(x,y,p,"ffun",stol,niter).

The parameter of note here are x, y, which are the observed variables from the data to be fit, p holds the initial parameters to be used as guesses for the algorithm, *stol* is the tolerance for the algorithm and *niter* sets the maximum number of iterations to be computed. On the other side $yfit$ is the column vector of computed values, $pfit$ is the column vector of the trial parameters which eventually become the solution.

corp is the correlation matrix for the parameters, *covr* is the covariance matrix of the parameters and *covr* is the covariance matrix of the residuals.

As well as being able to fit multiple lorentzians at once, because it also records the center positions of the peaks, it is also possible to measure the mode spacing. This was especially useful for testing generalisations of the Gouy degenarate cavity where we needed to know for a particular cavity length what the mode spacing was with good accuracy. The covariance matrix of the center positions was used to give some confidence on the degeneracy of the mode spacings measures. We could also use this to test the linearity of the piezo scan across the cavity. We found that close to the turning point of the cavity scan the piezo had a non-linear response and would artificially stretch the distance between the mode spacing potentially giving us a false reading of the degeneracy of the spacings. We found that if we operate near the middle of the scan we did not encounter this problem.

To operate the program, the user is prompted to input how many peaks are to be fitted followed by entering guesses of the parameters Y_0, a, ω and x_0 to be used by the algorithm. The program reads in the data file, fits the peaks and plots a new graph with the data and fit superimposed as well outputting all the fitting parameters requested, example plots of the program output are shown below in figures A.1, A.2, A.3.

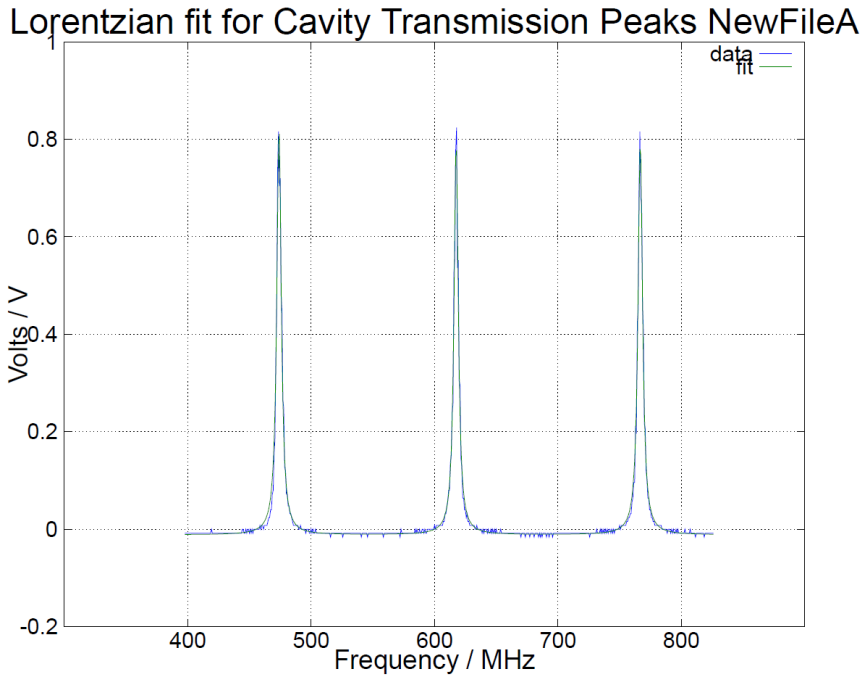

Figure A.1: Output of the Octave code after fitting Lorentzians on 3 peaks.

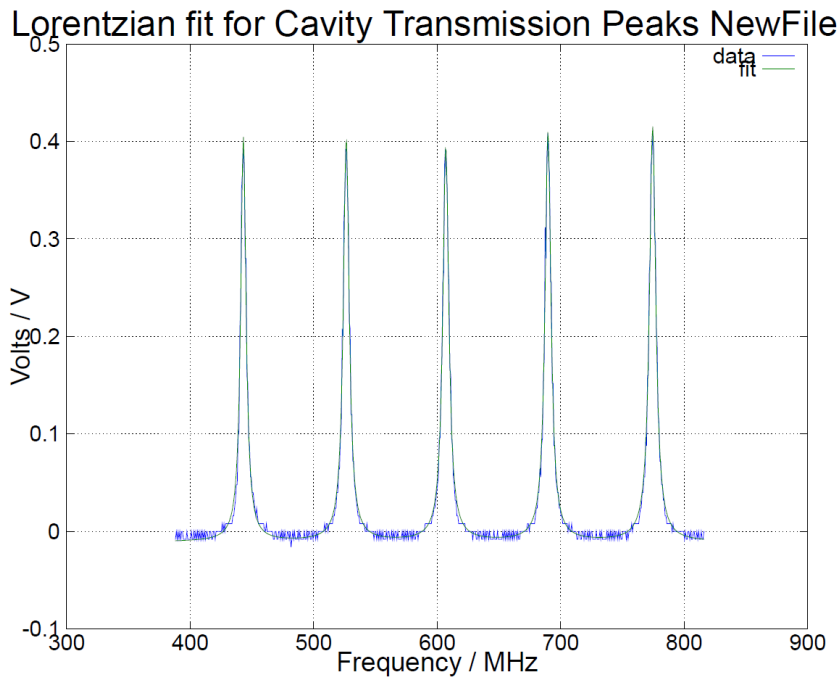

Figure A.2: Output of the Octave code after fitting Lorentzians on 5 peaks.

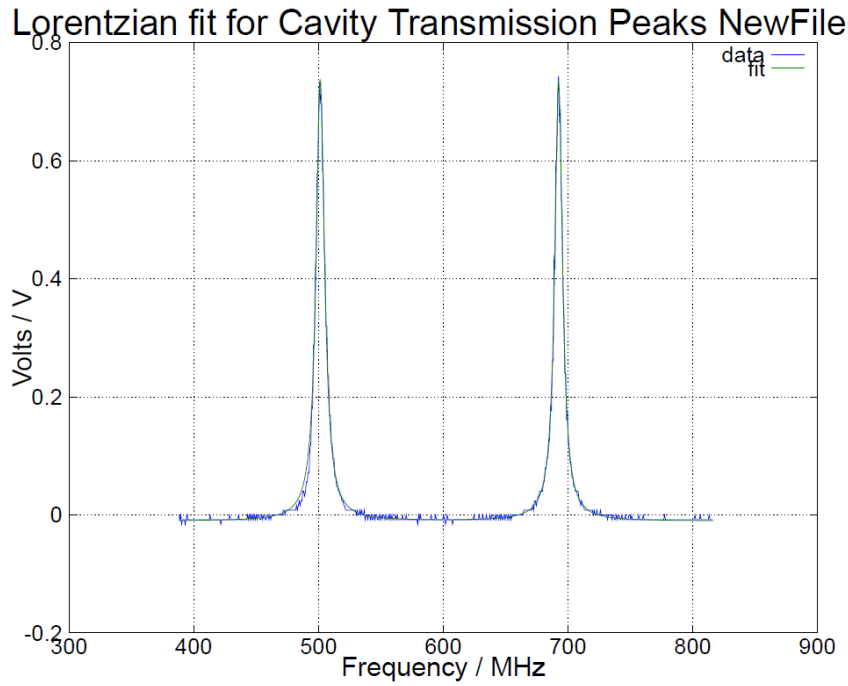

Figure A.3: Output of the Octave code after fitting Lorentzians on 2 peaks.

ACKNOWLEDGEMENTS

Firstly, I would like to acknowledge my supervisor Jon Goldwin for giving me the opportunity to study in his lab. l have learned not only a lot about cold atoms and quantum optics from him but also how to be a good scientist, which l am sure will carry me very far. Next I would like to thank Komal, the other PhD student who started with me on the experiment, being new to cold atoms was very daunting but it was nice to have someone just as daunted to share the experience with, we have come a long way from huddling in front of a computer screen in the lab after hours trying to figure out how to do a Gaussian fit in SciDAVis to were we are now.

Next I would like to thank the new additions to the lab, Rob and Andreas. Rob came at a critical time were we really needed manpower to build the vacuum system and was a very welcome addition, I wont forget the magnetic coil construction incident in a hurry. Andreas joined at the right time to take over the reigns from Komal and I leaving the lab, I hope we have left it in a fit state for you, just dont ask about the hammer, it is better if you don't know.

I would also like to thank the rest of the PhD students that make up the Cold Atom group, far too many to name now, but I take pride in us being the group that never missed a school BBQ or event always being the last to leave and taking any remaining "beverages" with us. To all those who helped me plan the YAO conference 2013, thank you very much, I still cannot believe that we actually managed to pull it off and only one participant broke their leg!

A special thanks to Kai Bongs and all the other senior staff for creating this environment for us, the culture and atmosphere in the group is to be admired. I would also like to thank the School of Physics machine shop who manufactured a lot of the components for the experiment and at such a high quality, the experiment would not have been possible without their expertise.

Lastly I would like to thank my family for all their love and support throughout the last four years, my parents for their courage to leave their country with everything and everyone they knew behind to come here and give me and my brother better opportunities in life, I hope I have done you proud. Thanks to my brother

Alex for being a good friend, brother, uncle and brother-in-law, really appreciate it man. Special thanks to my wife, Nelly, for being there for me and the sacrifices you made to support me, from now on it's my turn to support you.

LIST OF REFERENCES

[1] M. Atkinson, N. Santoro, and J. Urrutia. Integer sets with distinct sums and differences and carrier frequency assignments for nonlinear repeaters. *Communications, IEEE Transactions on*, 34:614–617, 1986.

[2] P.A. Bélanger. Beam propagation and the abcd ray matrices. *Opt. Lett.*, 16:196–198, 1991.

[3] P.R. Berman and V.S. Malinovsky. *Principles of Laser Spectroscopy and Quantum Optics*. Princeton University Press, 2011.

[4] S. Bernon. *Trapping and nondemolition measurement of cold atoms in a high-finesse ring cavity*. PhD thesis, Lecole Polytechnique, 2011.

[5] R.W. Boyd. Intuitive explanation of the phase anomaly of focused light beams. *J. Opt. Soc. Am.*, 70:877–880, 1980.

[6] D.M. Brink and G.R. Satchler. *Angular Momentum*. Oxford, 1962.

[7] H.J. Carmichael. *An Open Systems Approach to Quantum Optics*. Springer Verlag, 1993.

[8] H.J. Carmichael. *Statistical Methods in Quantum Optics*. Springer Verlag, 1999.

[9] L.G. Carpenter. *Vacuum Technology*. Hilger, 1970.

[10] S. Chu, L. Hollberg, J.E. Bjorkholm, A. Cable, and A. Ashkin. Three-dimensional viscous confinement and cooling of atoms by resonance radiation pressure. *Phys. Rev. Lett*, 1:48–51, 1985.

[11] K.L. Corwin, Z.T. Lu, C.F. Hand, R.J. Epstein, and C.E. Wieman. Frequency-stabilized diode laser with the zeeman shift in an atomic vapor. *Appl. Opt.*, 37:3295–3298, 1998.

[12] J.Y. Courtois, G. Grynberg, B. Lounis, and P. Verkerk. Recoil-induced resonances in cesium: An atomic analog to the free-electron laser. *Phys. Rev. Lett.*, 72:3017–3020, 1994.

[13] CVI. *Fundamental Optics Guide*. CVI Melles Griot, 2009.

[14] S.M. Rochester D. Budker and V.V. Yashchuk. Obtaining frequency markers of variable separation with a spherical mirror fabry-perot interferometer. *Rev. Sci. Instrum.*, 71:2984–2987, 2000.

[15] J. Dalibard and C. Cohen-Tannoudji. Laser cooling below the doppler limit by polarization gradients: simple theoretical models. *J. Opt. Soc. Am. B*, 6:2023–2045, 1989.

[16] W. Demtroder. *Laser Spectroscopy.* Berlin:Springer, 1998.

[17] R. H. Dicke. Coherence in spontaneous radiation processes. *Phys. Rev.*, 93:99–110, 1954.

[18] R.W.P. Drever, J.L. Hall, F.V. Kowalski, J. Hough, G.M. Ford, A.J. Munley, and H. Ward. Laser phase and frequency stabilization using an optical resonator. *Applied Physics B: Lasers and Optics*, 31:97–105, 1983.

[19] M. Ducloy and D. Bloch. Theory of degenerate four-wave mixing in resonant doppler-broadened media. - ii. doppler-free heterodyne spectroscopy via collinear four-wave mixing in two- and three-level systems. *J. Phys. France*, 43:57–65, 1982.

[20] Th. Elsässer, B. Nagorny, and A. Hemmerich. Collective sideband cooling in an optical ring cavity. *Phys. Rev. A*, 67:051401, May 2003.

[21] T. Floyd. *Principles of Electric Circuits (5th ed.).* Prentice Hall, 1993.

[22] L.G. Gouy. Sur une propriete nouvelle des ondes lumineuses. *Compt. Rendue Acad. Sci*, 2:1251–1253, 1890.

[23] T.W. Hansch and B. Couillaud. Laser frequency stabilization by polarization spectroscopy of a reflecting reference cavity. *Optics Communications*, 35:441–444, 1980.

[24] T.W. Hänsch, M.D. Levenson, and A.L. Schawlow. Complete hyperfine structure of a molecular iodine line. *Phys. Rev. Lett.*, 26:946–949, 1971.

[25] P. Hariharan and P.A. Robinson. The gouy phase shift as a geometrical quantum effect. *Journal of Modern Optics*, 43:219–221, 1996.

[26] M.L. Harris, C.S. Adams, S.L. Cornish, I.C. McLeod, E. Tarleton, and I.G. Hughes. Polarization spectroscopy in rubidium and cesium. *Phys. Rev. A*, 73:062509, 2006.

[27] K.C. Harvey and C.J. Myatt. External-cavity diode laser using a grazing-incidence diffraction grating. *Opt. Lett.*, 16:910–912, 1991.

[28] E. Hecht. *Optics (4th Edition).* Addison Wesley, 2001.

[29] D.J. Heinzen, J.J. Childs, J.E. Thomas, and M.S. Feld. Enhanced and inhibited visible spontaneous emission by atoms in a confocal resonator. *Phys. Rev. Lett.*, 58:1320–1323, 1987.

[30] S. Inouye, A.P. Chikkatur, D.M. Stamper-Kurn, J. Stenger, D.E. Pritchard, and W. Ketterle. Superradiant rayleigh scattering from a bose-einstein condensate. *Science*, 285:571–574, 1999.

[31] E.T. Jaynes and F.W. Cummings. Comparison of quantum and semiclassical radiation theories with application to the beam maser. *Proceedings of the IEEE*, 51:89–109, 1963.

[32] J.A Kim, U. Shim, and W. Jhe. Frequency-stabilized diode laser with the zeeman shift in an atomic vapor. *J. Kor. Phys. Soc.*, 35:222–225, 1999.

[33] D. Kleppner. Inhibited spontaneous emission. *Phys. Rev. Lett.*, 47:233–236, 1981.

[34] D. Kruse, M. Ruder, J. Benhelm, C. von Cube, C. Zimmermann, Ph.W. Courteille, Th. Elsässer, B. Nagorny, and A. Hemmerich. Cold atoms in a high-q ring cavity. *Phys. Rev. A*, 67:051802, 2003.

[35] D. Kruse, C. von Cube, C. Zimmermann, and Ph.W. Courteille. Observation of lasing mediated by collective atomic recoil. *Phys. Rev. Lett.*, 91:183601, 2003.

[36] D.J. McCarron, S.A. King, and S.L. Cornish. Modulation transfer spectroscopy in atomic rubidium. *Measurement Science and Technology*, 19:105601, 2008.

[37] J.H. Moor. *Building Scientific Apparatus*. Cambridge University Press, 2009.

[38] L. Mudarikwa, K. Pahwa, and J. Goldwin. Sub-doppler modulation spectroscopy of potassium for laser stabilization. *Journal of Physics B: Atomic, Molecular and Optical Physics*, 45:065002, 2012.

[39] B. Nagorny, Th. Elsasser, H. Richter, A. Hemmerich, D. Kruse, C. Zimmermann, and Ph. Courteille. Optical lattice in a high-finesse ring resonator. *Phys. Rev. A*, 67:031401, 2003.

[40] W. Nagourney. *Quantum Electronics for Atomic Physics*. OUP Oxford, 2010.

[41] N. Nemitz. Setup of a stable high-resolution laser system. Master's thesis, University of Stuttgart, 2004.

[42] K. Pahwa, L. Mudarikwa, and J. Goldwin. Polarization spectroscopy and magnetically-induced dichroism of the potassium d2 lines. *Opt. Express*, 20:17456–17466, 2012.

[43] P. G. Pappas, M. M. Burns, D. D. Hinshelwood, M. S. Feld, and D. E. Murnick. Saturation spectroscopy with laser optical pumping in atomic barium. *Phys. Rev. A*, 21:1955–1968, 1980.

[44] T. Petelski, M. Fattori, G. Lamporesi, J. Stuhler, and G.M. Tino. Doppler-free spectroscopy using magnetically induced dichroism of atomic vapor: a new scheme for laser frequency locking. *Eur. Phys. J. D*, 22:279–283, 2003.

[45] W.D. Phillips, P.L. Gould, and P.D. Lett. Cooling, stopping, and trapping atoms. *Science*, 4842:877–883, 1988.

[46] R.V. Pound. Electronic frequency stabilization of microwave oscillators. *Rev. Sci. Instrum*, 17:490, 1946.

[47] E.M. Purcell. Spontaneous emission probabilities at radio frequencies. *Phys. Rev. Lett.*, 69:69–681, 1946.

[48] E.L. Raab, M. Prentiss, A. Cable, S. Chu, and D.E. Pritchard. Trapping of neutral sodium atoms with radiation pressure. *Phys. Rev. Lett.*, 59:2631–2634, 1987.

[49] J.M. Raimond, M. Brune, and S. Haroche. Manipulating quantum entanglement with atoms and photons in a cavity. *Rev. Mod. Phys.*, 73:565–582, 2001.

[50] G. Ritt, G. Cennini, C. Geckeler, and M. Weitz. Laser frequency offset locking using a side of filter technique. *Applied Physics B*, 79:363–365, 2004.

[51] B.E.A. Saleh and M.C. Teich. *Fundamentals of Photonics*. John Wiley Sons, 1991.

[52] G.W. Series, T.W. Hansch, and A.L. Schawlow. The spectrum of atomic hydrogen. *Scientific American*, 240:94–111, 1979.

[53] Z. Shanchao, J.F. Chen, C. Liu, S. Zhou, M.M.T. Loy, G.K.L. Wong, and S. Du. A dark-line two-dimensional magneto-optical trap of 85rb atoms with high optical depth. *Review of Scientific Instruments*, 83:073102, 2012.

[54] J.H. Shirley. Modulation transfer processes in optical heterodyne saturation spectroscopy. *Opt. Lett.*, 7:537–539, 1982.

[55] A.E. Siegman. *Lasers*. University Science Books, 1990.

[56] S. Slama, S. Bux, G. Krenz, C. Zimmermann, and Ph.W. Courteille. Superradiant rayleigh scattering and collective atomic recoil lasing in a ring cavity. *Phys. Rev. Lett.*, 98:053603, 2007.

[57] J.J. Snyder, R.K. Raj, D. Bloch, and M. Ducloy. High-sensitivity nonlinear spectroscopy using a frequency-offset pump. *Opt. Lett.*, 5:163–165, 1980.

[58] V. Stert and R. Fischer. Doppler-free polarization spectroscopy using linear polarized light. *Applied physics*, 17:151–154, 1978.

[59] D. Subbarao. Topological phase in gaussian beam optics. *Opt. Lett.*, 20:2162–2164, 1995.

[60] M. Tavis and F.W. Cummings. Exact solution for an n-molecule-radiation-field hamiltonian. *Phys. Rev.*, 170:379–384, 1968.

[61] M. Tavis and F.W. Cummings. Approximate solutions for an n-molecule-radiation-field hamiltonian. *Phys. Rev.*, 188:692–695, 1969.

[62] G. Wasik, W. Gawlik, J. Zachorowski, and W. Zawadzki. Laser frequency stabilization by doppler-free magnetic dichroism. *Applied Physics B*, 75:613–619, 2002.

[63] C. Wieman and T.W. Hänsch. Doppler-free laser polarization spectroscopy. *Phys. Rev. Lett.*, 36:1170–1173, 1976.

[64] J. Zhang, D. Wei, C. Xie, and K. Peng. Characteristics of absorption and dispersion for rubidium d2 lines with the modulation transfer spectrum. *Opt. Express*, 11:1338–1344, 2003.